

Time-resolved investigations on ultrafast shape modification dynamics of silver nanoparticles embedded in glass

Dissertation

zur Erlangung des akademischen Grades
doktor rerum naturalium (Dr. rer. nat.)

vorgelegt der

Naturwissenschaftlichen Fakultät II
der Martin-Luther-Universität Halle-Wittenberg

von

Ahmet Akın Ünal
geb. am 7. October 1979 in Çorum, Türkei

Gutachter:

1. Prof. Dr. Heinrich Graener (Martin-Luther-Universität Halle-Wittenberg)
2. Prof. Dr. Jamal Berakdar (Martin-Luther-Universität Halle-Wittenberg)
3. Prof. Dr. Fabrice Vallée (Université Claude Bernard Lyon 1, Frankreich)

verteidigt am 19.06.2009

Contents

1. INTRODUCTION	1
1.1. Motivation and general aims.....	4
2. SURFACE PLASMONS ON METAL NANOPARTICLES	5
2.1. Optics of metals.....	6
2.1.1. Interaction of metals with electromagnetic fields	6
2.2. Optical properties of metal nanoparticles in dielectrics	9
2.2.1. Mie theory and the quasistatic approximation.....	10
2.2.2. Far-field extinction cross section and spectral properties	11
2.2.2.1. Dependence on dielectric functions.....	13
2.2.2.2. Dependence on particle sizes.....	14
2.2.2.3. Dependence on particle shapes	15
2.2.2.4. Dependence on particle concentration.....	16
2.2.3. Optical near fields	17
3. LASER PULSE INTERACTION WITH METAL NANOPARTICLES	19
3.1. Weak and strong excitation regimes	19
3.2. Ultrafast heating and cooling dynamics of nanoparticles.....	23
3.2.1. Electronic thermalization and electron-phonon coupling.....	24
3.2.2. Two temperature model for the strong excitation regime	27
3.2.3. Nanoparticle ionization	33
3.2.4. Nanoparticle dissolution via Coulomb explosion.....	36
4. SAMPLES AND THE EXPERIMENTAL APPARATUS	39
4.1. Composite glass containing silver nanoparticles.....	39
4.2. Laser-induced dichroism in composite glass	41
4.3. Femtosecond laser pulses and pulse characteristics.....	44
4.4. Time and polarization-resolved pulse pair irradiation.....	49
4.5. Temperature dependent irradiation.....	51
5. RESULTS AND DISCUSSION	53
5.1. Influence of time delay on nanoparticle shapes – an introduction	54
5.2. Temporal evolution of surface plasmon bands.....	59
5.2.1. Parallel-polarized pulse pairs	59
5.2.2. Orthogonal-polarized pulse pairs	63
5.3. First 20 ps of nanoparticle shape modifications	65
5.4. Nanoparticle ionization through electron emissions	69
5.4.1. Electronic band structure of composite glass containing silver nanoparticles	69
5.4.2. Modeling of nanoparticle ionization with the extended TTM.....	71

5.4.3. Pulse-enhanced and isotropic thermal electron emissions for pulse pair irradiations	73
5.5. Repulsive Coulomb forces on the ionized nanoparticle.....	77
5.6. Mobility of emitted silver ions	78
5.6.1. Effect of glass temperature on nanoparticle shape modifications	81
5.6.2. Nanoparticle dissolution	82
5.7. Reduction of silver ions and recombination	83
5.8. One pulse model.....	85
6. SUMMARY AND CONCLUSIONS	89
REFERENCES	93
Acknowledgments	99
Publications	101
Curriculum Vitae	103
Erklärung	105

Chapter

1. Introduction

The interaction of light with matter has started as early as the dawn of the Universe and enabled the energy flow between light quanta (photons) and the building blocks of matter (electrons and atoms). This interaction exists in all physical systems; from the ionization of smallest atomic units to the shining of gigantic stars in the form of emission and absorption of photons. Various material properties, mainly the optical properties, depend on the mentioned energy absorption and emission processes. In this context, the interaction of light with matter on a size scale between the macro world and the atomic world has a particular importance both for fundamental reasons and for technological applications. This size scale, which is known as the nanoscale, consists of “small” particles having sizes between large molecules and small pieces of bulk materials (range of 2-100 nm). Owing to their mesoscopic sizes, they possess very peculiar and interesting linear and nonlinear optical properties.

Such nanoparticles (e.g. metallic nanoparticles) surrounded by dielectric host media have been known since ancient times. The media having a distribution of embedded nanoparticles are called as nanocomposite materials. One of the oldest examples for these materials is the Lycurgus cup [1, 2], a Roman vase from the fourth century A.D., which is on display in the British Museum. The glass material of this cup changes its color depending on the light illumination. It appears green when it is viewed in reflected light, for example, in daylight. However when a light is placed into the cup and transmitted through the glass, it appears red (Fig. 1.1(a-b)). Now it is well-known that this coloration of the cup is determined by specific light absorption bands of the embedded metallic nanoparticles (silver-gold alloys), owing to their frequency-selective electron oscillations (i.e. surface plasmon bands). Other world-famous of such “plasmonic” materials that contain metallic nanoparticles are the colorful glass windows of medieval French and German gothic cathedrals (Fig. 1.1(c)). Especially the wine color of the windows is originated from gold nanoparticles, the electrons of which oscillate in green light – absorbing the energy of the green. Therefore the gold nanoparticles in glass produce the wine color (complementary color of green), which is obviously very different from the color of bulk gold.

The different colors of the materials mentioned above are due to the plasmon absorption bands of the nanoparticles. These properties are indeed small particle effects that do not exist in the individual metal atoms as well as in the bulk [3, 4, 5]. Although a smooth silver surface reflects all the visible light, silver nanoparticles in a liquid or glass exhibit a strong absorption. The reason for this is that a small silver particle has a surface plasmon resonance around 410 nm, while strong optical absorption in bulk silver occurs only for $\lambda < 310$ nm, corresponding to interband transitions from the *d*-bands. As a result of such size effects, various nanocomposite materials are currently of special interest in developing optical and microelectronic devices. This field of science is now popularly called as nanophotonics and plasmonics [6, 7].



Fig. 1.1. Top panel: the Lycurgus Cup containing metallic nanoparticles viewed in reflected (a) and transmitted light (b). The photos are adapted from [1]. Bottom panel: glass windows of a Gothic cathedral displaying different colors owing to the embedded metallic nanoparticles.

Early understanding of the physics of surface plasmons in metallic nanostructures dates back to the beginning of the twentieth century by Wood (1902) [8], Maxwell Garnett (1904) [9] and Mie (1908) [10]. In very general terms, the electron density waves in bulk metals are called plasmons, which are longitudinal electron waves and do not interact with transverse waves, such as light. However, the electron and light waves can couple with each other at metal surfaces and this state is named as a surface plasmon. Therefore, surface plasmons are defined as collective oscillation of conduction band electrons that occur at a metal-dielectric interface, and they are responsible for specific absorption spectra, which give the composite materials their colors in turn. Depending on the geometry of the interface (thin film, nanosphere, nanoshell, nanorod, channel, hole array, etc.) and type of the nanostructure, surface plasmons can take various forms. For example, in the case of flat interfaces, plasmons are freely propagating electron density waves throughout the surface; however, metallic nanospheres possess “localized” electron oscillations along the nanospheres and the surrounding dielectric interface [4]. The physical background of light interaction with metals and specifically with metallic nanoparticles in dielectric media will be presented in Chapter 2. Additionally, the

significant linear and nonlinear optical properties of these nanoparticles will be described according to their dielectric functions, sizes, and shapes.

A metallic nanoparticle can be regarded as a resonator for surface plasmons, which is thus called as the surface plasmon resonance. In the case of resonant excitation, the oscillation amplitudes of the plasmon waves can overcome the excitation amplitude by orders of magnitude, which mean a strong enhancement of the local electromagnetic field compared to the exciting field [11]. Metal nanoparticles can therefore confine and enhance electromagnetic fields in nano-dimensions. As a result of this, in the last decades there has been an increasing activity in the research and development of surface plasmon-based structures and devices employing the resonance behavior in far and near-fields, such as optical filters [12], media for optical data storage [13], nonlinear media [14, 15], waveguide applications [16, 17], and biological labels [18]. Surface-enhanced effects, like surface-enhanced Raman scattering or surface enhanced fluorescence [5, 19] take advantage of both the near field and the far field of resonantly excited metal nanoparticles [20].

Investigations on the nanoscale interaction of light with the embedded metallic nanoparticles, which require high resolution in spatial and temporal domains, have become possible with the invention of ultrashort-pulsed lasers and with the advance of nanoprobe such as electron microscopy. Indeed the physical mechanisms lying under the dynamics of the surface plasmon oscillations require ultrafast detection of the rapid optical changes during and after the laser pulse excitation. Upon photon absorption, the energy distribution along the nanoparticle (via electron-electron and electron-phonon interactions) happens rather rapidly – within a few picoseconds [21], which is only possible to investigate with pulses shorter than a picosecond in time, before the events are finished. In this context, the present thesis focuses on the ultrafast dynamics of femtosecond light interaction with the silver nanoparticles that are embedded in glass matrices.

In Chapter 3 an overview of the laser pulse interaction with metal nanoparticles in weak and strong excitation regimes will be given. The ultrafast heating and cooling dynamics of nanoparticles comprising the electronic thermalization and electron-phonon couplings will be developed. Chapter 4 introduces the experimental apparatus together with the preparation and characterization of silver nanoparticles embedded in soda-lime glass. High intensity (strong) femtosecond laser irradiation of composite glasses that contain silver nanoparticles has been found to cause optical dichroism because of permanent nanoparticle shape modifications [22 , 23]. Linearly-polarized laser irradiation transforms the initially spherical silver nanoparticles into elongated shapes with their symmetry axes oriented along the direction of the laser (light) polarization [24]. The shape modification causes the original single plasmon band of spherical nanoparticles to be irreversibly split into two bands of electron oscillations, one parallel (p-polarized) and one perpendicular (s-polarized) to the long axis of the modified nanoparticle. The separation between s- and p-polarized resonances depends strongly on the aspect ratio, which is defined as the length of the modified nanoparticle divided by its width. The details of these aspects and the experimental methods used for the time-resolved investigations of the pulse interaction with silver nanoparticles will also be presented in Chapter 4.

1.1. Motivation and general aims

Although the time-resolved investigations until now have extensively focused on the weak excitation regime (having transient and reversible surface plasmon changes) [25, 26], the physical situation of strong excitation is of high interest both for fundamental reasons (e.g. tailoring linear and nonlinear optical properties) and for device applications. In this context, the spectral positions of surface plasmon resonances before and after laser irradiation are well-known with respect to the irradiation parameters; however, the dynamical information regarding the laser-induced nanoparticle shape modification mechanisms (i.e. permanent changes in surface plasmon bands) remains as an interesting research topic [27, 28, 29]. The underlying question is how an ultrashort laser pulse can create a directional memory for the material transport so that the nanoparticle anisotropy happens along the pulse polarization direction.

Studies so far have shown that upon irradiation by intense and resonant femtosecond laser pulses, conduction electrons of the nanoparticle along the laser polarization direction can be emitted into the glass matrix as a result of the enhanced local fields, thereby ionizing the nanoparticle. The emitted electrons relax rapidly and they are trapped in color centers of the glass [30]. The remaining electrons equilibrate to a hot electronic distribution and they heat up the nanoparticle lattice gradually. The ionized, hot nanoparticle becomes unstable due to the intense electro- and thermo-dynamical forces on itself. Binding energy of the ions is overcome gradually and silver ions are emitted into the surrounding glass matrix [28, 30], dissolving the nanoparticle partially. Subsequently (in the long term), the reduction and aggregation of these ions form small silver clusters mostly along the pole sides of the nanoparticle along the laser polarization direction. The recombination of these silver clusters to the main nanoparticle leads to a slow by slow elongation of the nanoparticle within tens or hundreds of pulses (depending on the pulse intensity). The aim of this thesis is to investigate the mentioned laser-induced shape modification dynamics of glass-embedded silver nanoparticles.

Chapter

2. Surface plasmons on metal nanoparticles

First scientific studies related to surface plasmons date back to the beginning of the twentieth century. Following Sommerfeld's mathematical description of radio waves propagating along the surface of a conductor [1], Wood observed strange intensity drops in reflection measurements on metallic gratings [2]. A few years later, Maxwell Garnett [3] described the colors of metal containing glasses using the Drude theory of metals [4] and the electromagnetic properties of small spheres as derived by Rayleigh. In an effort to develop further understanding, in 1908 Gustav Mie [5] developed a clear mathematical foundation of light absorption and scattering by spherical particles.

Some fifty years later, Pines [6] theoretically described the collective oscillations of free electrons in metals, and he called these oscillations as "plasmons." Just like photons are quantum of light waves and phonons are quantum of sound waves, plasmon name was denoted as the quantum of electron waves/oscillations. In the same year Fano [7] introduced the term "polariton" for the coupled oscillation of electrons and photons in dielectric media. As a result, the coupling of surface plasmons with light has been unified in the name of surface plasmon polaritons, but the polariton term is often dropped in the literature. A major step forward in the field was the excitation of Sommerfeld's surface waves with visible light by Kretschmann *et al.* [8]. They have employed a prism for coupling of light to plasmons (known as Kretschmann configuration), which enabled the surface plasmon research on thin metallic films much easier. It was in 1970, when Kreibig *et al.* [9] described the optical properties of metal nanoparticles in terms of localized surface plasmons for the first time. Another big step forward in the field was taken by Fleischmann *et al.* [10], who observed enhanced Raman scattering from pyridine molecules in the vicinity of silver surfaces owing to the surface plasmons. This has opened up the possibility of a number of applications employing enhanced local fields.

Having such a long history behind, the research in this area has gained acceleration especially in the last decades with the development of manufacturing and measuring techniques. The rising of nanotechnology together with the advances in photonics have created their fusion as "nanophotonics." Clearly stated, nanophotonics deals with the interaction of light with matter on a nanometer size

scale. Under the general name of nanophotonics, the research specifically on metallic nanoparticles (their unique linear and nonlinear optical responses) constitute the area of “plasmonics” [11, 12]. It explores the interaction of light with conduction electrons (i.e. localized surface plasmons) in metallic nanoparticles and the outcoming enhanced optical near fields that can provide the possibility of localization and guiding of light in sub-wavelength dimensions.

2.1. Optics of metals

When isolated atoms of a metallic element come together to form a metal, the core electrons remain tightly bound to the atomic nuclei while the weakly bound valence electrons can wander far away from their parent atoms. In the metallic context they are called as essentially free (conduction) electrons [13]. For this reason, metals are generally defined by their free electrons in the ground state, which are not bound to single atoms but to the metal bulk, moving in a periodic potential of fixed positively charged atoms. These free electrons are responsible for the well-known metallic features such as high electrical and heat conductivity, and high optical reflectivity. Here, we will focus only on the optical properties of metals.

2.1.1. Interaction of metals with electromagnetic fields

The free electrons of metals can be treated as a plasma (a gas of free charge carriers) and they sustain propagating plasma waves upon excitation. As it was mentioned before, plasma waves are longitudinal electromagnetic waves and their quanta are referred to as plasmons. These plasmons are responsible for the optical properties of metals. Light of frequency below the plasma frequency is reflected, as the metal electrons screen the electric field of the light and they do not allow electromagnetic waves to propagate through them. However, the field penetration increases significantly for the light of frequency above the plasma frequency. Most metals have plasma frequency in the ultraviolet region of the spectrum, making them shiny in the visible range. On the other hand, noble metals like silver and gold have electronic interband transitions in the visible range, absorbing specific light energies, thereby yielding their distinct colors. These dispersive properties can be described via a complex dielectric function $\varepsilon(\omega)$ using the Drude theory of metals [4, 13], which is also known as Drude-Sommerfeld model.

The equation of motion for an electron subjected to an oscillating external electric field $\mathbf{E}(t) = E_0 e^{-i\omega t}$ can be written as:

$$m \frac{d^2}{dt^2} x + m\gamma \frac{d}{dt} x = -eE \quad (2.1)$$

where m is the effective electron mass and e is the charge of an electron. γ is the damping constant, and it is related to the lifetime associated with the electron scattering from various processes. In the bulk metal, γ has main contributions from electron–electron and electron–phonon scatterings.

The electrons affected by the electric field follow an oscillatory displacement in the form of $\mathbf{x}(t) = \mathbf{x}_0 e^{-i\omega t}$, where ω is the angular frequency of the light. The complex amplitude of this expression incorporates any phase shifts between the driving field and the response via [11]:

$$x(t) = \frac{e}{m(\omega^2 + i\gamma\omega)} E(t) \quad (2.2)$$

Having Eq. (2.2), the polarizability α for a single electron ($\alpha = e\mathbf{x}/E$, which is the dipole moment per unit field) and the macroscopic polarization $\mathbf{P} = -n\mathbf{e}\mathbf{x}$ can be found. The field of the incoming light can induce polarization of the conduction electrons, where the electrons are displaced with respect to the much heavier positively charged atoms. This polarization is given in the following as:

$$P = -\frac{ne^2}{m(\omega^2 + i\gamma\omega^2)} E \quad (2.3)$$

Now, using the well-known relation between the electric displacement and the polarization ($\mathbf{D} = \varepsilon_0\mathbf{E} + \mathbf{P}$) it is possible to write the electric displacement

$$D = \varepsilon_0 \left(1 - \frac{\omega_p^2}{\omega^2 + i\gamma\omega}\right) E \quad (2.4)$$

where ε_0 is the permittivity of free space and ω_p is defined as the plasma frequency of the free electron gas [14], which is composed of

$$\omega_p^2 = \frac{ne^2}{m\varepsilon_0} \quad (2.5)$$

with n being the density of conduction electrons. From this definition of plasma frequency, the plasma energy can be estimated simply by

$$E_p = \hbar \sqrt{\frac{ne^2}{m\varepsilon_0}} \quad (2.6)$$

Recalling that $\mathbf{D} = \varepsilon\varepsilon_0\mathbf{E}$, we can write the dielectric function of the free electron gas from Eq. (2.4) as:

$$\varepsilon(\omega) = 1 - \frac{\omega_p^2}{\omega^2 + i\gamma\omega} \quad (2.7)$$

This is the dielectric response of a metal to an electromagnetic field. It can be written as a combination of its real and imaginary parts in the form:

$$\varepsilon(\omega) = \varepsilon_1(\omega) + i\varepsilon_2(\omega) \quad (2.8)$$

The real part, ε_1 , determines the degree, to which the metal polarizes in response to an applied electric field. The imaginary part, ε_2 , quantifies the relative phase shift of this induced polarization with respect to the external field, and it includes losses.

For noble metals the described Drude model must be corrected for the influence of d -band electrons, which requires an extension to the model. In the case of noble metals there are two types of contributions to the dielectric constant of the metal: One is from the free conduction electrons (intraband transitions) by the Drude model, and the other is from the inner d -band electrons, which describes interband transitions (from inner d orbitals to the conduction band) [14]. For example, the dielectric function of silver can be written in the form:

$$\varepsilon(\omega) = \varepsilon_{intra}(\omega) + \varepsilon_{inter}(\omega) \quad (2.9)$$

where $\varepsilon_{intra}(\omega)$ is the Drude part originating from the free electron contributions that is written in Eq. (2.7) and $\varepsilon_{inter}(\omega)$ is the interband part originating from the band to band transitions. Taking this into account, the dielectric function can be written as

$$\varepsilon(\omega) = \varepsilon_b + 1 - \frac{\omega_p^2}{\omega^2 + i\gamma\omega} \quad (2.10)$$

where ε_b is the electric permittivity associated with interband transitions of the core (bound) electrons. Because of this complexity, the experimentally measured values for $\varepsilon(\omega)$ [15] are often used rather than the calculated ones. The real part of the dielectric function of silver is negative in the visible and infrared region, while the imaginary part has a very small positive value as seen in Fig. 2.1.

The complex dielectric function given in Eq. (2.7), and more generally in Eq. (2.10), determines the optical properties (such as reflectance, transmittance and absorbance) of metals upon light interaction. Also note that these optical properties depend not only on the type of the metal but also on the surrounding dielectric medium. Therefore, the optical properties of metals are dominated by the relation between the dielectric functions of the metal and its surrounding medium. As a result of this, we will now concentrate mainly on the optical properties of metals (and specifically metallic nanoparticles) in dielectric media.

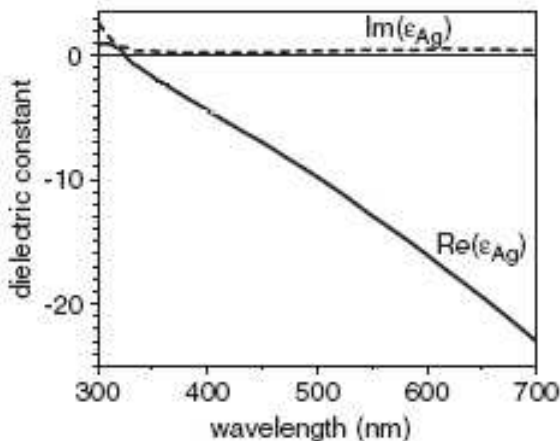


Fig. 2.1. The dielectric function of silver: solid line is the real part and dashed line is the imaginary part. The figure is adapted from [16].

2.2. Optical properties of metal nanoparticles in dielectrics

As already mentioned in the previous sections, light can not be coupled directly to the surface plasmon mode at a flat metal surface because the wavevector k_{sp} of a surface plasmon wave is significantly larger than that of light propagating in air. As a result of this, various geometries are used to match the wavevectors of surface plasmons and light, one of which is the Kretschmann geometry employing a prism [8]. There are also other geometries such as grating structures on metal films that provide coupling between plasmons and light [17].

It should be noted that the “surface plasmon” term is mostly used to describe the excitations at the metal-dielectric interface in the case of flat surfaces, where the plasmons can only be excited by using special geometries described above. However, in the case of metal nanoparticles, plasmon oscillations are localized (they do not propagate); and therefore, they are not characterized by a wavevector k_{sp} . In the literature they are sometimes called as localized surface plasmons or nanoparticle plasmons. Throughout this thesis the nanoparticle plasmon resonances will be called as surface plasmons on metal nanoparticles. These localized plasmons can easily be excited by light absorption in the nanoparticles with the specific absorption bands. For this reason, there is no need for a special geometry to excite the surface plasmons on nanoparticles. The only requirement is the wavelength of excitation (and its polarization in the case of non-spherical nanoparticles). The wavelength of light excitation should be in resonance with the plasmon oscillations as they have specific light absorption bands, which are usually called as plasmon absorption bands.

The light absorption by metallic nanoparticles significantly smaller than the wavelength of light (particle diameter $d \ll$ light wavelength λ) is within a narrow wavelength range. The wavelength of the absorption band maximum is influenced by various parameters such as the type, size and shape of the nanoparticles, as well as on the dielectric environment surrounding them. These dependences will be explained briefly in the following sections of this chapter.

We now focus on to the plasmonic excitations in metal nanoparticles. Owing to the very small dimensions of metallic nanoparticles, the light can easily penetrate into the volume of the nanoparticle and grasp at all conduction band electrons, shifting them with respect to the ionic lattice (see Fig. 2.2). The resulting oscillating

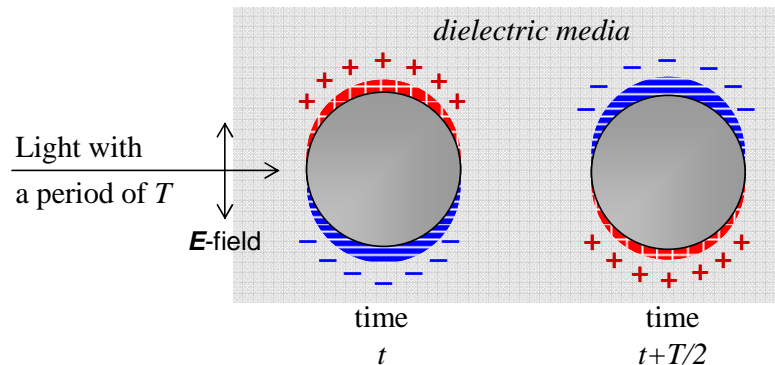


Fig. 2.2. Schematic representation of the dipolar surface plasmon excitation on a metal nanoparticle.

electric dipole on the nanoparticle produces a restoring force. Therefore the nanoparticle can be considered as a harmonic oscillator, which is driven by the light wave and damped by some losses that define the maximum amplitude and bandwidth of the resonance [16]. To arrive at the required conditions for surface plasmon resonances in nanoparticles, we will explore the physics of the localized surface plasmons in the following section.

2.2.1. Mie theory and the quasistatic approximation

Gustav Mie solved Maxwell's equations for spherical particles interacting with plane electromagnetic waves [5]. He developed a complete theory of the scattering and absorption of electromagnetic radiation by spherical particles, which is now widely known as the Mie theory. According to the theory, eigenmodes of spherical particles are either dipolar or multipolar in character depending on their sizes [9, 18]. The theory also assumes that the exciting field is homogeneous and not retarded over the particle's volume. For particles having sizes smaller than the wavelength of the exciting electromagnetic fields, it is sufficient to consider only the first term of the multipolar expansion, which is the dipolar term. This regime is called as the quasistatic (or dipole) approximation and also known as the Rayleigh limit. Our aim here is to develop this approximate solution rather than the full Mie expansion. The reason why we are interested in this regime is that the Mie theory allows a straight-forward calculation of the nanoparticle extinction spectra (the collective measure of absorption and scattering spectra); as long as the dielectric functions of the particle and the surrounding media are known and the particle size is smaller than the wavelength of the excitation light. This approximation of the scattering problem describes the optical properties of nanoparticles of dimensions below 100 nm adequately for many purposes.

In this regime, where $d \ll \lambda$, the phase of the harmonically oscillating electromagnetic field is practically constant over the particle volume. So that it is possible to calculate the spatial field distribution by assuming the simplified problem of a particle in an electrostatic field. The applied field induces a dipole moment inside the sphere [11] in the form of:

$$p = 4\pi\epsilon_0\epsilon_m r^3 \frac{\epsilon - \epsilon_m}{\epsilon + 2\epsilon_m} E_0 \quad (2.11)$$

where ϵ is the frequency dependent dielectric function of the metal (see Eq. (2.8)), and ϵ_m is the dielectric function of the surrounding matrix. The nanoparticle radius is given by r .

Having the dipole moment, the polarizability of the sphere can be defined as:

$$\alpha = 4\pi r^3 \frac{\epsilon - \epsilon_m}{\epsilon + 2\epsilon_m} \quad (2.12)$$

It is apparent that the denominator of the polarizability experiences a minimum in the case when $\varepsilon(\omega) + 2\varepsilon_m = 0$, which yields a resonant enhancement for the polarizability (for small $\varepsilon_2(\omega)$ of Eq. (2.8)). So the resonance condition can be written as [19]

$$\text{Re}[\varepsilon(\omega)] = -2\varepsilon_m \quad (2.13)$$

This requires the real part of the dielectric function (and the real part of the refractive index) of metals to be negative. This is indeed the case for noble metals in the visible spectral region (see Fig. 2.1 for the case of silver).

Relaxing the assumption of a spherical nanoparticle shape, the polarizability of an ellipsoidal metal nanoparticle parallel to the principal ellipsoid axis ($i=1, 2, 3$) follows from this theory can be written as [18]:

$$\alpha_i = \frac{4\pi}{3} abc \frac{\varepsilon - \varepsilon_m}{\varepsilon_m + L_i(\varepsilon - \varepsilon_m)} \quad (2.14)$$

where L_i is the geometrical shape factor and depends on the axis ratio of the ellipsoidal particle and the polarization of the exciting field with respect to the ellipsoid axis i . It takes values between 0 and 1. a , b and c represent the half axes of the ellipsoid. For spherical particles, axes of the ellipsoid are equal to each other $a=b=c$, and $L_i = 1/3$ in all directions, which reduces Eq. (2.14) to the expression for the polarizability of a sphere given in Eq. (2.12).

2.2.2. Far-field extinction cross section and spectral properties

The resonance condition for the polarizability (given in Eq. (2.13)) urges an optically much more interesting aspect, which is the enhancement in the efficiency of scattering and absorption of light from the metal nanoparticle. Therefore, it is very important to mention the corresponding scattering and absorption cross sections: σ_{sca} and σ_{abs} . From the results of quasistatic theory, relatively simple equations for the absorption and scattering cross-sections of a particle can be found using

$$\sigma_{abs} = k \text{Im}(\alpha) \text{ and } \sigma_{sca} = \frac{k^4}{6\pi} |\alpha|^2, \text{ respectively.}$$

The complex polarizability of the particle α (Eq. (2.12)) is proportional to the particle volume within the quasistatic approximation. $|\alpha|$ denotes the modulus and $\text{Im}(\alpha)$ the imaginary part of the polarizability. They are given in the quasistatic approximation by the following expressions for a sphere of volume V :

$$\sigma_{abs} = 4\pi k r^3 \text{Im} \left[\frac{\varepsilon - \varepsilon_m}{\varepsilon + 2\varepsilon_m} \right] \quad (2.15)$$

$$\sigma_{sca} = \frac{8\pi}{3} k^4 r^6 \left| \frac{\varepsilon - \varepsilon_m}{\varepsilon + 2\varepsilon_m} \right|^2 \quad (2.16)$$

From these cross sections, the explicit expression for the extinction cross section is found simply by $\sigma_{ext} = \sigma_{abs} + \sigma_{sca}$, which is given in the following:

$$\sigma_{ext} = \frac{18\pi V \epsilon_m^{3/2}}{\lambda} \frac{\epsilon_2}{(\epsilon_1 + 2\epsilon_m)^2 + \epsilon_2^2} \quad (2.17)$$

Note that for small particles the efficiency of absorption, scaling with r^3 , dominates over the scattering efficiency, which scales with r^6 . Therefore, for particles (less than 20 nm in diameter) it is very hard to see any scattered light because most of the light is absorbed. However, if the diameter becomes too large, the scattered spectrum eventually becomes very broad. Figure 2.3 depicts the absorption, scattering and extinction cross-sections of a silver nanosphere of 60 nm diameter, which is immersed in water. As the size of the particle is big enough, the scattering cross section is seen to be comparable with the absorption cross section.

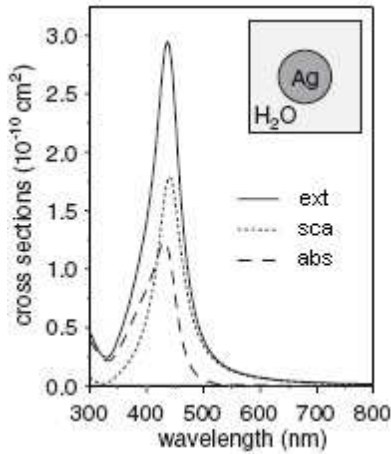


Fig. 2.3. Extinction, scattering, and absorption cross sections of a silver sphere of 60 nm diameter immersed in water. The figure is adapted from [16].

Examining again the resonance condition for the extinction cross section of Eq. (2.17), it is clearly seen that in the case of small $\epsilon_2(\omega)$, the resonance condition is produced with $\epsilon_1(\omega) = -2\epsilon_m$, leading to a vanishing denominator. Hence, the surface plasmon resonance for extinction (and also for absorption) is produced at optical frequency ω at which the resonance condition is fulfilled. This condition is sketched for silver in Fig. 2.4. For a dielectric environment having $\epsilon_m = 2.25$ (with refractive index $n = 1.5$) surrounding the silver nanoparticle, the resonance condition is observed to occur at around 400 nm. For nanoparticles of the noble metals (silver, gold and copper), the surface plasmon resonances fall into the visible region of the electromagnetic spectrum. A consequence of this is their bright colors exhibited both in transmitted and reflected light. The plasmon resonances of these metal nanoparticles can be observed using far-field extinction spectroscopy under illumination with visible light.

As it is seen from the brief summary given above, the quasistatic approximation is a simple but a very valuable regime within the Mie theory. This dipolar regime successfully describes the major parameters influencing the surface plasmon resonances on metal nanoparticles. These parameters are the dielectric functions of metals and the surrounding environment, together with the sizes and shapes of nanoparticles. Some of the details of these parameters and their roles on the

spectral positions and properties of surface plasmon resonances will be explained in the following sections.

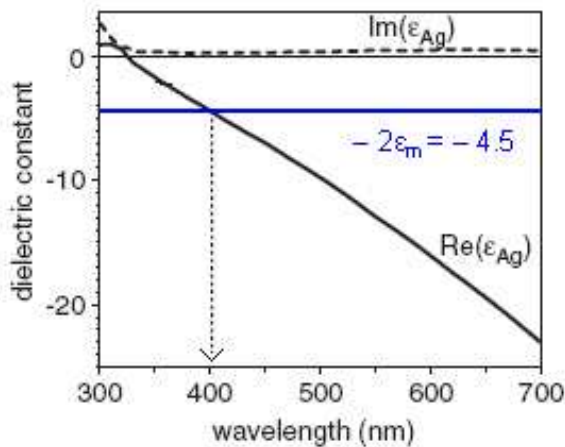


Fig. 2.4. The dielectric function of silver and two times the negative of the dielectric constant of a dielectric ($n=1.5$, $\epsilon_m=2.25$) fulfilling the surface plasmon resonance condition $\text{Re}[\epsilon(\omega)] = -2\epsilon_m$. The resonance occurs at around 400 nm. ϵ_m is assumed to be frequency independent. The figure is adapted from [16].

2.2.2.1. Dependence on dielectric functions

The surface plasmon absorption bands depend strongly on the dielectric function ϵ_m of the surrounding medium and $\epsilon(\omega)$ of the metal particle as they are the basic parameters defining the plasmon resonance condition (Eq. (2.13)). For example, an increase in ϵ_m leads to an increase in the plasmon band intensity and bandwidth, as well as it produces a red shift (shift to higher wavelengths, i.e., to lower energies) of the plasmon band maximum [14] as seen in Fig. 2.4 (wavelength scale) and Fig. 2.5 (energy scale). The curves in Fig. 2.5 represent the spectral positions of plasmon resonances of silver nanoparticles that are embedded in three different media: vacuum ($\epsilon_m=1$), glass ($\epsilon_m=2.25$), and TiO_2 ($\epsilon_m=6.25$). As clearly seen, increases in the ϵ_m values shift the plasmon resonances to the red side of the spectrum.

Figure 2.6 depicts the effect of the dielectric function of the metal (that is the material of the metal) on surface plasmon resonances. Nanoparticles of three different metals are embedded in a same type of glass. It is seen that silver

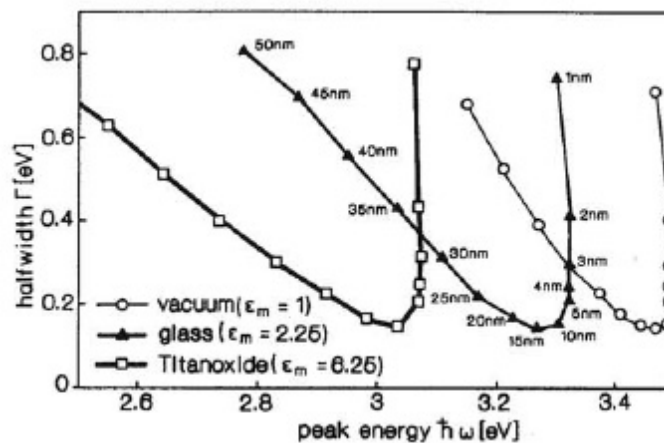


Fig. 2.5. Halfwidths of the surface plasmon bands of silver nanoparticles versus the corresponding peak energy in three different embedding media. The numbers above the points indicate the corresponding particle sizes (diameters). The figure is adapted from [14].

nanoparticles have their surface plasmon extinction band at shorter wavelengths (near to the UV) compared with the gold and copper nanoparticles of comparable shapes and sizes. The extinction band maxima of gold and copper nanoparticles in glass lie in the middle of the visible spectrum.

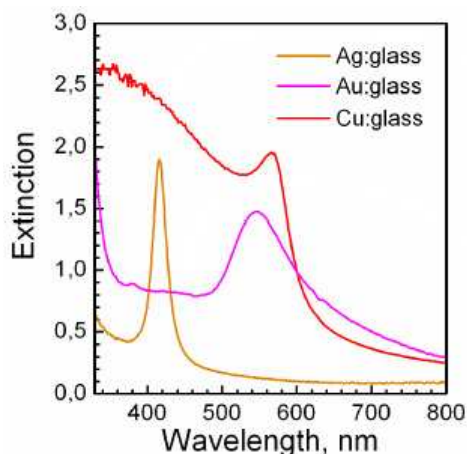


Fig. 2.6. Extinction spectra of glass containing spherical silver, gold and copper nanoparticles. The figure is adapted from [20].

2.2.2.2. Dependence on particle sizes

As it was hinted in Fig. 2.5, the plasmon resonances of metal nanoparticles also depend heavily on particle sizes, as the size modifies the dielectric function of the particle. If the particle size gets below the dimension of the mean free path of the electrons in the metal (≈ 10 nm) [21], the electron scatterings at the particle surface increases mainly the imaginary part of the dielectric function ($\epsilon_2(\omega)$). This is often described as an intrinsic size effect [14, 22]. Going down even to lower particle dimensions (≈ 1 nm) the spill-out of electrons from the particle surface should be taken into account, which results in an inhomogeneous dielectric function. Therefore, very broad plasmon bandwidths are observed for small nanoparticles (Fig. 2.5).

On the other side, as the nanoparticle sizes get larger (bigger than 25 nm), higher-order (such as quadrupolar) oscillations of conduction electrons become important. These contributions induce red shifts to the peak positions of the surface plasmon resonances as shown in Fig. 2.7. This effect for the larger size particle is referred as the extrinsic size effect [14, 19, 22, 24]. In addition to the red-shifts of the

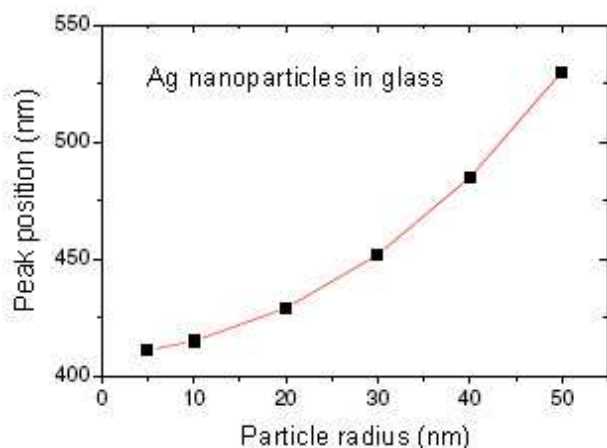


Fig. 2.7. Plot of the spectral position of surface plasmon peaks versus particle sizes for glass-embedded silver nanoparticles. The figure is adapted from [23].

plasmon bands, the bandwidths get broader as the nanoparticle sizes grow. The minimum bandwidths of the plasmon bands are observed for particles with sizes around 15 nm as seen in Fig. 2.5.

2.2.2.3. Dependence on particle shapes

A much more drastic effect on the surface plasmon resonances is found if the nanoparticle shape is changed. It was shown in Fig. 2.6 that spherical nanoparticles exhibit only a single surface plasmon extinction band. However, in the case of e.g. ellipsoidal nanoparticles (such as spheroids), the plasmon absorption splits into two bands corresponding to the oscillations of free electrons along and perpendicular to the long axis of the ellipsoid. The plasmon resonance for the longitudinal mode lies at higher wavelengths while the one for the perpendicular mode lies at shorter wavelengths compared to the single resonance of a nanosphere of the same volume. The spectral separation of the two plasmon bands of the ellipsoidal nanoparticle depends strongly on its aspect ratio, which is defined as the length of the nanoparticle divided by its width (i.e. the asymmetry of the nanoparticle).

The extinction spectra of ellipsoidal silver nanoparticles clearly showing the presence of two extinction maxima are shown in Fig. 2.8(a-b). The numbers above the figures depict the aspect ratios. An aspect ratio of 1 means that the nanoparticle is

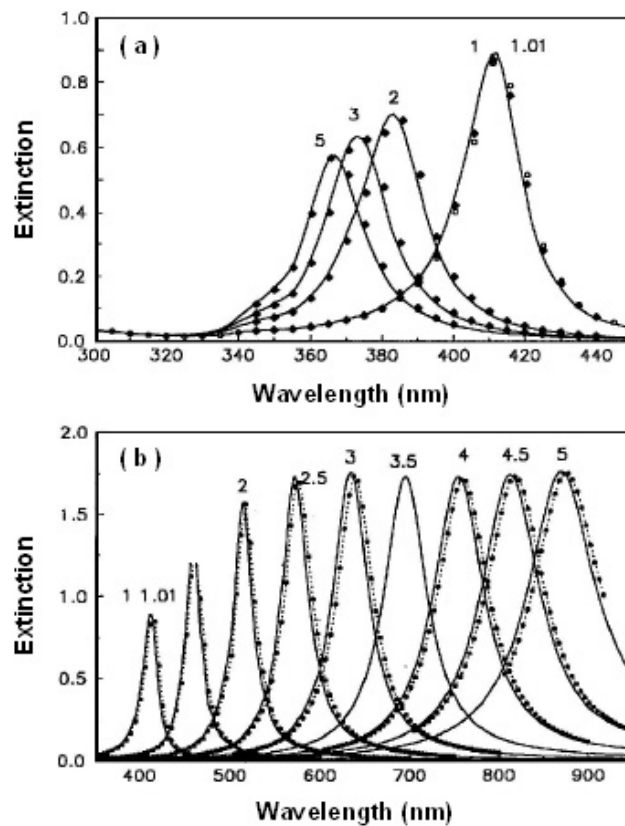


Fig. 2.8. The surface plasmon resonances along the short axes (a) and long axes (b) of nanorods with several aspect ratios. The first plasmon bands of (a) and (b) lie almost at the same spectral position. Increasing the aspect ratio (stated by the numbers above the bands) increases the spectral gaps between the plasmon bands of (a) and (b). The figures are adapted from [23].

indeed a nanosphere, which means that the first plasmon resonances shown in Fig. 2.8(a) and 2.8(b) lie at the same spectral position. As the nanosphere shape is distorted to become an ellipsoid, two resonances of electron oscillations are created, inducing an aspect ratio to the nanoparticle. These aspect ratios are determined by the amount of spectral gaps between the two plasmon resonance bands. The higher the aspect ratio, the more the blue shifts of the extinction bands in Fig. 2.8(a) and the more the red shifts of the extinction bands in Fig. 2.8(b), resulting in a large spectral gap.

2.2.2.4. Dependence on particle concentration

We have seen that the surface plasmon resonances of a metal nanoparticle can be shifted in the spectrum via alterations in particle size and shape. In the case of ensembles of particles, additional shifts are expected to occur due to electromagnetic interactions between the localized modes. For small particles, these interactions are essentially of dipolar nature, and the particle ensemble can in a first approximation be treated as an ensemble of interacting dipoles [11].

In this context, the plasmon resonance of a single spherical metal particle is successfully characterized by the well-known Mie theory using the quasi-static approximation summarized above. However, increasing the metal content in a unit volume (i.e. filling factor, V_{Ag}/V_{total}) of dielectric media decreases the average distances among the particles, which introduces collective dipolar interactions and a modified refractive index of the host media. Therefore, the optical properties of the nanocomposite material are strongly affected by the particle concentration. As an approximation, the Maxwell Garnett theory [3] handles this situation quite successfully and predicts the absorption spectra for high filling factors. Figure 2.9 depicts the calculated absorption spectra for glasses containing spherical silver nanoparticles with different filling factors. Similar to the case depicted in Fig. 2.5 for the particle sizes, increasing the filling factor has basically two effects on the surface

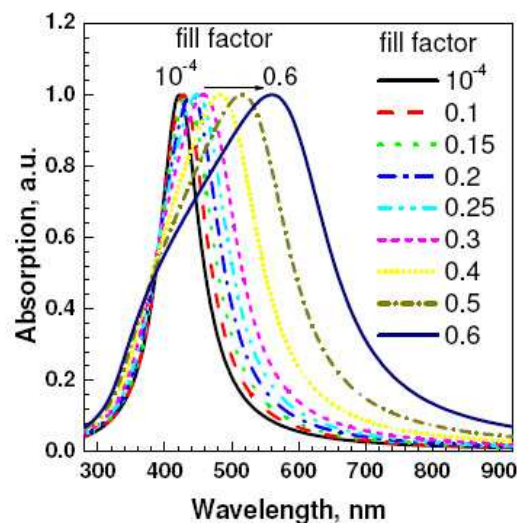


Fig. 2.9. Absorption spectra of composite glasses containing different amounts of silver nanoparticles per unit volume. Calculations are done by Maxwell Garnett theory. The figure is adapted from [20].

plasmon band of the nanoparticles: first is the red-shift of the band maxima, and second is the increasing amount of band broadening.

2.2.3. Optical near fields

As described in previous sections, the surface plasmon resonance on metal nanoparticles can be considered as a simple harmonic oscillator, where the free electrons of the particle oscillate back and forth with respect to the positively-charged ionic background (see Fig. 2.2). These plasmon oscillations not only scatter light to the far field but they also possess near fields when they are excited. In the case of weak excitations, the displacement of the electron cloud is in the linear regime. Increasing the excitation strength changes the oscillation behavior of the electrons, resulting in various nonlinear optical effects because of the induced near-fields. These near fields can be much higher than the exciting optical fields. In the case of spherical nanoparticles, the near fields are induced on the poles of the nanoparticle, depending on the polarization direction of the exciting light. However, in the case of non-spherical particles, the near fields are enhanced mostly at the tips and corners of the particles, in analogy to the collection of electrical charges on sharp edges.

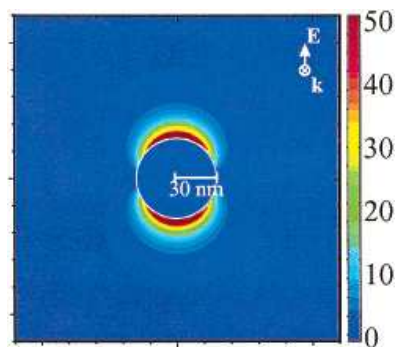


Fig. 2.10. Electric field contours for a 30 nm-radius silver nanoparticle in vacuum. The excitation light is in resonance with the plasmon oscillations. It propagates into the plane with a polarization vector shown by the E-field arrow. The figure is adapted from [25].

Detailed analysis of local field enhancements in metallic nanoparticles have been provided by discrete dipole approximations [25], an example of which is shown in Fig. 2.10. A 30 nm silver nanoparticle is excited by a linearly-polarized light near to the surface plasmon resonance. The electric field contours in the vicinity of the nanoparticle surface are depicted with colors. It is important to see here that the maximum near-field enhancement values are created on the poles of the nanoparticle within a vicinity of a few nanometers, along the direction of the light polarization.

Chapter

3. Laser pulse interaction with metal nanoparticles

The optical properties of metal nanoparticles comprising the surface plasmon resonances were presented in the previous chapter. As a step forward, this chapter is devoted to the general understanding of laser pulse interaction with metal nanoparticles. The aim is to present a temporal sequence of physical events and mechanisms that may take place as soon as the laser pulse starts to interact with the nanoparticle. Depending on the laser parameters (e.g. weak and strong excitation regimes) and nanoparticle properties, one can expect various kinds of physical phenomena (Ch. 3.1). In this context, the literature results from the weak excitation of metal nanoparticles in dielectrics, providing the time scales for the electronic thermalization and electron-phonon coupling, will be summarized in Ch. 3.2.1. Our main focus, however, will be on the mechanisms that happen upon strong laser excitation of silver nanoparticles in glass. Even though it is impossible to account for all complicated many-body interactions among electrons, phonons, ions, etc., in this regime, the theoretical modeling of the possible laser-induced events is very useful in interpreting experimental observations, which we will develop in Ch. 3.2.2. In this manner, the requirements and, if they occur, the consequences of mechanisms affecting the electrical and thermal situation of the nanoparticles will be presented in the last two sections of the chapter.

3.1. Weak and strong excitation regimes

Until now most of the investigations regarding the laser pulse interaction with metal nanoparticles have focused on the weak excitation regime [1]. As suggested by its name, this regime employs weak (i.e. low intensity) laser pulses to excite the nanoparticles, thereby ensuring only weak electrical perturbations to the nanoparticle. Owing to such weak perturbations, the changes induced to the surface plasmon bands of the nanoparticles are transient, that is, totally reversible. By carefully adjusting the wavelength and intensity of the laser pulses, this regime is usually employed to selectively excite the conduction electrons of the nanoparticle. As the nanoparticles absorb very less when the the excitation wavelength is far away from the surface plasmon resonance of the nanoparticles, the laser wavelength can be adjusted in accordance with the aim of the experiment to ensure less perturbation. A well-established all optical method for the investigation of ultrafast response of

nanoparticles upon laser excitation is a pump-probe configuration (see Ref. [2] for a review). After the absorption of the pump pulse, the energy exchange mechanisms among the excited electrons and the relaxation mechanisms between the electrons and lattice phonons are investigated by a much more weaker time-delayed probe pulse [3, 4]. Varying the time delay, the probe pulse maps the changes in the time evolution of optical properties (i.e. transmission or reflection changes) that were induced to the nanoparticle system by the pump pulse. These changes are correlated to both the electron heating and the subsequent cooling dynamics. Owing to the reversible nature of the mechanisms induced to the nanoparticle in the weak regime, the nanoparticle cools down and returns back to its original steady state until the next pump pulse arrives. Therefore it is possible to detect tens or hundreds of probe pulses from the same sample spot for each time delay. The detected probe signals can be averaged, thereby reducing experimental noises. As the nanoparticle is not excited strongly, the acquired data includes the heating and cooling of the electronic system alone without any unwanted influence coming from the third parties, which makes the interpretation easier.

On the other hand, the physical situation of strong excitation employs intense laser pulses that can create persistent (irreversible) changes to the nanoparticle. In the case of near resonance or resonant excitation (i.e. laser wavelength close to the surface plasmon resonance of the nanoparticles) with intense laser pulses, the energy absorbed by the nanoparticle becomes very high, which creates big perturbation for the nanoparticle electrons. As a result of such a strong non-equilibrium, this regime can open up additional channels of relaxation for the nanoparticle electrons in the form of e.g. hot electron emissions. Therefore, the strong regime has a destructive nature, which becomes more drastic with the degree (or strength) of excitation. Further details on the mechanisms that take place in the strong excitation regime, comprising also the studies of this thesis, will be summarized in the following sections. The implementation of a pump-probe technique for the investigation of temporal dynamics, as suggested above for the weak excitation regime, is much more difficult here due to the strong many-body interactions. Additionally, as the nanoparticle is partially modified even after absorbing the first pump pulse, the forthcoming pulses can not see the original particle anymore. This necessitates pumping another part of the sample that contains original nanoparticles for each data point in time (i.e. single shot experiments without averaging). Therefore the interpretation of the temporal data acquired from such single shots becomes much more difficult.

It is clear from the consequences of weak and strong excitation regimes that the wavelength (i.e. frequency) and intensity of the laser pulses are of great importance for the mechanisms generated on the nanoparticle. In general, we can reduce the interaction of a laser pulse with the nanoparticle to simple photon absorption. In atomic terms it is said that a photon can be absorbed by an atom, if the energy of the photon is equal to or greater than the energy gap of the two atomic levels. The absorption of a photon populates the higher energy level E_2 , while the electron population in E_1 is reduced [5] as depicted in Fig. 3.1(a). For example, the absorption of a photon with energy higher than the ionization energy of the material ($E_{\text{photon}} \geq E_i$) leads to the photoionization of the material, where an electron escapes from atom's potential energy. Such single photon ionization processes can take place independent of the laser intensity (i.e., high photon flux), but of course the degree of

ionization will be much higher for high intensities. Therefore, when the laser frequency is high enough, the atomic or bulk properties of the material (such as the dipole moment and absorption) are linearly dependent on the laser intensity. This is indeed the case that covers our studies, namely the resonant (highly absorbed) excitation of silver nanoparticles in glass with intense laser pulses. Further details will be described in the following sections and in Ch. 4.

However, if the photon energy is not enough to ionize the nanoparticle ($E_{\text{photon}} < E_i$) through single photon absorptions, the light intensity becomes much more important. Increasing the laser intensity causes the above mentioned factors to become intensity dependent, which is known as the nonlinear regime. Depending on the photon energy, two or more photons can be absorbed to fulfill the ionization condition (Fig. 3.1(a)). It is also possible with the increasing laser intensity that the potential barrier of the material is deformed so that the electrons can tunnel through the reduced potential to ionize the material (Fig. 3.1(b)). However, the ionization can not take place at all for low light intensities. This is exactly the case (i.e. the low energy and low intensity case) that many of the experiments in the weak excitation regime employ.

Having described the weak and strong excitation regimes in general, we will now present a more rigorous description of the influence of the laser frequency and intensity on laser interaction with nanoparticles. Strong laser interaction with nanoparticles depends on the kinetic energy of the electrons oscillating in the field, and the ionization energy of the nanoparticle atoms. In this context, two parameters are commonly used to characterize the laser interaction with the particle: Ponderomotive energy [6] and Keldysh parameter [7]. Considering an electron in the inhomogeneously oscillating electromagnetic field $E(t) = E \cdot e^{-i\omega t}$ of the laser, the electron experiences a force that originates from second-order terms of the Lorentz force on the nanoparticle. This is called as the ponderomotive force and given by

$$F_p = -\frac{e^2}{4mc\epsilon_0\omega_L^2} \nabla E^2 \quad (3.1)$$

where e is the electron charge, m is the electron mass, E is the amplitude of the electric field, and ω_L is the laser frequency. From the force equation, the

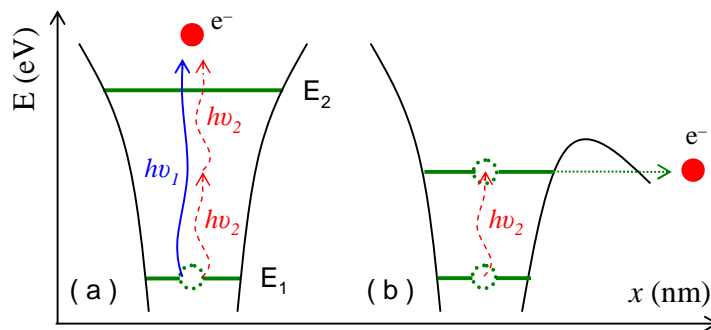


Fig. 3.1. (a) Single photon (with energy $h\nu_1$) and multiphoton (with energy $h\nu_2$) ionization of an atom having two energy levels. (b) Sketch showing the possibility of tunneling ionization of an atom. The atomic potential of the atom is deformed by the laser field.

ponderomotive energy can be found ($F = -\nabla U$) as $U_p = \frac{e^2}{4mc\epsilon_0\omega_L^2}E^2$. Replacing the E -field amplitude with the laser intensity $I = (c\epsilon_0/2)E^2$ this energy can be written as follows

$$U_p = \frac{e^2}{2m\omega_L^2}I \quad (3.2)$$

which describes the cycle-averaged oscillation energy of the electron. As it is seen in Eq. (3.2), the ponderomotive energy is wavelength ($\lambda = 2\pi c/\omega_L$) and intensity dependent. It grows up quadratically with the wavelength and linearly with the intensity. Inputting the e and m quantities, it can be given neatly in the form

$$U_p = 9.34 \cdot \lambda^2 [\mu m] I [10^{14} W / cm^2] \quad (3.3)$$

Having stated the laser frequency (or wavelength) and intensity dependence of the ponderomotive energy, now it is possible to relate this information with the Keldysh parameter γ , which is a practical parameter to distinguish between the strong and weak field regimes of laser interaction with matter:

$$\gamma = \sqrt{\frac{E_i}{2U_p}} \quad (3.4)$$

The comparison between the oscillation energy of the electrons and the ionization energy of the nanoparticle should be made to determine which ionization processes take place. The Keldysh parameter relates the ionization potential of the atom E_i to the ponderomotive energy of the electrons. According to the equations (3.3) and (3.4), the Keldysh parameter increases with increasing laser frequency and when $\gamma > 1$, i.e. $E_i > U_p$, ionization occurs by multiphoton absorption. When $\gamma \approx 1$, tunneling ionization dominates owing to the deformed atomic potential. On the other hand, if $\gamma < 1$, the most prominent mechanism is optical field ionization.

In the following we will describe the ultrafast heating and cooling dynamics of metal nanoparticles, with special emphasis on silver nanoparticles. As mentioned before, the events that take place upon laser interaction with the nanoparticle will be described according to their temporal order. Therefore we will first start with the fastest processes, namely the electronic thermalization of the nanoparticle that happens through electron-electron scatterings. A literature review of the weak excitation regime comprising the electronic thermalization and relaxation in silver nanoparticles will also be given. Afterwards we will describe the electron-phonon couplings in the frame of two temperature model, which we have extended to cover the strong excitation regime conditions. The consequences of the strong excitation regime will be presented at the end of the chapter.

3.2. Ultrafast heating and cooling dynamics of nanoparticles

Figure 3.2(a) shows the electron density of states (DOS) of silver, which has an electronic configuration of the form $\text{Ag}^{47}: 4d^{10}5s^1$. The prominent regions of high density of states, which are associated with the d -bands, located ~ 3 eV below the Fermi level, are clearly seen. These are due to the $4d$ valence bands of the silver. In the case of laser excitation with energy higher than 3 eV, the excitation of these d -band electrons becomes possible and they can make a significant contribution to the thermodynamics of the nanoparticle, thereby increasing the complexity of the thermal description. The details of this scenario can be further investigated by looking at the extinction (i.e. absorption) properties of the nanoparticle.

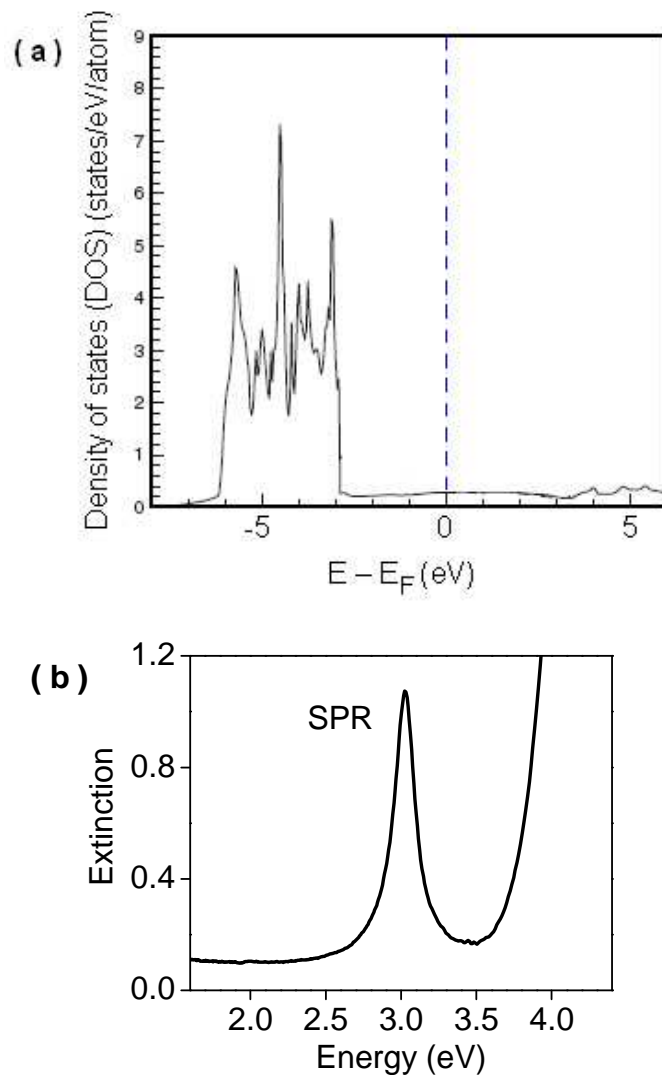


Fig. 3.2. (a) The electron density of states (DOS) of Ag. The graph is adapted from [8]. (b) Extinction spectrum of silver nanoparticles in a glass matrix. The sharp band of the surface plasmon resonances is observed around $\hbar\omega_{sp} = 3$ eV.

Figure 3.2(b) shows the extinction spectrum of $R \approx 15$ nm silver nanoparticles embedded in a glass matrix. The surface plasmon resonance (SPR) is observed to occur at around $\hbar\omega_{sp} = 3$ eV, which covers the intraband transitions of the half filled

s-p conduction bands. Owing to the strong SPR, the nanoparticle absorbs light with frequency at or near to its resonances efficiently. In other words, the excitation light is in resonance with the oscillations of the nanoparticle electrons if it has a frequency close to the oscillation frequency of the electrons. The absorption rise that is observed for higher energies is due to the interband transitions (from the inner *d* orbitals well below the Fermi energy to the conduction band).

3.2.1. Electronic thermalization and electron-phonon coupling

The absorption of a femtosecond laser pulse produces a coherent collective oscillation of the nanoparticle electrons. The strength of the oscillations depends on the mentioned ponderomotive energy of the electrons. The electronic oscillation can be considered as a pulse-induced polarization on the nanoparticle (see, for example Fig. 2.2) that preserves the optical phase memory of the exciting laser pulse. Subsequently on a less than ~ 10 fs time scale after excitation [9], the coherent collective oscillation of the electronic motion decays via phase destructive events (loss of coherence) like hot electron emissions from the nanoparticle (in the case of strong excitation) and electron-electron (*e-e*) scatterings [1], which randomize the momentum. Details and characteristics of possible electron emission processes will be given in the following sections and further in Ch. 5. Here we only consider the dynamics of electronic thermalization (through *e-e* scatterings) and following relaxation (through *e-ph* couplings) in metal nanoparticles in the frame of the weak excitation regime.

The initially deposited pulse energy is dissipated by creating a highly excited ensemble of incoherent electron-hole pairs which do not obey the Fermi-Dirac statistics. The resulting non-Fermi electronic distribution is depicted in Fig. 3.3(a). Electrons having energies between $E_F - \hbar\omega_L$ and E_F are excited above the Fermi energy with final energies between E_F and $E_F + \hbar\omega_L$. The excitation is sketched with rectangular-shaped boxes, whose dimensions are determined by the energy of the exciting laser pulse $\hbar\omega_L$ as the length and the absorbed energy density (i.e. intensity) as the width. Depending on the laser frequency, it is possible to selectively excite only the *s-p* band conduction electrons of the nanoparticle or the core *d*-band electrons below the Fermi level. The excitation intensity will determine how strong the non-equilibrium conditions will be, or in other words how big an athermal electronic distribution will be generated. As mentioned before, it is possible to adjust these laser parameters to achieve various kinds of excitations.

The internal thermalization of the non-Fermi electronic distribution, that is, the redistribution of the excess energy carried by the optically excited conduction electrons, happens through the mentioned inelastic *e-e* scattering processes. It is known that the *e-e* scattering rate is determined by the number of available unoccupied states, which serve as the final states for the scattering processes [9]. For this reason, the *e-e* scattering rate $(\tau_{e-e})^{-1}$ is inversely proportional to the energy above the Fermi level. For the weak excitation regime the scattering rate (and thus the lifetime) of the excited electrons can be estimated within the Fermi liquid theory [10], where the electron interactions can be described by a Coulomb potential screened by both the conduction and bound *d*-band electrons. According to this theory for

electrons with an initial energy E close to the Fermi energy E_F , the $e-e$ scattering rate is given by (for a three-dimensional free electron gas at $T = 0$ K):

$$\frac{1}{\tau_{e-e}} \propto \frac{1}{\sqrt{\epsilon_{sc}} n^{5/6}} (E - E_F)^2 \quad (3.5)$$

where ϵ_{sc} is the core electrons screening amplitude.

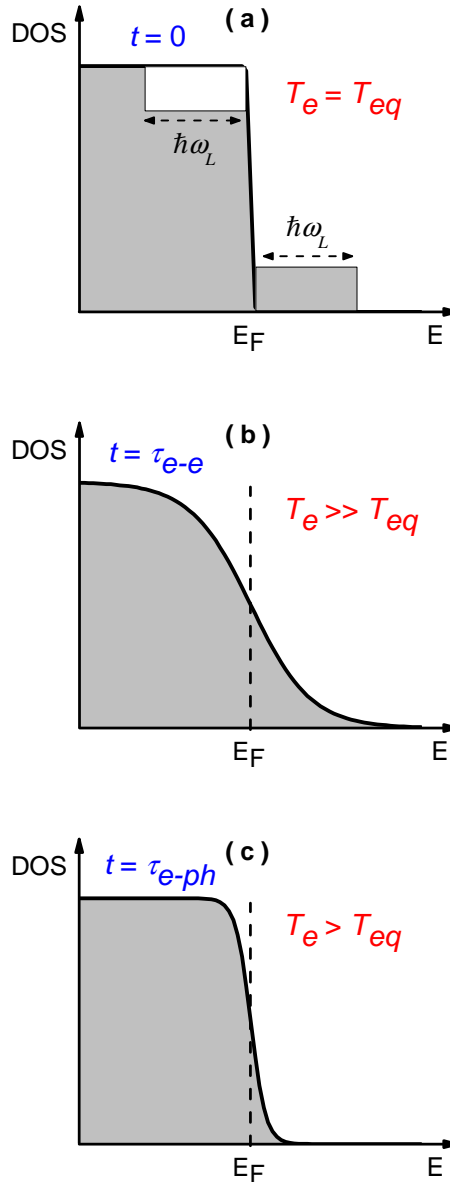


Fig. 3.3. Laser excitation and the subsequent electron dynamics: (a) At $t = 0$ the electronic distribution is at an equilibrium temperature T_{eq} . Absorption of a laser pulse energy density with photon energy of $\hbar\omega_L$ creates a non-thermal electronic distribution represented by the rectangles. (b) The non-thermal electrons thermalize to a hot Fermi distribution ($T_e \gg T_{eq}$) through electron-electron scatterings within several hundred femtoseconds (the time constant is denoted as τ_{e-e}). (c) Electrons cool down by sharing their energy with the lattice through electron-phonon coupling processes (the time constant is τ_{e-ph}), reaching a temperature which is equal to the lattice temperature $T_e = T_l > T_{eq}$.

It is seen that the electronic lifetime depends on the excess energy of the excited electron ($E - E_F$) and the density of the electron gas n . The electronic environment of the nanoparticles is very different compared with the bulk metal because of the strong impact of the surface [11]. On one hand, the wavefunctions of the conduction electrons extend beyond the particle radius, leading to a decrease in their number density n close to the surface. On the other hand, the wavefunctions of the core d -band electrons are localized in the inner region of the nanoparticle. Both effects lead to less efficient screening of the Coulomb potential close to the surface in noble metals, which leads to a higher rate of e - e scattering for smaller nanoparticles [11, 12]. For the case of silver, as the d -bands are localized well below the Fermi level, mostly the s - p energy levels play a role in the relaxation of excited electrons in the weak excitation regime. Depending on the initial electron energy E , the e - e scattering time for a single scattering process is usually on the order of 10 fs [9, 13], and the sum of all the e - e scatterings determines the internal electron thermalization time τ_{e-e} , which is on the order of several hundred femtoseconds. The τ_{e-e} depends on many parameters such as the material of the metal, the embedding medium and the excitation regime.

Measuring the internal thermalization of electrons in the weak regime requires the avoidance of high laser intensities, which otherwise can excite interband transitions and a great perturbation of the electron gas. Tuning the excitation wavelength away from the threshold for interband transitions (i.e. off-resonance excitation) with less energy density pulses maintain the sufficient conditions for the measurements [14]. Considering the Ag nanoparticles in glass (surface plasmon band shown in Fig. 3.2(b)), an off-resonant excitation wavelength would be 800 nm [15], which corresponds to photon energies of 1.55 eV. As described in Ch. 3.1, the applied intensity of the pulse should also be less enough to avoid any possible multiphoton absorption processes.

Using a two-color (infrared pump and ultraviolet probe) femtosecond pump-probe technique, Voisin *et al.* [11] reported an internal electron thermalization time of ≈ 350 fs for 12 nm radius Ag nanoparticles in a BaO-P₂O₅ matrix, which is comparable to the one determined from Ag films [16]. The time it takes for the internal thermalization decreases for smaller nanoparticles, for example $\tau_{e-e} \approx 150$ fs for 2 nm radius Ag nanoparticles embedded in an Al₂O₃ matrix. For the 9 and 48 nm Au nanoparticles in solutions, the decay lifetimes of 500 and 450 fs were found, respectively, for the internal electron thermalization [9]. Figure 3.3(b) shows the equilibrated thermal Fermi distribution following the mentioned e - e scattering processes. The excited electrons possess high energies above the Fermi level, and the resulting temperature of the electronic system is much higher compared with the equilibrium temperature before the laser excitation ($T_e \gg T_{eq}$).

Subsequently, the hot electrons cool *externally* by electron-phonon (e - ph) interactions until the temperatures of the electron gas and the lattice are equilibrated (Fig. 3.3(c)). The resulting electronic temperature is again higher than the equilibrium temperature but less than its peak value ($T_e > T_{eq}$), which is also reflected by the shorter $k_B T_e$ range of the Fermi distribution in Fig. 3.3(c). Since the e - ph interactions occur on a comparable time scale with the internal electron thermalization, a clear separation between e - e and e - ph relaxation as sequential processes is therefore incorrect. That means, the nonthermal electrons of the Fig.

3.3(a) already interact with the phonons during the same time they scatter with themselves to achieve the Fermi distribution of Fig. 3.3(b). This simultaneous e - ph coupling is an important channel of electron relaxation, which heats the nanoparticle lattice in time. As a result, the decay time of the nonthermal electronic population τ_{th} can be determined by the time constant of e - e (τ_{e-e}) and e - ph (τ_{e-ph}) interactions as follows [9]

$$\frac{1}{\tau_{th}} = \frac{1}{\tau_{e-e}} + \frac{1}{\tau_{e-ph}} \quad (3.6)$$

Bigot *et al.* [17] found the internal electron thermalization and e - ph relaxation to happen within about 1 ps for both processes measured on 10 nm Cu nanoparticles embedded in a glass matrix. Normally one can expect that the lattice heating takes longer time compared with the electronic heating, and the maximum lattice temperature cannot reach temperatures as high as electron temperatures since the electronic heat capacity is about 2 orders of magnitude smaller than the lattice heat capacity. These fundamental processes lie at the basis of a wide range of electrical and thermal phenomena in solid state physics. For a better understanding, we will proceed with the two temperature model that describes the thermal situations of electrons and phonons and the heat transfer between these two systems in more detail. We will extend the standard two temperature model to include very high electronic temperatures to account for the conditions of strong excitation regime.

3.2.2. Two temperature model for the strong excitation regime

Upon pulse interaction with the nanoparticle, the electrons heat up gradually to a hot electronic distribution. During and after their heating, the electrons couple with the nanoparticle lattice vibrations (the phonons) and heat up the nanoparticle. The heat gained by the nanoparticle lattice can be found from the heat lost by the electrons using the two-temperature model (TTM) [1, 18], where the heat flow between two subsystems (electrons and lattice) is defined by two coupled differential equations. TTM is the commonly accepted theory to describe the energy relaxation mechanisms between electrons and lattice. The electronic system is characterized by an electron temperature T_e and the phononic system by a lattice temperature T_l . The electron-phonon coupling factor $G(T_e)$ is responsible for the energy transfer between two subsystems. The heat equations describing the temporal evolution of T_e and T_l are given as follows:

$$C_e(T_e) \frac{\partial T_e}{\partial t} = -G(T_e)(T_e - T_l) + S(t) \quad (3.7)$$

$$C_l \frac{\partial T_l}{\partial t} = G(T_e)(T_e - T_l) - C_l(T_l - T_0) / \tau_s \quad (3.8)$$

where $C_e(T_e)$ and C_l are the electronic and lattice heat capacities, respectively. $S(t)$ in Eq. (3.7) is a source term of Gaussian shape describing the absorbed laser pulse energy per nanoparticle, which is given as:

$$S(t) = I \cdot (\sigma_{abs} / V_{NP}) \cdot \exp(-4 \ln 2 \cdot (t / \tau_{FWHM})^2) \quad (3.9)$$

Here I is the peak pulse intensity, σ_{abs} is the absorption cross section of a single nanoparticle, V_{NP} is the nanoparticle volume, and τ_{FWHM} determines the full width at half maximum of the temporal pulse profile. One of the critical terms in Eq. (3.9) is the absorption cross section of the nanoparticle, which is $\approx 3000 \text{ nm}^2$ for a silver nanoparticle in a dielectric environment with refractive index of $n = 1.52$ [19]. This corresponds almost to the refractive index of the glass. The last term in Eq. (3.8) represents heat transfer from the nanoparticle to the surrounding matrix (with $T = T_0$ and the cooling time constant τ_s) through phonon-phonon interactions (i.e. thermal diffusion), which lead to the complete relaxation of the initially absorbed pulse energy.

In the following, we will present the solutions of the coupled heat equations given above. Before doing that, it is necessary to take a look at the temperature dependences of the electronic heat capacity (C_e) and the electron-phonon coupling factor (G), as we know that the strong excitation regime induces very high temperatures to the electronic and phononic systems. The temperature dependence of the C_e changes the evolution of T_e itself, which in turn introduces the temperature dependence to the G factor. For this reason, possible changes of the C_e and G values at high electronic temperatures are expected to play important roles in the thermodynamics of the nanoparticle. Therefore, a better understanding of the nanoparticle dynamics requires a correct modeling of the thermal interactions between electrons and phonons, which is only possible with the closest approximations. In contrast, for the heat capacity of the nanoparticle lattice (C_l) the room temperature values are reasonable approximations, as C_l does not change so much as the temperature increases. For the case of silver, it is known that the change of C_l upon lattice temperature increase by 1500 K is less than 20 % compared with its room temperature value of $3.5 \times 10^6 \text{ Jm}^{-3}\text{K}^{-1}$ [20].

In the literature, C_e is commonly defined by a linear function of electron temperature in the form $C_e(T_e) = \gamma T_e$, where γ is the electronic heat capacity constant. This expression for the electronic heat capacity is only valid at low electron temperatures, where the Sommerfeld expansion of the electronic free energy is commonly used. Electron heat capacity constant of the above expression is given as $\gamma = \pi^2 k_B^2 g(\mathcal{E}_F)/3$ and defined by the value of the electron DOS at the Fermi level, $g(\mathcal{E}_F)$. Within the frame of free electron gas model, γ can also be associated with the free electron number density n and the Fermi energy as $\gamma = \pi^2 n k_B^2 / 2 \mathcal{E}_F$ [21].

However, the Sommerfeld expansion is no more valid at high electron temperatures, and the C_e calculation should include the full spectrum of the electron DOS by taking the derivative of the total electron energy density with respect to the electron temperature [21], as given in the following:

$$C_e(T_e) = \int_{-\infty}^{\infty} \frac{\partial f(\mathcal{E}, T_e)}{\partial T_e} g(\mathcal{E}) \mathcal{E} d\mathcal{E} \quad (3.10)$$

where $g(\varepsilon)$ is the electron DOS at the energy level ε (see Fig. 3.2(a) for Ag), and $f(\varepsilon, T_e)$ is the Fermi distribution function of the form $f(\varepsilon, T_e) = \frac{1}{\exp[(\varepsilon - \varepsilon_F)/k_B T_e] + 1}$.

The temperature dependence of the C_e for silver is depicted in Fig. 3.4. The deviation between the linear temperature dependence of the C_e obtained from the free electron gas model (dashed line) and the nonlinear temperature dependence of C_e calculated from Eq. (3.10) (solid line) is clearly seen above T_e values of ~ 5000 K. The free electron gas model approximates the C_e values very well up to 5000 K ($\gamma \approx 63 \text{ Jm}^{-3}\text{K}^{-2}$ is used for Ag [22]), and indeed the calculations considering the full DOS (Eq. (3.10)) follow closely the same linear dependence. However, further increases of the electron temperatures cause significant changes in the C_e as a result of the contributions coming from the core electrons, compared with the commonly used linear approximation. Therefore, employing the linear C_e dependence in the TTM could definitely result in an overestimation of the electron temperatures, which proves to be inappropriate for the strong excitation regime (when T_e is higher than several thousands of Kelvins). This nonlinear behavior of the C_e for high electron temperatures depends strongly on the electron DOS and should be expected to have different behavior for different metals. Calculations on other noble metals (such as Cu and Au) also show an increase of the C_e values for higher T_e [8], which is not necessarily the case for other metals.

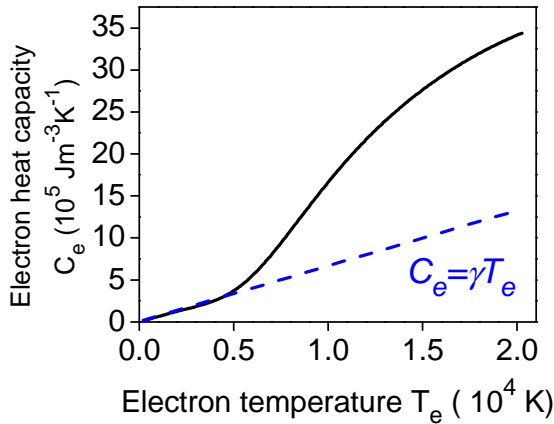


Fig. 3.4. Electron temperature dependence of the electronic heat capacity C_e of silver. The figure is reproduced from the data given in [8]. The dashed line shows the linear temperature dependence of C_e with $\gamma = 63$.

The temperature dependent form of the C_e , which is plotted in Fig. 3.4, will be used in all our TTM calculations in the following. Since C_e depends on the electron temperature, the electron-phonon coupling is also expected to have temperature dependence. To develop a similar temperature-dependent expression for the electron-phonon coupling factor ($G(T_e)$), we will again consider the classical description of the G within the free electron gas model first. Kaganov *et al.* suggested that the electron-lattice energy exchange rate per unit volume

$\frac{\partial E_e}{\partial t} = G(T_l - T_e)$ can be expressed in terms of the electron relaxation times at T_e and

T_l as [18, 23] $G = \frac{\pi^2}{6} \frac{m C_s^2 n}{\tau_{e-ph} T_e}$, where m is the effective electron mass, C_s is the speed

of sound, n is the number density of electrons, and τ_{e-ph} is the electron-phonon

scattering time. The electron-phonon scattering time is proportional to the inverse of the lattice temperature and when $T_e = T_l$, τ_{e-ph} becomes $1/T_e$, which results in a constant value for the G factor [8].

For this reason, G has been defined in the literature as a constant, temperature independent value that is found either by the above model or by best-fitting the values from the experimental results. Typical G values used for silver range between 3×10^{16} to $3.5 \times 10^{16} \text{ Wm}^{-3}\text{K}^{-1}$ [1, 14, 24, 25]. This constant G value is depicted in Fig. 3.5 with the dashed line.

As it has been mentioned before, high electronic temperatures trigger the thermal excitation of the d -band electrons located below the Fermi level. For this reason dramatical changes are expected for the rate of the electron-phonon energy exchange. Therefore, the correct treatment of the G factor in the strong excitation regime requires again the consideration of the full spectrum of electron DOS (as it was done above for the C_e). The resulting expression for the temperature dependent electron-phonon coupling factor is given by [8]

$$G(T_e) = \frac{\pi \hbar k_B \lambda \langle \omega^2 \rangle}{g(\mathcal{E}_F)} \int_{-\infty}^{\infty} g^2(\mathcal{E}) \left(-\frac{\partial f}{\partial \mathcal{E}} \right) d\mathcal{E} \quad (3.11)$$

where λ denotes the electron-phonon coupling constant, and the value of $\lambda \langle \omega^2 \rangle$ is 22.5 for silver. The solid line in Fig. 3.5 depicts the calculations out of this equation. It shows a nearly constant electron-phonon coupling term up to electron temperatures of ~ 5000 K. At higher temperatures a significant strengthening of the G factor is observed when a large number of d -band electrons are thermally excited and contribute to the electron-phonon energy exchange. The enhancement of the electron-phonon coupling at high electron temperatures implies a faster energy transfer from the hot electrons to the lattice. As in the case of C_e , the temperature dependence of the G factor will also be used in all our TTM calculations.

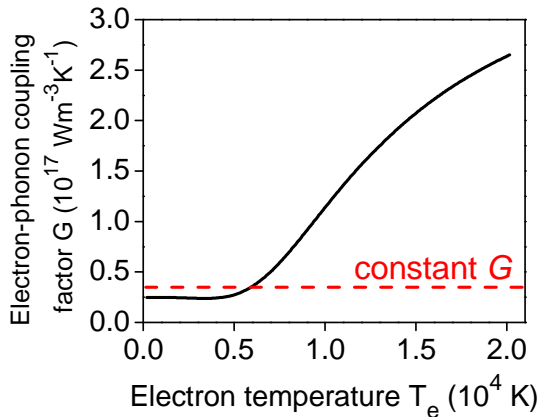


Fig. 3.5. Electron temperature dependence of the electron-phonon coupling factor G of silver. The figure is reproduced from the data given in [8]. The dashed line marks the value of constant G value commonly used in the literature.

A consequence of the temperature dependent electron-phonon coupling term is that the electron-phonon relaxation times (τ_{e-ph}) increase with increasing electron temperatures and hence the applied laser pulse energy [26, 27]. Therefore, slightly different electron-phonon relaxation results that are presented in the literature could

be explained by the temperature dependence of the electron-phonon relaxation. Several time resolved studies including Cu nanoparticles in glass [28], Ag nanoparticles in glass [24] and Ag and Au nanoparticles in solutions [27] showed that a limiting value of up to 4 ps for the $e-ph$ coupling time was reached for high intensity laser excitations.

Besides the laser energy dependence of the electron-phonon relaxation dynamics, there is also the size dependence in nanoparticles. It is expected that in nanoparticles smaller than the mean free path of the conduction electrons (~ 40 nm in silver [21, 29]), an enhanced electron-surface scattering leads to a faster electron-phonon relaxation if the collisions of the electrons and the surface are inelastic. For colloidal solutions containing Au nanoparticles of 9 and 48 nm, the electron-phonon interactions were found to have lifetimes of 1.6 and 1.7 ps, respectively [9], which are very near values to each other. However, the electron-phonon relaxation time was observed to decrease from 800 to 500 fs for silver nanoparticles in glass as the size is reduced from 30 nm to below 8 nm [15], which can be due to an increased probability of electron-surface scattering in these small particles.

As we have established the wide range of temperature dependences for the C_e and G parameters in this section, we can now solve the coupled heat equations (Eqs. 3.7 and 3.8) for the quantitative modeling of the energy relaxation dynamics followed by the strong irradiation of silver nanoparticles. It was already mentioned that the strong irradiation regime creates huge electron-phonon non-equilibrium conditions due to the very small heat capacity of electrons (at room temperature) and the finite time needed for the electron-phonon equilibration. Thus the high energy fs pulse transiently raises the T_e over several thousands of Kelvins while the lattice still remains cold.

As an illustration to this regime, Fig. 3.6(a) and Fig. 3.6(b) depict the results of TTM calculations for the case of a single silver nanoparticle excited by a 100 fs pulse with an intensity of 0.3 TW/cm^2 (above the permanent nanoparticle shape modification threshold [30]) and central wavelength of 400 nm ($\hbar\omega_L = 3.1 \text{ eV}$), i.e., close to the surface plasmon resonance. The mentioned intensity corresponds to an energy density (i.e. fluence) of approximately 15 mJ/cm^2 . It is easily seen that, upon absorbing the laser pulse energy, the conduction electrons of the nanoparticle gain very high temperatures (up to 10^4 K) within the pulse. Reaching the maximum T_e , the hot electronic system heats the cold silver lattice to a region of temperatures above the melting point of (bulk) silver within a few picoseconds. The electronic and lattice temperatures meet at a value near 1500 K, 30 ps after the pulse interaction (Fig. 3.6(b)). After this time, the equalized temperatures of T_e and T_l decrease together as the nanoparticle cools down to the surrounding glass matrix. It is seen that the silver lattice temperature of the nanoparticle stays above the melting temperature of bulk silver until around 100 ps. This suggests the plausibility of the melting of nanoparticles in such a short time. Plech *et al.* indeed observed the melting of gold nanoparticles suspended in water within 100 ps [31] by time-resolved X-ray scattering studies after strong laser pulse excitation with fluences above $\sim 15 \text{ mJ/cm}^2$ [32]. We should however note for our calculations that we do take into account the energy losses due to possible electron emission processes from the nanoparticle, which are additional cooling mechanisms of the electronic sea. The details of these electron emission processes will be considered in the next section.

Figure 3.6(c) shows the dependences of electronic and lattice temperature maxima on a wide range of applied energy densities, starting from very weak and going up to extreme irradiation conditions. The weak regime (up to T_e values of 5000 K) shows a rapid increase in T_e owing to the very low electronic heat capacity (C_e) in this interval. However, this regime does not heat up the lattice efficiently due to the less coupling (G) between two subsystems for such temperatures. Further increases in the energy density of the pulses cause higher T_e values, but the increase in T_e slows down due to the increasing C_e value. The lattice temperatures are also observed to increase with a higher slope in this regime as a result of the increasing efficiency of the G factor. If we were to employ standard linear values for C_e (i.e. $C_e(T_e) = \gamma T_e$), which is the trend shown by the linear regime depicted up to 5000 K in Fig. 3.6(c), the electronic temperatures would be very much overestimated for the pulses of high energy densities. For example the pulse of energy density 15 mJ/cm^2 (used in the presented TTM calculations) would be estimated to induce $\sim 10^5 \text{ K}$ of maximum T_e and very high resulting T_l values, which is definitely not true.

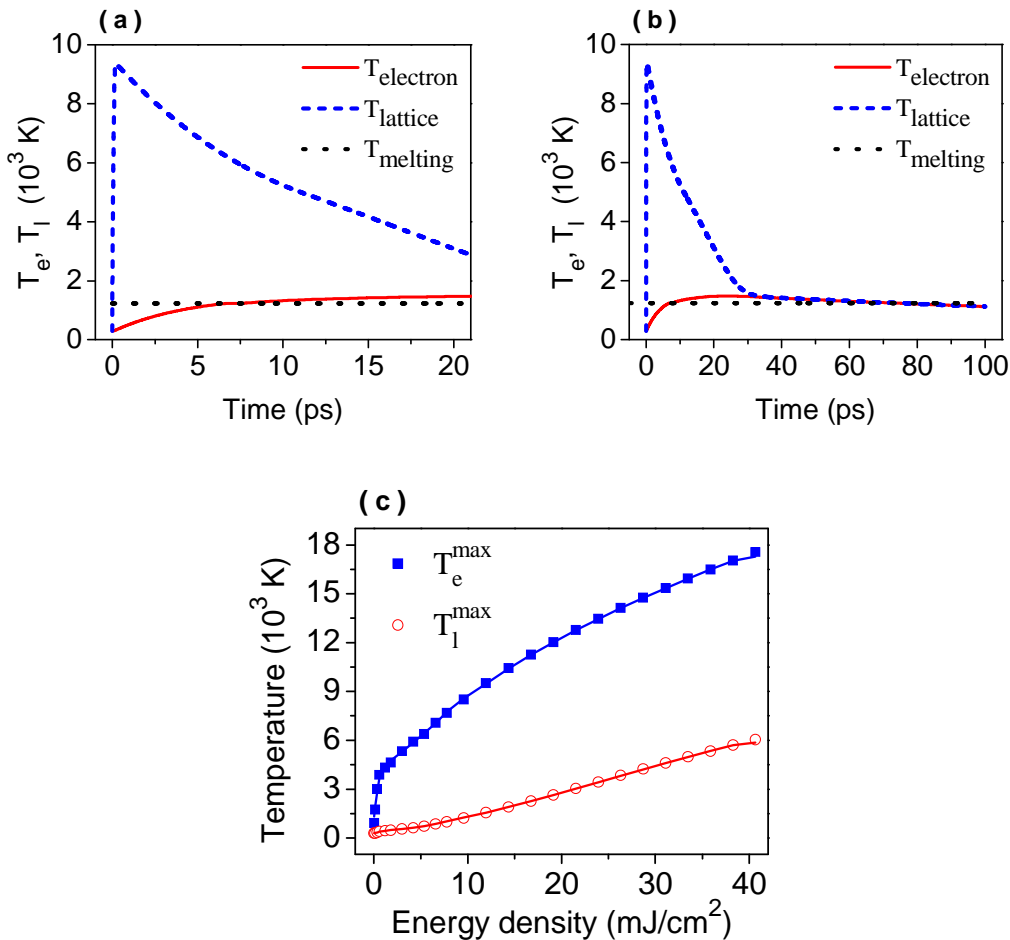


Fig. 3.6. Time evolution of electronic and lattice temperatures of a silver nanoparticle following the absorption of an intense fs laser pulse (around 15 mJ/cm^2 of energy density): (a) up to 20 ps, (b) up to 100 ps time scale is shown. The dotted line at 1235 K marks the melting temperature of bulk silver. (c) The dependences of electronic (blue squares) and lattice (red dots) temperature maxima on a wide range of laser energy densities.

The above given theory describes only the heat transfer between the electrons and the nanoparticle lattice. To get the complete thermodynamical picture of the nanoparticle and the surrounding glass system, the temporal evolution of the heat transfer from the nanoparticle to the glass matrix can be considered by thermal diffusion. The excess energy of the nanoparticle is released to the surrounding via phonon couplings across the nanoparticle-glass interface [33, 34]. Considering the nanoparticle as a hot droplet in a cold glass surrounding, an initial spherical temperature distribution can be ascribed to the system. For $r \leq R$, $T(t = \tau_{e-ph}) = T_{max}$, and $T(t = 0) = T_0$ (300 K) for $r > R$, where R is the radius of the nanoparticle, and T_{max} is the maximum temperature achieved in the nanoparticle lattice. Cooling of the nanoparticle (and heating of the glass matrix) can be calculated considering the heat flow from the hot nanoparticle to the glass through infinitesimal concentrated spherical shells. As the thermal diffusivity of Ag ($123 \text{ nm}^2/\text{ps}$) is much higher than that of the glass ($0.5 \text{ nm}^2/\text{ps}$), the spatial temperature changes within the nanoparticle can be neglected. The temporal and spatial evolution of the heat transfer within the glass can be calculated by the radial heat equation, where the rate of temperature change ($\partial T(r,t)/\partial t$) is proportional to the curvature of temperature density ($\partial^2 T(r,t)/\partial r^2$) through the thermal diffusivity (χ) of the glass medium as

$$\frac{\partial T(r,t)}{\partial t} = \frac{\chi}{r} \frac{\partial^2 [rT(r,t)]}{\partial r^2} \quad (3.12)$$

The time scales for the particle cooling range from tens of picoseconds to nanoseconds, depending on the the laser excitation strength, the size of the nanoparticle and surrounding environment [34, 35]. However, the thermal diffusion alone cannot account for the full relaxation and cooling mechanisms of the nanoparticle under the strong excitation regime. As it was mentioned before the ionization of the nanoparticle and the consequent dissolution (ion emission) mechanisms should be taken into account as effective cooling processes. The emitted electrons and ions heat the glass matrix in the vicinity of the particle very rapidly compared with the normal heat conduction described above.

3.2.3. Nanoparticle ionization

It is obvious that the response of the nanoparticle to the laser excitation shows up in the electronic degrees of freedom at first owing to the huge mass difference between electrons and ions. Only in strong non-equilibrium conditions (due to strong laser excitation) the ionic degrees of freedom are affected through mechanisms like Coulomb explosion, which will be explained soon. In principle strong non-equilibrium conditions trigger some electronical and thermal processes that play important roles for the permanent shape modifications of nanoparticles. One of the most important mechanisms responsible for permanent shape modifications is the laser-induced ionization of the nanoparticle (i.e. electron emissions from the nanoparticle). Therefore, we have to investigate the possible electron emission processes in more detail.

As mentioned before, the interaction of an intense laser pulse with the nanoparticle enhances the oscillation amplitudes and the ponderomotive energy of

the conduction electrons. If the applied laser pulse is close to the surface plasmon resonance wavelength of the nanoparticle, the oscillation amplitudes of the surface plasmon waves can overcome the excitation amplitude by typically two orders of magnitude (for silver nanoparticles with $R \approx 15$ nm) [36]. This means a strong enhancement of the local electromagnetic field in the vicinity of the nanoparticle [32]. As a result of such high fields, the collective charge density oscillations can be perturbed by electron emissions from the nanoparticle. This is the fastest damping mechanism of the surface plasmon oscillations occurring from the first plasmon oscillation period on [37, 38]. As described in Eq. 3.4 the electron emission processes are closely related to the ionization energy E_i of the nanoparticle.

Figure 3.7 depicts the excitation dynamics of a small metallic nanoparticle that is excited by a ~ 100 fs laser pulse. The schematics of the subsequent nanoparticle dynamics during and after the laser pulse are depicted in their temporal order from left to right. The first panel shows that the time-dependent oscillating electric field of the laser pulse induces dipole oscillations to the nanoparticle electron cloud (represented by gray shaded areas) with respect to the background ionic lattice (black balls). These charge-density oscillations (the surface plasmons) are localized at the interface of the nanoparticle and the surrounding medium. According to Mie theory [39], the surface plasmon oscillations of spherical particles are either dipolar or multipolar in character depending on their sizes [40]. For particles having sizes much smaller than the wavelength of the exciting electromagnetic field ($d \ll \lambda$), it is sufficient to consider only the first term of the multipolar expansion, i.e., the dipolar term (see Ch. 2.2.1 for details). The dipole oscillations follow the laser polarization direction, which is shown with the arrow in Fig. 3.7. The electronic oscillations have a Mie plasmon period (τ_{pl}), which is different for different nanoparticles. The figure reads the plasmon period of 1.5 fs for small Na clusters.

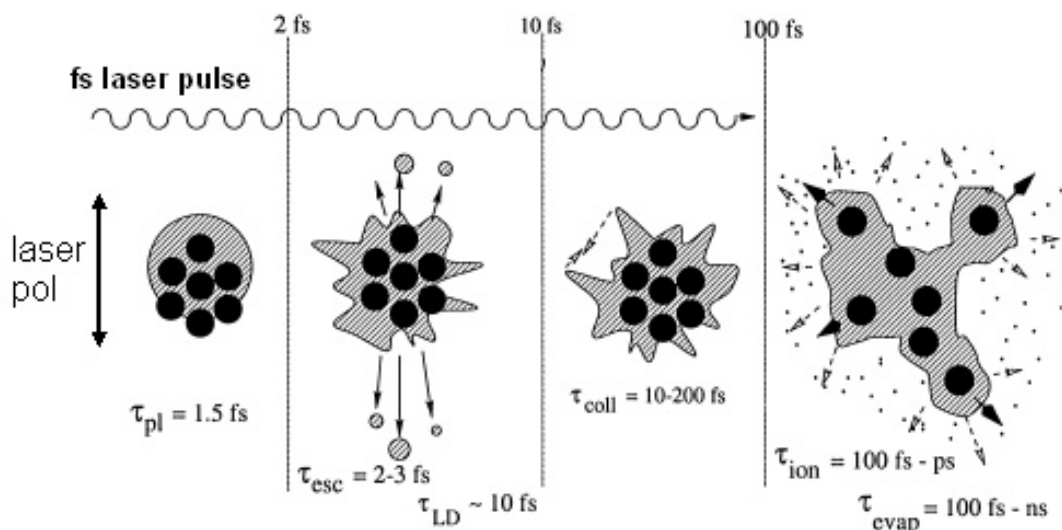


Fig. 3.7. Schematic overview of the typical dynamical processes in metal nanoparticles upon intense fs laser pulse excitation. Gray shaded areas represent electrons, and black balls represent ions. First panel shows the collective charge-density oscillations of the nanoparticle; the second one corresponds to direct electron emissions; the third panel shows the electron-electron relaxation processes and gradual coupling to phonons and the fourth panel shows the Coulomb explosion. The figure is adapted from [37].

The energy given to the hot electrons dissipate successively over various degrees of freedom. The fastest of these processes is the direct, field-driven electron emission (escape) from the nanoparticle, which perturbs (or damps) the coherence of the electronic oscillations and creates electron-hole pairs. The time scale of this process (τ_{esc}) is the first few plasmon oscillation periods. This process is also in analogy with Landau damping of the plasmon into an electron gas, with time scales of $\tau_{LD} \sim 10$ fs for small clusters with up to 1000 atoms [37]. In the validity regime of the dipolar oscillations, hot electrons can be injected into the surrounding glass matrix along the direction of the laser polarization during interaction with the applied pulse. If the emitted electrons return back to the nanoparticle, we cannot consider the ionization of the nanoparticle. Therefore the probability of this direct field-driven electron escape process is clearly correlated to the availability of electronic states of the surrounding medium (for example, glass in our case). In addition, the excitation energy of the laser ($\hbar\omega_L$) and its intensity are also decisive parameters for the directed electron emissions. If the photon energy is high enough, electrons can jump the gap between the conduction bands of the nanoparticle to the glass conduction band(s) via single photon absorption. For these reasons, the investigation of the band structures of silver nanoparticles together with the surrounding glass matrix is of high importance for the feasibility of nanoparticle ionization processes, which will be presented in Chapter 5.4.

Electrons being emitted during the laser pulse interaction will be driven by the strong, oscillating electric field and therefore generate an anisotropic distribution of emission directions, obviously given by the electric field oscillations (polarization) of the laser pulse. The anticipated 100 fs pulses at $\lambda = 400$ nm correspond to 75 full oscillation cycles with mostly very high amplitudes. A simple estimate shows that a conduction band electron of the nanoparticle can gain a linear acceleration of around 10^{20} m/s² upon encountering a linear-polarized pulse of 0.3 TW/cm² intensity (corresponding to an electric field amplitude of 10^9 V/m) within the half plasmon period. This is indeed a huge electric field amplitude on the nanoparticle. In the absence of any damping, the above acceleration can push the electron approximately 0.1 nm away from the nanoparticle surface. The enhanced electric field at the particle-glass interface [36] can increase this value to approximately 10 nm. Electrons driven so far away from the nanoparticle have left the region of the strongest field enhancement, will thus experience a weaker backward force due to the reversed field of the next half plasmon period, and may finally be trapped in the glass matrix. These numbers make plausible that under the specified conditions there is a non-negligible probability for emission of even 'cold' electrons.

In the temporal order, the next step of electron dynamics is the internal thermalization of the remaining nanoparticle electrons through electron-electron collisions, which is sketched in the third panel of Fig. 3.7. The physical details of these processes have been summarized in Ch. 3.2.1 with time scales on the order of several hundred femtoseconds. We have stated that the exact thermalization time depends on many parameters such as the material of the nanoparticle, the embedding medium and the strength of the excitation regime. For small Na clusters the adapted figure reads this value to be up to τ_{coll} (i.e. τ_{e-e}) ≈ 200 fs. These $e-e$ collisions are further damping mechanisms for the electron oscillations that drive the electron cloud towards thermal equilibrium [37].

The ionization mechanisms are categorized according to their nature of occurrence through direct (i.e. field-enhanced) and thermal electron emissions. The first one is due to the mentioned very fast, direct electron emissions. On the other hand, the second process goes on over long time scales, which is due to the high temperature state of the electronic system, namely the thermal electron emissions or evaporations (denoted with the time scale τ_{evap}). Even though the direct electron emissions happen only during the pulse interaction, thermal electron emission processes start after the pulse has gone away and continue to happen as long as the electrons possess high temperatures. This is sketched with the faint arrows and dust in the last panel of Fig. 3.7. As a final remark, it is important to notice that as the direct electron emissions are field-driven in nature, they have the directional character along the pulse polarization. This is because of the dipolar oscillations of the Mie plasmon resonances in small nanoparticles. Therefore, there will be a non-homogenous electron concentration along the poles of the nanoparticle as long as these electrons are trapped in the conduction band(s) of the glass. On the other hand, the thermal electron emissions are isotropic, that is, they are homogeneously spread around the glass conduction band(s) surrounding the nanoparticle. Considering the anisotropy of the laser-irradiated nanoparticles (see Ch. 4.2), these two groups of electron emission processes must have a contribution to the final shapes of the nanoparticle. The detailed analysis regarding these ideas will be revisited in Ch. 5.

3.2.4. Nanoparticle dissolution via Coulomb explosion

As mentioned before, the high temperatures induced to the nanoparticle electrons and lattice are expected to trigger some mechanisms that we know to cause nanoparticle shape transformations. The nanoparticle gets positively-charged (due to the emitted electrons) and hot over time; therefore it becomes unstable electrically and thermally. The answer to the question, asking what happens to the nanoparticles after establishing such instability is given by the experimental observations. From luminescence and extinction spectra [41], it is known that Ag ions are being emitted into the glass matrix upon femtosecond laser irradiation. TEM pictures [42, 43] showed that this ion emission leads to partial dissolution of the nanoparticles, creating small Ag aggregates around the remaining nanoparticle. So it is obvious that after a few picoseconds already some electrons have left the nanoparticle, i.e. the nanoparticle is then positively charged and very hot; electric potential and thermal energy can overcome the binding energy of Ag ions, which are being emitted into the surrounding glass matrix [37, 41, 44]. This case is sketched in the fourth panel of Fig. 3.7 for the small Na cluster.

The physical concept behind these ion emission processes is mainly the so called Coulomb explosion [44], which is a direct consequence of the nanoparticle charging. The repulsive Coulomb forces among the accumulated charges lead to the dissolution (destruction) of the nanoparticle. Even extreme cases of nanoparticle dissolution mechanisms were observed for nanoparticles in aqueous medium [45], where not only the ions but also some small fragments could leave the nanoparticle because of the soft surrounding. In the case of rigid matrices surrounding the nanoparticle, such big fragmentation is not possible. Nevertheless, independent of the way it happens, the total volume of the nanoparticle is reduced over time due to material ejections. Additionally, some part of the energy will be taken from the

nanoparticle and, via kinetic energy of the ions, be transferred to the glass when the ions are trapped there, which is also an additional cooling mechanism of the nanoparticle as was mentioned before.

To serve for the general understanding, we can say for all the emitted electrons (field-driven and thermal) that they can lose their energy rapidly and are eventually trapped at local potential minima forming color centers in the glass [41]. These trapped electrons play an important role in reducing the emitted Ag cations at later times. The modified anisotropic shapes of the nanoparticles can be associated with the distribution of trapped electrons in the glass matrix, if we assume a non-homogenous electronic distribution (the anisotropy from field-driven emissions plus the isotropy from thermal emissions) that is trapped around the nanoparticle. The experimental observations and analysis regarding these electron and ion emission processes will be presented in the following chapters.

Chapter

4. Samples and the experimental apparatus

In the previous chapters, we have introduced the general optical properties of metal nanoparticles embedded in dielectric media (Ch. 2) and the consequences of laser pulse interaction with such nanoparticles (Ch. 3). The experimental work covered in this thesis employed femtosecond laser pulses for the structural modifications of glass-embedded silver nanoparticles. Therefore, in this chapter, we will first give a brief description of both the samples and the experimental apparatus. The first two parts of the chapter will be devoted to our samples before and after laser irradiations, respectively. The concept of laser-induced optical dichroism as a result of nanoparticle shape modifications will be presented. Regarding the experimental apparatus, the laser systems will be described with emphasis on spatial and temporal characterization of femtosecond laser pulses. The chapter will be concluded with the description of the experimental technique that we use to investigate the temporal dynamics of laser-induced shape determining mechanisms in glass-embedded silver nanoparticles.

4.1. Composite glass containing silver nanoparticles

The samples studied in this thesis consist of soda-lime glasses that contain spherical silver nanoparticles in a thin surface region. The samples were prepared by CODIXX AG [1] (as intermediate products for the manufacturing of broadband polarizers) from a float soda-lime glass by the Ag-Na ion exchange method followed by annealing in H₂ reduction atmosphere [2]. This technique results in the formation of spherical silver nanoparticles of ~ 30 nm mean diameters, which are continuously distributed in a thin surface layer of approximately 6 μm thickness of glass.

Size and distribution of silver nanoparticles change strongly in the depth of the glass, which can be controlled by adjusting several parameters such as the temperature and the time of Ag-Na ion exchange processes, and the annealing time during H₂ reduction atmosphere. The volume filling factor (V_{Ag}/V_{total}) of Ag nanoparticles near to the surface of glass is measured to be around 0.7 and decreases gradually in the depth [3, 4]. The total thickness of the host glass plate is 1 mm. To achieve samples with very less filling factors and therefore to get isolated nanoparticles, the upper layers of the glass with the maximum filling factor were

etched away. At the end, the final filling factor of around 10^{-3} was achieved in a very thin ($\sim 2 \mu\text{m}$) surface layer of glass. As the nanoparticles are sufficiently dispersed for such low filling factors, they may be treated as being isolated.

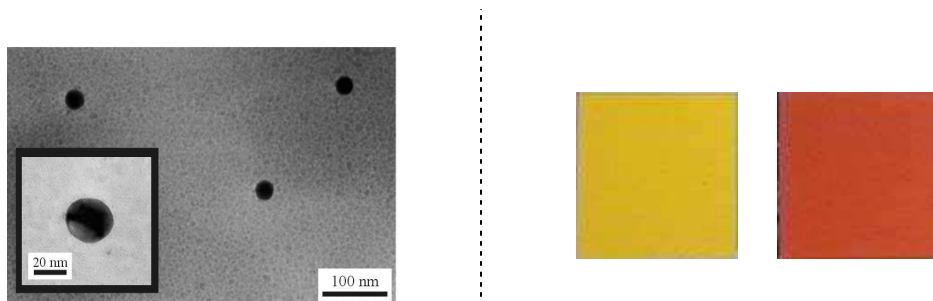


Fig. 4.1. Left panel: Tunneling electron microscope image of spherical silver nanoparticles embedded in soda-lime glass matrix (from [5]). Owing to the very less filling factor, the nanoparticles are far away from each other. Right panel: Glass samples that contain metal nanoparticles. The glass with pale yellow color hosts silver nanoparticles and the glass with reddish color hosts gold nanoparticles.

Figure 4.1 shows tunneling electron microscope images of spherical Ag nanoparticles embedded in glass with very low filling factors. The typical distance between nanoparticles is on the order of several hundred nanometers, which is enough to prevent any interaction. The right panel of Fig. 4.1 shows the pale yellow colored glass, which hosts these spherical Ag nanoparticles with low filling factors. The yellowish color is due to the strong optical absorption of silver nanoparticles in the near UV region. As mentioned in Ch. 2, the optical absorption in nanoparticles is governed by the surface plasmon absorption bands. Figure 4.2 depicts the corresponding surface plasmon resonance of the pictured glass-embedded Ag nanoparticles, which displays a very prominent absorption peak around 413 nm.

As a comparison to our glass samples that contain silver nanoparticles, a picture of a similar glass but containing embedded gold nanoparticles is shown on the right panel of Fig. 4.1. Owing to the comparably broad surface plasmon absorption of gold nanoparticles around 550 nm (see f.e. Fig. 2.6), the gold nanoparticles absorb the green and yellow components of the visible spectrum. Therefore the glass displays a reddish color, which is the complementary color of green.

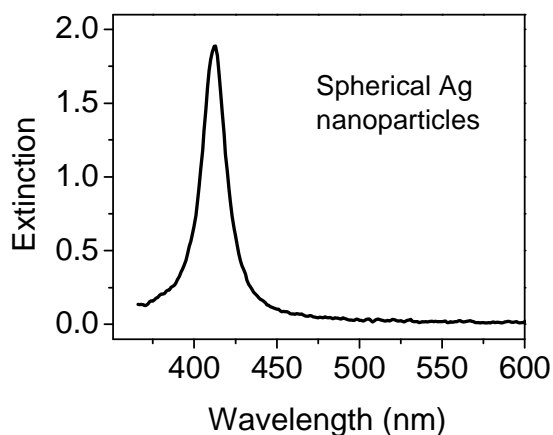


Fig. 4.2. A typical extinction spectrum of spherical silver nanoparticles in glass. The extinction maximum is around 413 nm, which is responsible for the pale yellow color of the glass.

4.2. Laser-induced dichroism in composite glass

High intensity femtosecond laser irradiation of composite glass that contains silver nanoparticles was shown to induce optical dichroism (i.e. polarization-selective absorption of light) to the irradiated region of the glass sample [6, 7]. A sketch of the laser irradiation of a glass sample containing spherical silver nanoparticles is shown in Fig. 4.3. The laser irradiation changes the original color of the glass (the pale yellow) into some darker colors. The different colors of the irradiated areas depend strongly on the irradiation parameters such as the laser wavelength, the pulse intensity and the total number of pulses applied per area. When viewed with a polarizer these different colors display different contrasts, which indicate the polarization-sensitive absorption, that is, the dichroism.

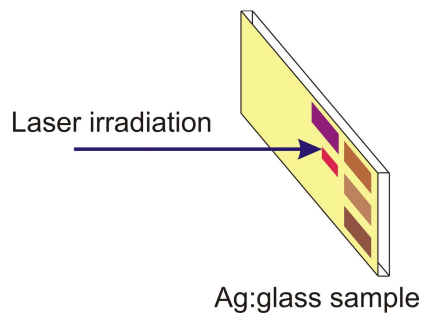


Fig. 4.3. Laser irradiation of glass containing spherical silver nanoparticles. Different colors of irradiated areas can be produced by varying the irradiation parameters. The colors are due to the non-spherical shapes of the modified nanoparticles.

Two polarization-dependent (i.e. polarized) photos of a single glass sample irradiated by linearly-polarized fs laser pulses are shown on the left panel of Fig. 4.4. The color differences of the irradiated areas are again due to the differences in irradiation parameters. The photos were taken by using a film polarizer to see the polarization dependences of the areas. It is indeed seen that the laser irradiated areas display a strong dichroism. Bright colors (due to higher light absorption) are observed when the polarizer is aligned parallel to the laser polarization direction (i.e. P-polarized case); and fade colors (due to less light absorption) are observed when the polarizer is aligned perpendicular to the laser polarization direction (i.e. S-polarized case). The right panel of Fig. 4.4 shows two polarized photos of the double signets of the Martin-Luther-University: one of them was irradiated by horizontal-polarized pulses and the other one was irradiated by vertical-polarized pulses. When viewed under the polarizer, the contrast of the colors can be identified. A signet can be viewed bright or fade by aligning the polarizer parallel or perpendicular to the corresponding laser polarizations.

Essentially, the optical dichroism induced to the irradiated areas is a macroscopical consequence of the nanoparticle shape modifications. Linearly polarized laser irradiation can transform initially spherical silver nanoparticles into elongated shapes (i.e. prolate spheroids [8]) with their symmetry axes uniformly oriented along the polarization direction of the laser. The electron microscope images of the modified nanoparticles are shown on the left panel of Fig. 4.5. Due to this shape modification, the original surface plasmon resonance of Fig. 4.2 splits into two spectrally separated bands, which are shown on the right panel of Fig. 4.5. The physical background of this band splitting is associated with the electron oscillations parallel (P-polarized) and perpendicular (S-polarized) to the symmetry axis of the

modified nanoparticle. These electron oscillations are schematically represented by the small arrows drawn next to the corresponding plasmon bands.

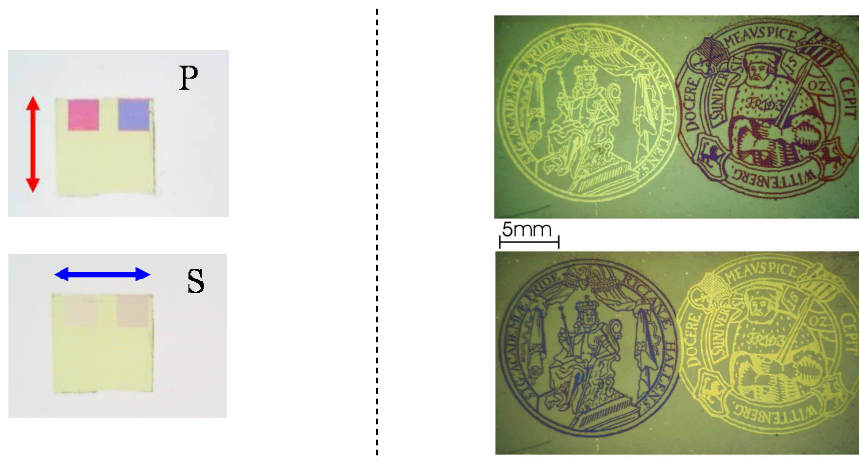


Fig. 4.4. Left panel: The irradiated areas display optical dichroism. The photos were taken using a film polarizer. Bright (fade) colors are observed when the polarizer is aligned parallel (perpendicular) to the laser polarization direction. Right panel: The double signets of the Martin-Luther-University written by laser irradiation on a glass containing silver nanoparticles (from [5]). The laser polarization was rotated 90 degrees before the irradiation of the second signet.

The spectral gap between the surface plasmon resonances of the modified nanoparticle depends strongly on the aspect ratio [9, 10], which is defined as the length of the modified nanoparticle divided by its width (a/c). To see a global picture, Fig. 2.8 can be revisited, which shows the P- and S-polarized extinction spectra of silver nanoparticles with aspect ratios ranging from 1 to 5. Therefore, it becomes also clear that the spectral gap between polarized plasmon bands is directly related to the degree of dichroism induced to the nanoparticle. In this context a sample displaying a high dichroism should have P- and S-polarized bands well separated from each other (i.e. nanoparticles with high aspect ratios). Varying the irradiation parameters, the

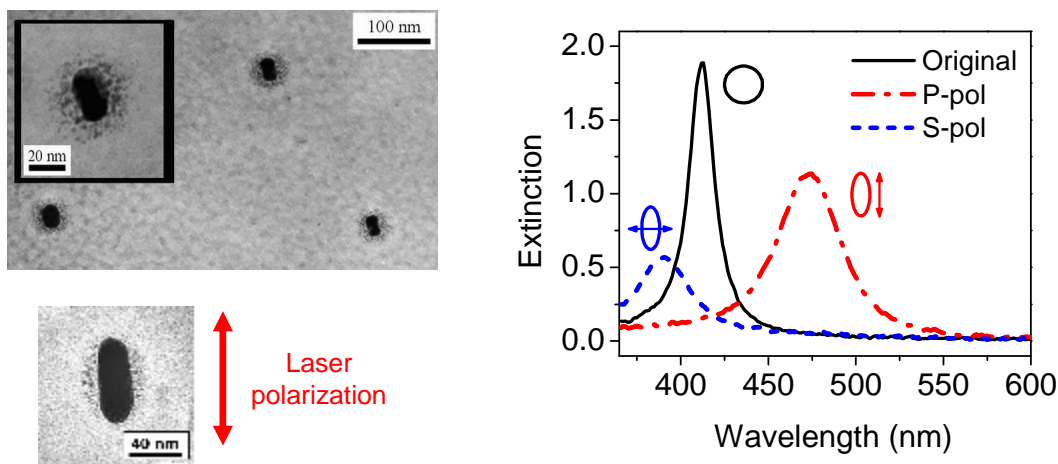


Fig. 4.5. Left panel: TEM images of irradiated nanoparticles (from [5]). The original spherical shapes of the nanoparticles are permanently modified to oblong shapes with laser polarization being parallel to the nanoparticles' longer axes. Right panel: The extinction spectra of the original (spherical) and modified (spheroidal) nanoparticles. P- (S-) polarization band corresponds to the extinction along the long (short) axes of the nanoparticles.

aspect ratios of the nanoparticles can be adjusted to tailor desired optical properties of the nanoparticles. Searching for the best set of parameters that can yield the highest nanoparticle aspect ratios is one of the tasks for development of nanoparticle-based device applications such as filters and polarizers. For this reason, the irradiation parameters are very important. As mentioned above, these parameters include the selection of the wavelength of irradiation, the energy and the number of pulses. In the following, we will briefly describe the effect of different parameters on nanoparticle shape modifications.

The easier way of modifying nanoparticle shapes is with the selection of suitable irradiation wavelengths. Because the spherical silver nanoparticles have their surface plasmon absorption band around 410 nm, the irradiation wavelength should be also in this region. In this sense 400 nm pulses would be the best choice for near-resonant irradiation. Even though laser wavelengths lower than 350 nm are not resonant with nanoparticle surface plasmon modes, they are also absorbed through the interband transitions of silver ($E > 3.5$ eV, see Fig 3.2). Further increasing the laser energy towards to UV region will ionize the embedding glass matrix, which is not desirable at all. The other side of the spectrum contains irradiations with higher wavelengths. Nanoparticle shape modifications have also been realized with green (532 nm) and red laser pulses (800 nm), but they require much higher intensities compared with the resonant 400 nm irradiation.

Following the fundamental effects of laser polarization (see Fig. 4.5) and wavelength on nanoparticle shape modifications, the most prominent laser parameters are surely the laser intensity and the irradiation density (i.e. the number of pulses). These two parameters complete each other in a sense when it comes to nanoparticle elongations. That means, when all other parameters are fixed, nanoparticles of a certain aspect ratio can be produced either by applying `high intensity and less number of pulses` or by applying `low intensity and high number of pulses`. Each pulse helps the nanoparticle grow step by step along the polarization direction in a sort of accumulative manner. The extreme case of a single pulse with very high intensity was also observed to result in a noticeable aspect ratio, which has, however, a symmetry axis perpendicular to the laser polarization [8] (i.e. in the form of oblate spheroids). As a remark for the case of low intensity and high number of pulses, we must state that the peak pulse intensity should be not lower than ~ 0.2 TW/cm², which is the shape modification threshold of silver nanoparticles in glass [11, 12]. Below this intensity level, the changes induced to the nanoparticle are totally reversible (like the weak excitation regime).

In the following, we will concentrate more into the description of femtosecond laser pulses that were used to create the above mentioned nanoparticle shape modifications. As the reproducibility of the experiments depends heavily on the good standards of the laser pulses, we will explain the spatial and temporal characterization of the laser pulses starting from their generation on. We will also briefly describe some of the well-known pulse characterization tools that were used in our experiments.

4.3. Femtosecond laser pulses and pulse characteristics

A commercial Ti:sapphire [13] laser system, which consists of a mode-locked femtosecond oscillator and a regenerative amplifier (both from Spectra Physics), is used as the primary laser source throughout the experiments of this work. The main component of the system is the acousto-optically mode-locked Ti:sapphire oscillator, which generates Gaussian pulses in the infrared region (centered at 800 nm) having pulse widths shorter than 100 fs. A sketch of the laser system is shown in Fig. 4.6. The green lasers on the figure are diode-pumped Nd:YVO₄ and Q-switched ND:YLF pump lasers for the oscillator and the amplifier, respectively.

As the energy of the output pulses from the oscillator is in the region of a few nJ, they are too weak to induce permanent shape modifications on nanoparticles. Therefore these low energy pulses are amplified to high energy levels (~ 0.5 mJ) by the regenerative amplifier. The working principle of the amplifier is based on chirped pulse amplification, which is a method of generating very short pulses at high powers. The regenerative amplifier consists of three parts: namely the stretcher, the amplifier and the compressor. First of all, the seed pulses from the oscillator are stretched in time to ensure a safe amplification process. If not stretched, a femtosecond pulse can cause catastrophic damages with very high peak powers during the amplification. A single stretched pulse is allowed from the stretcher part to the amplifier cavity with the help of an electro-optic modulator (Pockel cell). This pulse makes tens of passes through a Ti:sapphire rod, which is pumped by the mentioned Q-switched laser. Extracting much of the energy from the rod, a second Pockel cell sends the pulse out of the cavity. The stretched and amplified pulse is then temporally recompressed back to its original duration of ~ 100 fs with a grating compressor unit. At the end, the strong output pulses of the amplifier are almost transform-limited in time with a high beam quality.

The real electric field of an ultrashort laser pulse (e.g. the pulse shown in Fig. 4.6) can be given as

$$E(t) = \text{Re}\{\sqrt{I(t)} \exp[i(\omega_0(t) - \phi(t))]\} \quad (4.1)$$

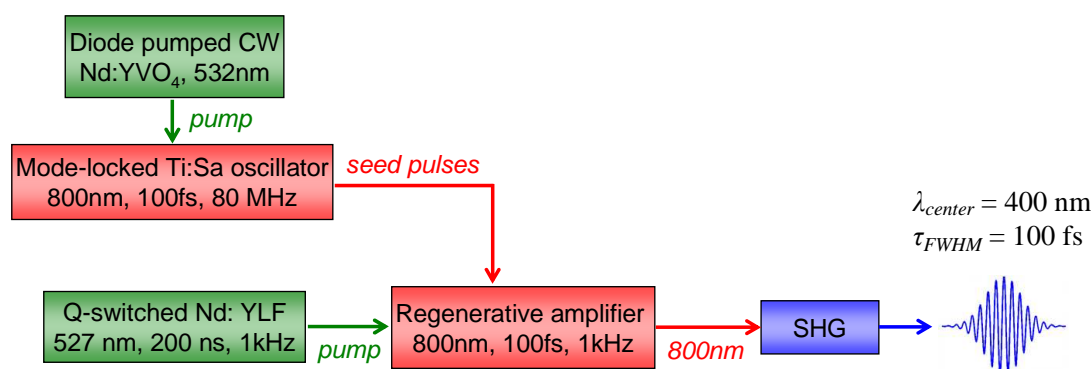


Fig. 4.6. Schematic of the Spectra Physics femtosecond laser system. Low energy pulses (~ 4 nJ) from the oscillator are amplified by the regenerative amplifier to 0.5 mJ of energy in 100 fs. The central wavelength of the fundamental 800 nm beam is frequency-doubled to generate the second harmonic at 400 nm with ~ 100 μ J of energy.

where I is the intensity, ω_0 is the angular frequency and $\varphi(t)$ is the phase of the pulse. A good approximation for any ultrashort pulse is the Gaussian pulse with zero phase. The amplitude and the intensity of a theoretical Gaussian pulse can be written as follows

$$E(t) = E_0 \exp[-2 \ln 2 (t / \tau_{FWHM})^2] \quad (4.2)$$

$$I(t) = |E_0|^2 \exp[-4 \ln 2 (t / \tau_{FWHM})^2] \quad (4.3)$$

where τ_{FWHM} is the pulse duration measured from intensity full-width at half-maximum. Figure 4.7 shows the real electric field, amplitude and intensity of this Gaussian pulse. The intensity is $\sqrt{2}$ shorter than the real amplitude in time. As the plotted pulse is transform-limited, its time-bandwidth product ($TBP = \Delta t \cdot \Delta \nu$) is at its theoretical minimum, which is 0.441 for Gaussian pulses.

The high energy infrared pulses (centered at $\lambda = 800$ nm with $\Delta\lambda \sim 20$ nm) are frequency-doubled to $\lambda = 400$ nm with a 0.5 mm thick Type-I Beta Barium Borate (BBO) crystal. Normally the second harmonic generation (SHG) intensity depends on the l^2 of the crystal but for short pulses (having large bandwidths) there will be a narrow phase-matching bandwidth for thick crystals. Therefore the thickness (i.e. length) of the crystal is determined by taking into account the group velocity mismatch (GVM, i.e., temporal walkoff) of the fundamental and the generated beams in the crystal. The group velocities of the pump (800 nm) and the SHG (400 nm) in BBO are $0.593251c$ and $0.574089c$, respectively, which correspond to a GVM ($1/v_{pump} - 1/v_{SHG}$) of 187 fs/mm. Considering that the pump has a temporal bandwidth of 100 fs, the length of the crystal can be found to be around 0.5 mm through $l = \tau_{pump} / GVM$. The efficiency of the SHG process is about 25 %, resulting in 100 μ J of maximum pulse energy, which is more than enough for our purposes. Longer crystals would definitely result in higher SHG conversion efficiencies but at the expense of causing severe distortions to the temporal shape and the duration of the harmonic pulses.

The polarization direction of the SHG beam is perpendicular to the polarization direction of the fundamental beam as a result of the Type-I phase matching in the nonlinear crystal. The vertically-polarized (i.e. linear-polarized)

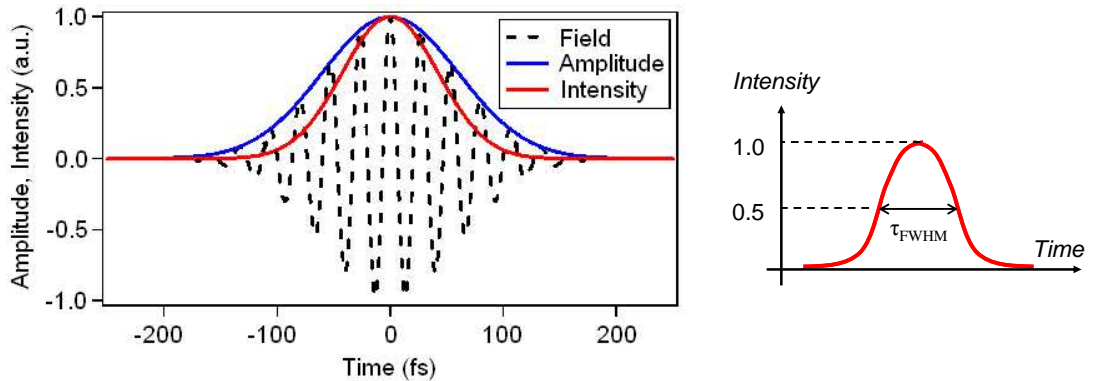


Fig. 4.7. Left panel: The real electric field, amplitude and intensity of a 100 fs Gaussian pulse. Right panel: The definition of the τ_{FWHM} as the pulse width.

SHG beam is characterized spatially and temporally before sending to the experimental setups. For the sake of reproducibility and reliability of the experimental results, the characteristics of the laser pulses should be measured regularly to have the same universal standards. Namely these standards are set with the theoretical description of the fs laser pulses regarding their spatial and temporal shapes. In this sense it is not enough to have a circular beam pattern; rather it should have a fundamental TEM₀₀ Gaussian intensity profile with a plane wavefront. The spatial profile should also look like the profile shown on the right panel of Fig. 4.7 - only in the spatial domain. In the same way, it is not enough to have just a short (e.g. 100 fs) pulse width, rather it should have a Gaussian temporal profile (as in Fig. 4.7). For these reasons, the spatial and temporal characteristics of the pulses should be maintained before proceeding with the experiments.

Figure 4.8 shows the two-dimensional spatial profile of the SHG beam. The beam is focused by a 150 mm lens, and the image is recorded by a CCD camera before the focus of the lens perpendicular to the propagation direction of the beam. The intensity distribution is best-fitted with the Gaussian function. It is clearly seen that the beam has a Gaussian profile with the fundamental TEM₀₀ mode. The diameter (beam width) of the Gaussian shape is defined at the position where the beam irradiance (intensity) has fallen to $1/e^2$ (13.5 %) of its peak value. Having the fundamental mode of the beam before focusing is very important in this sense, because at each focusing depth, the beam will retain its Gaussian character.

The intensity distribution of the Gaussian TEM₀₀ beam can be given as

$$I(r) = I_0 \exp(-2r^2 / \omega_0^2) = \frac{2P}{\pi\omega_0^2} \exp(-2r^2 / \omega_0^2) \quad (4.4)$$

where I_0 is the peak intensity, r is the distance from the beam center and ω_0 is the spot size (width) of the laser beam (right panel of Fig. 4.8). The peak intensity of the Gaussian beam is defined as: $2P/\pi\omega_0^2$, where P is the laser pulse power or output power. The geometry and behavior of a Gaussian beam are described by a set of beam parameters (such as the M^2 quality factor, beam width ω_0 , the Rayleigh range, etc.), the detailed definitions of which can be found elsewhere [14].

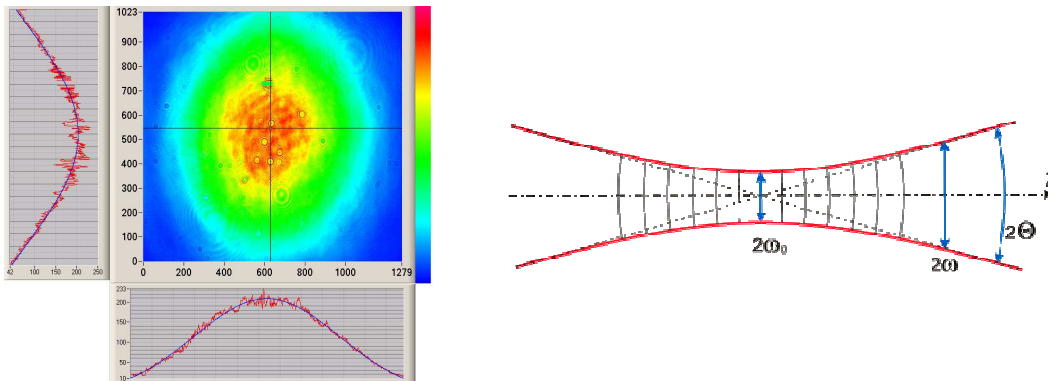


Fig. 4.8. Left panel: Two-dimensional spatial beam profile of the SHG beam showing the TEM₀₀ Gaussian mode. Right panel: The free space propagation of the Gaussian beam with a beam waist (spot size) of ω_0 . The growth in ω_0 (i.e. divergence) with the propagation distance is observed.

The minimum focal spot size that can be achieved with a 150 mm focal length lens is measured to be $\sim 30 \mu\text{m}$. This sharp focus was used only for single shot experiments, which necessitate very high intensities. On the other hand, the majority of the experiments employed a beam diameter of about $100 \mu\text{m}$ by placing the sample before the focus.

After this introduction of the spatial characteristics of the laser beam, now we will continue with the temporal characteristics of the laser beam comprising ultrashort pulses. Temporal characterization of ultrashort laser pulses with pulse widths greater than 20 ps can be directly performed electronically using high speed photo detectors. For shorter pulses, however, there is no means of direct measurement possibilities. Therefore, one needs to employ some type of correlation techniques in the optical domain using the instantaneously responding nonlinear-optical medium. As there are no other controllable events faster than the ultrashort pulses, the idea is to use the pulse itself to measure its temporal width, which is called as the autocorrelation. It involves splitting the pulse into two, delaying one with respect to the other, focusing and spatially overlapping both of them in a SHG crystal in a non-collinear fashion to generate second harmonics. The setup for this process is sketched in Fig. 4.9. The intensity of the generated signal light $I_{sig}(t, \tau)$ is measured by varying the delay; therefore it is directly proportional to the amount of overlapping of the two pulses and can be written as

$$I_{sig}^{SHG}(t, \tau) \propto I(t)I(t - \tau) \quad (4.5)$$

Because the detector is too slow to resolve this beam in time, it simply integrates the signal as

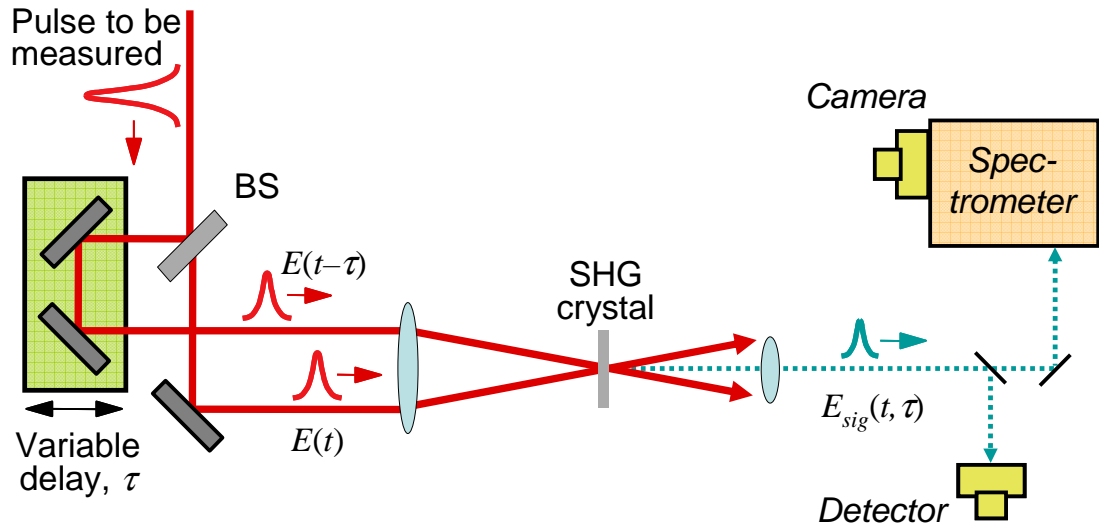


Fig. 4.9. Setups for an intensity autocorrelator (employing the detector) with second harmonic generation and a SHG-FROG (employing the spectrometer with camera). All optical instruments are reflective with very less dispersion. The beam splitter (BS) with a thickness of 0.2 mm and the focusing lens are the only dispersive components. Pulses as short as 30 fs can be measured. $E(t)$ is the probe pulse and $E(t-\tau)$ is the gate pulse. Signal pulse $E_{sig}(t-\tau)$ generated from the SHG crystal is measured to extract the input pulse duration. The schematic is adapted from [15].

$$A(\tau) = \int_{-\infty}^{\infty} I(t)I(t-\tau)dt \quad (4.6)$$

which is the intensity autocorrelation [16]. It contains only the intensity information of the input pulses and says nothing about the electric field of the pulse. Therefore, the phase of the pulse is completely lost.

To overcome this problem and to achieve the time-domain phase information of the pulses, another technique must be used, which is called as the frequency-resolved optical gating (FROG) [17, 18]. In general there are four different techniques of performing FROG: Second Harmonic Generation (SHG) [19], Third Harmonic Generation (THG), Polarization Gate (PG), and Self Diffraction (SD) [20]. The schematic of Fig. 4.9 shows only the SHG-FROG. This technique employs the similar optical setup like the intensity autocorrelator of Fig. 4.9, the only difference

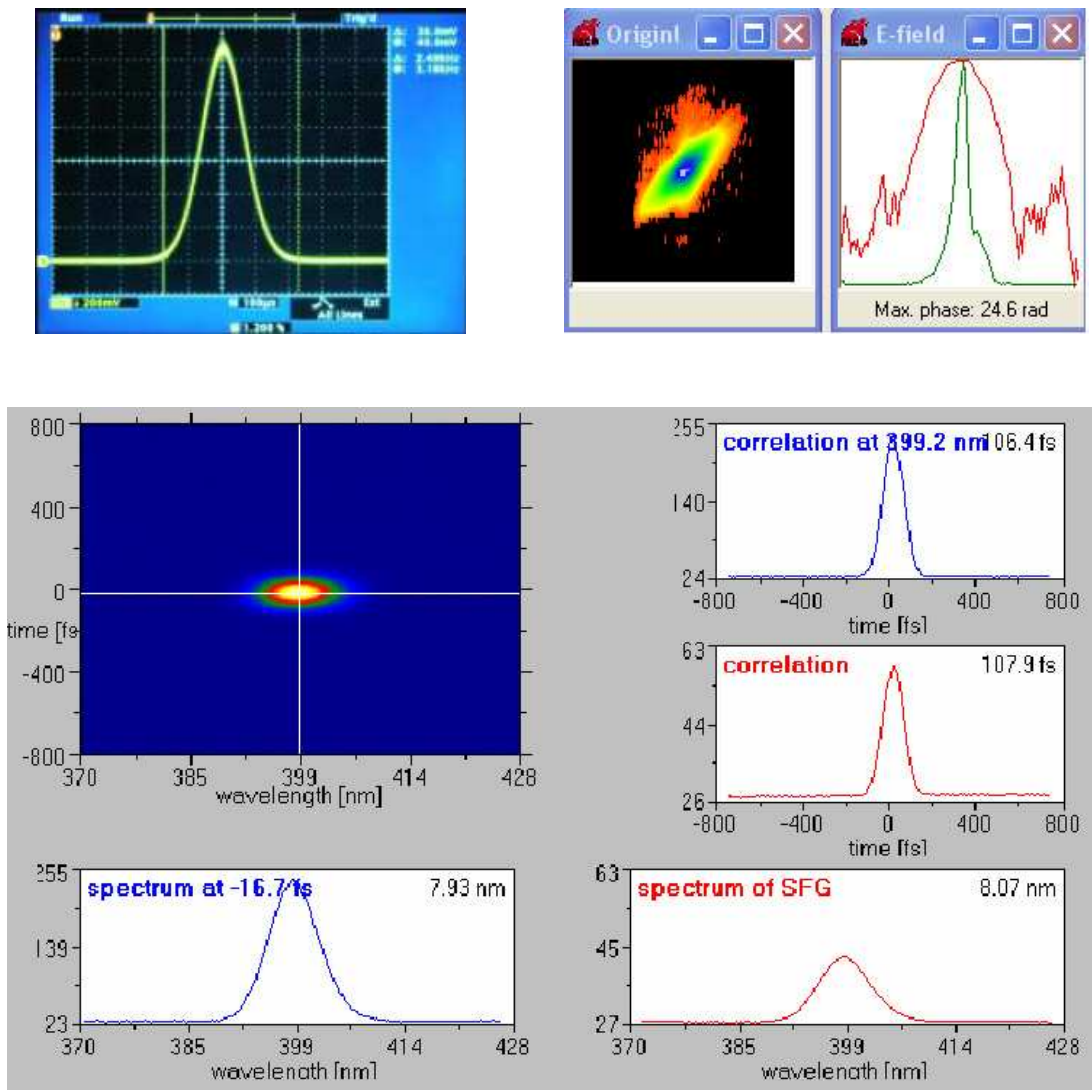


Fig. 4.10. Temporal beam profiles of ultrashort pulses with different techniques. Top left panel: Autocorrelation trace of a ~ 100 fs laser pulse at 800 nm. Top right panel: SD-FROG trace of a laser pulse at 400 nm, yielding 90 - 100 fs of pulse width. Bottom panel: SHG-FROG trace, showing ~ 108 fs of pulse width together with the spectral information.

is that the detector is replaced by a spectrometer. Instead of measuring the autocorrelator signal intensity vs. delay, FROG involves measuring the signal spectrum vs. delay. Therefore, it measures additionally a frequency spectrum at each time delay and can be used to reconstruct the temporal and spectral phase with an iterative, retrieval algorithm developed by Rich Trebino [16]. This provides a bunch of additional information about the spectral components. The resulting frequency-resolved intensity FROG-trace, or spectrogram (I_{FROG}^{SHG}) can be given as

$$I_{FROG}^{SHG}(\omega, \tau) = \left| \int_{-\infty}^{\infty} E(t) |E(t - \tau)|^2 \exp(-i\omega t) dt \right|^2 \quad (4.7)$$

As an example, Fig. 4.10 shows the results of different pulse characterization techniques. The top left panel shows the intensity autocorrelation of a ~ 100 fs pulse at 800 nm. The same pulses can be measured with a SHG-FROG with more details, which is seen in the bottom panel. The FROG-trace displays the hybrid time-wavelength domain view of the laser pulse. As the pulse is unchirped the spectrogram is linear without any slope. This method is one of the most reliable methods of pulse characterization because it directly displays the chirp of the pulses.

The panel on the top right is a view from the SD-FROG measurements of the second harmonic pulses at 400 nm. Often it is not trivial to measure the widths of 400 nm pulses with the above mentioned autocorrelation and SHG-FROG methods, because the signal beam to be produced from the nonlinear crystal will be in the UV region (200 nm) and the UV sensitive optics (the nonlinear crystal that has phase matching for this wavelength, the photodiode, and the spectrometer) are usually very expensive. SD-FROG, on the other hand, can provide the means for measurement of the 400 nm input pulses by non-collinearly overlapping them in a thin sapphire plate. The first pulse initiates a sort of diffraction grating in the crystal, which diffracts the time delayed second arriving pulse. The received diffraction signal is then analyzed by the mentioned phase-retrieval algorithm to create the SD-FROG traces.

4.4. Time and polarization-resolved pulse pair irradiation

To investigate the laser-induced shape modification dynamics (including for example the ionization, dissolution, and elongation) of metal nanoparticles, we employ an irradiation technique that generates time-delayed pulse-pairs. The experimental setup creating the time-delayed pulse pairs is shown in Fig. 4.11. The input pulse is divided by a beam splitter into two pulses of equal energy, where one pulse is delayed with respect to the other by the help of a motorized delay stage. The stage can be moved 150 mm away from its original position with 10 μm steps, thereby generating a time delay Δt of up to 1 ns between the pulse pairs. As a result, pulse pairs can be created with a variable Δt in between. The pairs of pulses are focused on the sample to a spot size of about 100 μm , resulting in an energy density of 20 mJ/cm^2 per pulse (in the case of having $E = 3 \mu\text{J}$ per pulse). Moving the sample continuously on a motorized X-Y translation stage, a separate area is irradiated (written) for each desired delay between pulse pairs. Each irradiated area is denoted with the specific Δt of pulse pairs that were used for its irradiation.

As the effect of one pulse (above the shape modification threshold) on the nanoparticle can not be detected spectroscopically, the sample movement is arranged such that on average 300 pulse pairs hit one spot. The time delay between pulse pairs is always 1 ms, the period of the laser system, which is a very long time scale for the irradiated nanoparticle system to relax and establish a steady state again. The experimental results to be shown prove that most of the nanoparticle shape modification events take place within the first 1 ns after the pulse interaction, which is 6 orders of magnitude shorter than 1 ms. So that the pulse pair(s) hitting the nanoparticle after the first pulse pair see a totally relaxed but slightly modified nanoparticle. There are no processes remaining on the nanoparticle from the previous pulses when the forthcoming pulse pairs interact with it. In this sense the high number of pulses applied to the nanoparticle can be thought to ripen the nanoparticle for spectroscopic analysis.

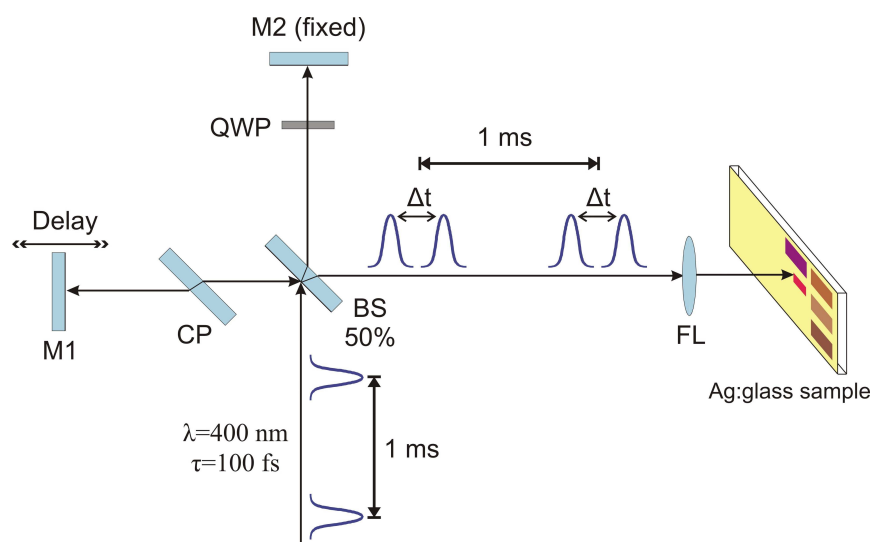


Fig. 4.11. Experimental setup for pulse-pair irradiation. BS: 50 % beam splitter; M1 and M2: 0 degree high reflecting mirrors; CP: compensator plate; FL: focusing lens; QWP: quarter waveplate. M1 sits on a motorized delay stage, which can be delayed up to $\Delta t = 1 \text{ ns}$. The polarization state of the pulse travelling along the M2 arm can be rotated by 90 degrees when the QWP is mounted.

In standard configuration, the polarization of the pulse pair is linear, the polarization planes being parallel to each other. By inserting a quarter-wave plate in one arm of the setup, the pulse in this arm experiences a rotation of the plane of polarization by 90 degrees. In this configuration, the linearly-polarized input light passes two times over the quarter waveplate. As it passes for the first time, the light becomes circularly polarized in a right-handed way, which is then reflected by the end mirror (M2) and becomes left-handed. The left circularly-polarized light passing over the quarter waveplate becomes linearly-polarized again, but with 90 degrees of rotation from its initial state. At the end, this configuration generates linearly-polarized pulse pairs with polarization planes orthogonal with respect to each other.

After the pulse-pair irradiations, the samples were annealed for one hour at $200 \text{ }^\circ\text{C}$ in order to remove any possible laser-induced defects in the glass matrix [21, 22]. Then the polarization-dependent extinction bands from each irradiated area (representing a single time delay Δt) are recorded by conventional transmission

spectroscopy (Schimadzu 3100 UV/VIS/NIR spectrometer). These bands are then analyzed by the method of moments [23], the details of which will be given in the next chapter (Ch. 5.1).

4.5. Temperature dependent irradiation

In addition to the laser-related parameters, the nanoparticle shape modification is also found to depend on the initial temperature conditions of the surrounding glass matrix. Following the absorption of the laser pulse energy the nanoparticle lattice gets heated through electron-phonon couplings (see Ch. 3.2) within a short time and it starts to heat up the surrounding glass matrix gradually. In this sense, the softening of the glass matrix around the nanoparticle is crucial for the nanoparticle to have some degrees of freedom for the necessary shape changes. Therefore, pre-heating or cooling of the glass matrix can change the nanoparticle shape modification mechanisms severely. Regarding this fact, the influence of the embedding medium temperature on the laser-induced shape modification of silver nanoparticles should also be investigated.

A simple setup comprising of a heating/cooling chamber was employed for this purpose. The sample was placed in the vacuum chamber with a heat-sink that can be either heated by applying electrical voltage or cooled by using liquid nitrogen. The temperature was controlled by the thermocouple connected to the heat-sink and could be varied from -100 till 170 °C. The chamber windows (thin UV fused silica glasses) transmit the 400 nm laser light with very less dispersion to the pulses.

Chapter

5. Results and discussion

In this chapter basic experimental results regarding the shape modification dynamics of glass-embedded silver nanoparticles and the corresponding discussion points will be presented. The results on nanoparticle shape modification mechanisms will be described in the temporal order of their occurrence (i.e. starting from the fastest and going to the slowest). In this context, our roadmap will be roughly like the one in Chapter 3, where the theoretical descriptions of physical events upon laser interaction with the nanoparticle were presented in their temporal sequence.

First of all, we will start with a brief introduction of the influence of time delay between the irradiating pulses on nanoparticle shapes. As an addition to the laser parameters that were described in the last chapter (see Ch. 4.2), we will show that the time delay between the irradiating pulses has also very important consequences considering the aspect ratios of the modified nanoparticles. Afterwards, we will present the time-resolved results of parallel and orthogonal-polarized pulse pair irradiation experiments for the temporal scale of up to 1 ns. Essentially it is possible to identify three time intervals out of these results. The dynamics observed within the first 20 ps indicate that this is the time scale for the fastest processes like ionization of the nanoparticle and the forthcoming Coulomb explosion. For the detailed investigation of these mechanisms, we will employ the extended two-temperature model (see Chapter 3.2.2) in conjunction with the electronic band structure of the composite glass. Therefore, the results indicating the ionization and the dissolution of the nanoparticle will be modeled in the frame of directed and isotropic electron emissions. The second time interval contains the intermediate dynamics observed from 20 to 100 ps of time delay. The experimental observations of this interval suggest that the glass surrounding the nanoparticle becomes hot enough to support the mobility of the emitted silver ions, which can be reduced by the trapped electrons in the following times. Further increasing of the surrounding temperature, for example by heating the glass externally, may estrange the emitted ions from the main nanoparticle, resulting in a smaller particle at the end. Finally, the long-term dynamics that range from 100 ps to 1 ns are associated with the reduction and the clustering of the emitted ions together with the start of their recombination with the main nanoparticle. These processes provide the origin of the nanoparticle shape elongations.

5.1. Influence of time delay on nanoparticle shapes – an introduction

As described in Chapter 4.2 the original surface plasmon (SP) band of the spherical silver nanoparticles is split into two polarization-dependent bands (Fig. 4.5) upon irradiation with a number of parallel-polarized pulses. The spectral gap between the polarized SP bands is proportional to the aspect ratio of the modified nanoparticle. This is observed as the optical dichroism, which is essentially the macroscopic consequence of the permanent shape elongation of the nanoparticles. In this context, various irradiation parameters (such as the wavelength, polarization, and the intensity of the laser, together with the irradiation density, etc.) that can influence the final nanoparticle shapes were described.

Besides these parameters, the effect of laser pulse widths on permanent nanoparticle shape changes has been a question mark for a long time. Although, some experiments [1] with pulse durations as long as 4 ps reported nanoparticle shape modifications, the efficiency of even longer pulses is not well known [2]. Our main aim is not the investigation of this specific issue; nevertheless our results of pulse pair irradiation experiments suggest an answer. In the following, we will present the results on nanoparticle shape modification dynamics, which testify that the time delay Δt between the pulses of each irradiating pulse pair has a great influence on nanoparticle aspect ratios. For example, irradiation of nanoparticles with pulse pairs very close to each other in time results in very high dichroism, while the dichroism is sharply reduced when the pulses are separated. Therefore the time delay between pulses, which can be considered to be an effective pulse width ($\Delta t \approx \tau$), should also be listed as one of the nanoparticle shape determining parameters.

The strong influence of time delay between two pulses of each pair on nanoparticle shapes opens up the possibility of several experiments, which employ the idea of scanning a whole range of time delay (delaying a pulse with respect to the other) to investigate the nanoparticle shape modification dynamics. The results in the following exploit this simple idea, which is realized with different set of controlled experiments (i.e. varying pulse energies and polarizations) to account for the physical mechanisms triggering the laser-induced nanoparticle shape changes. As a technical point, we must state that in order to create the same irradiation conditions, the total number of pulses hitting a sample area are kept constant for all type of experiments. Additionally the irradiated focal spot sizes on the sample are also kept the same for all experiments. Therefore, the results are directly comparable with each other. As an illustration to the effect of Δt on nanoparticle aspect ratios, we will present some of the results from two sets of experiments in the following: the first one employing parallel-polarized pulses and the other one with orthogonal-polarized pulses.

A series of areas were irradiated on the sample by varying the delay between two parallel-polarized pulse pairs, where a separate area corresponds to a desired Δt between pulse pairs. Figure 5.1 depicts the measured polarized spectra for several time delays, showing the temporal evolution of the modified plasmon extinction bands when irradiated by pulses of varying delay. Figure 5.1(a) shows the spectra from an area, which was irradiated by the usual successive pulses from the laser without any generation of pulse pairs. As the period of the laser is 1 ms, the pulses

follow each other in time with a natural delay of $\Delta t = 1$ ms. As it was stated in the description part of the experimental setup (Ch. 4.4), 'P-pol' ('S-pol') abbreviate the polarization of light parallel (orthogonal) to the polarization of the second pulse of each pair interacting with the sample. As we have only vertical polarized pulse pairs here, P-pol always denotes the direction of nanoparticles' long axes parallel to the laser polarization. Figure 5.1(a) clearly shows that the S- and P-polarized surface plasmon extinction bands are well separated from each other, where the P-polarized band center lies around 475 nm while the S-polarized band center lies in the near UV region, ~ 390 nm. The central peak position of the P-polarized band is marked with a dashed vertical line as a guide to the eye for comparison with the forthcoming results. The dashed vertical line in Figs. 5.1(d-f) marks also at the same spectral position.

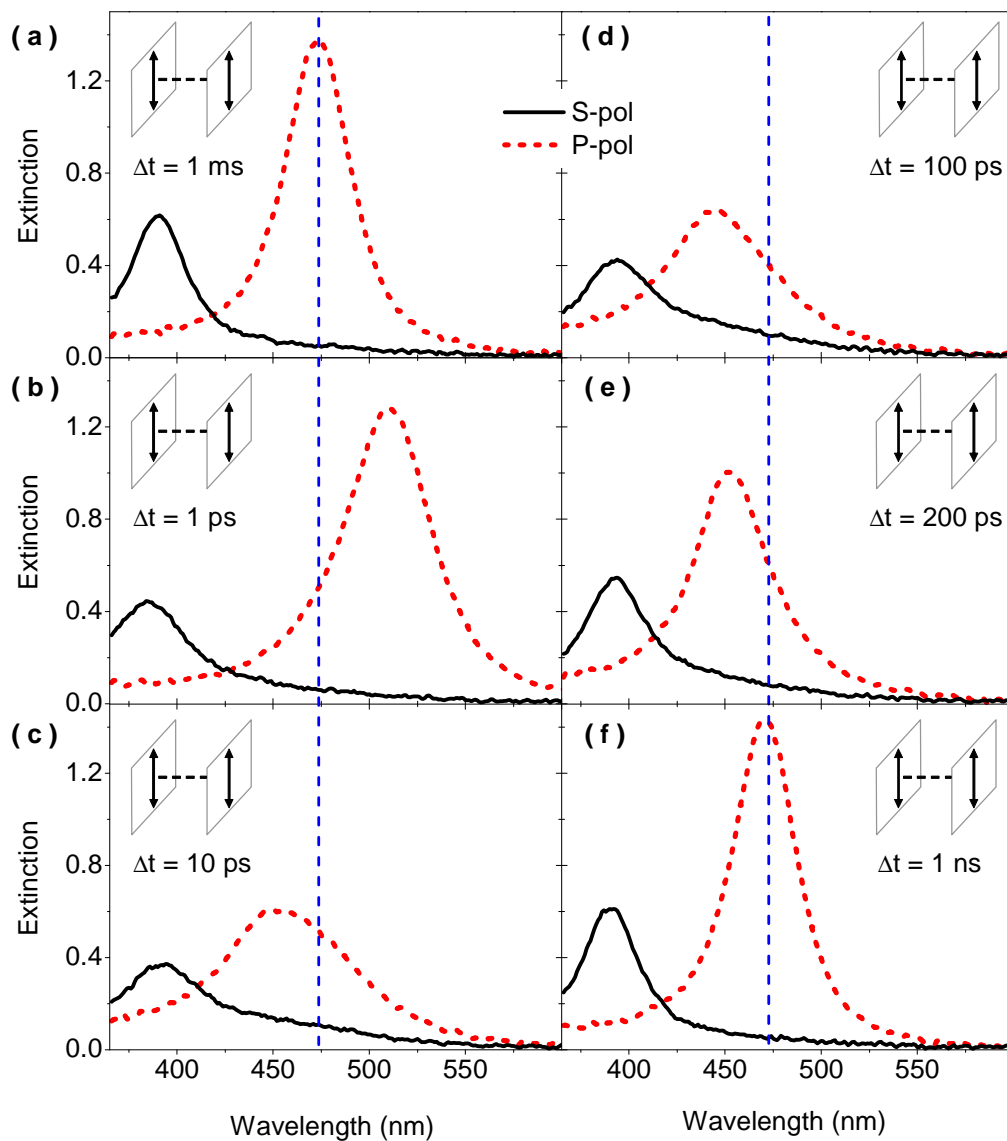


Fig. 5.1. Surface plasmon extinction bands of nanoparticles resulting from parallel-polarized pulse-pair irradiation experiments for different time delays: $\Delta t = 1$ ms (a), 1 ps (b), 10 ps (c), 100 ps (d), 200 ps (e), 1 ns (f). The energy of each pulse is $3 \mu\text{J}$ (fluence of $\approx 20 \text{ mJ}/\text{cm}^2$ at the sample spot). Arrows represent the polarization directions of the pulses. The dashed vertical lines are guides to the eye, marking the central peak position of the P-polarized band of $\Delta t = 1$ ms irradiation for comparison.

When the pulses are brought very close to each other in time (e.g. $\Delta t = 1$ ps or shorter) by employing the experimental setup described in Ch. 4.4, the resulting P-polarized band is observed to shift to longer wavelengths with the central peak position at 510 nm, which is shown in Fig. 5.1(b). The spectral position of the S-polarized band is almost the same with the $\Delta t = 1$ ms irradiation. Considering the aspect ratios of the modified nanoparticles for the 1 ms and 1 ps irradiation cases, it is apparent that the irradiation with pulse pairs of 1 ps delay results in a higher spectral gap, thereby higher aspect ratios for the nanoparticles. That means, it is better for the end result of irradiation (considering the nanoparticle aspect ratios) to have a pair of pulses close to each other in time rather than separated pulses. This is an important observation, because it suggests some very fast physical mechanisms that take place within the first picoseconds of laser irradiation. Whatever these mechanisms are, it is clear from the spectra that they are enhanced with the second pulse arriving the disturbed nanoparticle shortly after the first pulse. The lifetime of these mechanisms can be found varying the delay further to see the spectra for longer time delays.

The observations show that increasing the delay between two pulses of each pair ($\Delta t > 1$ ps) causes a decrease in the central positions of the P-polarized plasmon bands. After passing over a specific time delay, the P-polarized band crosses the central position of the 1 ms irradiation (the dashed vertical line) and goes further towards the blue side of the spectrum. As an example to this case, the results of $\Delta t = 10$ ps irradiation are depicted in Fig. 5.1(c). The P-band is observed to occur around 450 nm, well below the dashed vertical line. This result is also of very high importance, as it suggests that the existence of the second pulse, which hits the already disturbed nanoparticle 10 ps after the first one, is worse off for the shape modification (i.e. the spectral gap) of the nanoparticles, compared with the 1 ms irradiation. It is understood from this simple result that some fast mechanisms should have happened until 10 ps, so that the nanoparticle irradiated with a second pulse during or after these mechanisms result in a less aspect ratio. Additionally, a decrease in band amplitude and an increase in bandwidth accompany the observed shift of the surface plasmon bands.

The spectra presented in Fig. 5.1 (d-f) are obtained from irradiations with long time delays between pulse pairs. For illustrative reasons three experiments with time delays of $\Delta t = 100$ ps, 200 ps and 1 ns are depicted in the figure. First to notice is again the shifts of the P-polarized band centers with the increasing time delay. The P-band of the 100 ps irradiation lies almost at the same region with the one of the 10 ps. Increasing the time delay to 200 ps causes the band to shift towards the P-polarized band of the 1 ms irradiation. The maximum time delay of 1 ns (10^{-9} s) results in a pretty interesting result, which produces both S- and P-polarized bands almost at the same spectral position with the ones of the 1 ms (10^{-3} s) irradiation. Not only the positions of the 1 ns and 1 ms bands but also the bandwidths and band amplitudes are very similar to each other. This indicates that although there are much slower energy relaxation mechanisms, most of the shape determining parameters are completed within the first 1 ns. As most of the events started by the first pulse have already finished until 1 ns, the second pulse hitting the nanoparticle after this time can not influence those events in a positive or a negative manner. Rather than that the second pulse triggers new mechanisms from the beginning, but on a slightly non-spherical nanoparticle. As we use several hundred pulse pairs (Ch. 4.4) for

observable nanoparticle shape changes, the forthcoming pulses with $\Delta t \geq 1$ ns will only have an additive (cumulative) role in reshaping the nanoparticle.

For a complete discussion of the possible nanoparticle shape modification dynamics, the full temporal evolution of the plasmon bands (from perfect overlapping of pulses until $\Delta t = 1$ ns) will be presented in the following section. Before proceeding with that, we now like to introduce the influence of relative polarizations of pulse pairs on the nanoparticle aspect ratios when they are orthogonal to each other during the time-delayed irradiation experiments. While keeping the first pulse's polarization as vertical, the polarization of the second pulse is rotated by 90 degrees (resulting in a horizontal-polarized pulse) as described in the experimental section. This is a useful control experiment, the results of which can be compared with the parallel-polarized experiments for a better understanding of directional mechanisms induced to the nanoparticle.

Figure 5.2 presents some of the short-term results of the orthogonally polarized pulse pair experiments. Figure 5.2(a) depicts the irradiation case when the pulses overlap in time ($\Delta t = 0$), which results in a very interesting situation. The temporally overlapping pulses lead to a considerable red-shift of the surface plasmon band centers with respect to the original surface plasmon band (at 413 nm, see Fig. 4.2), but without any directional preference (i.e. no dichroism). This is indeed the

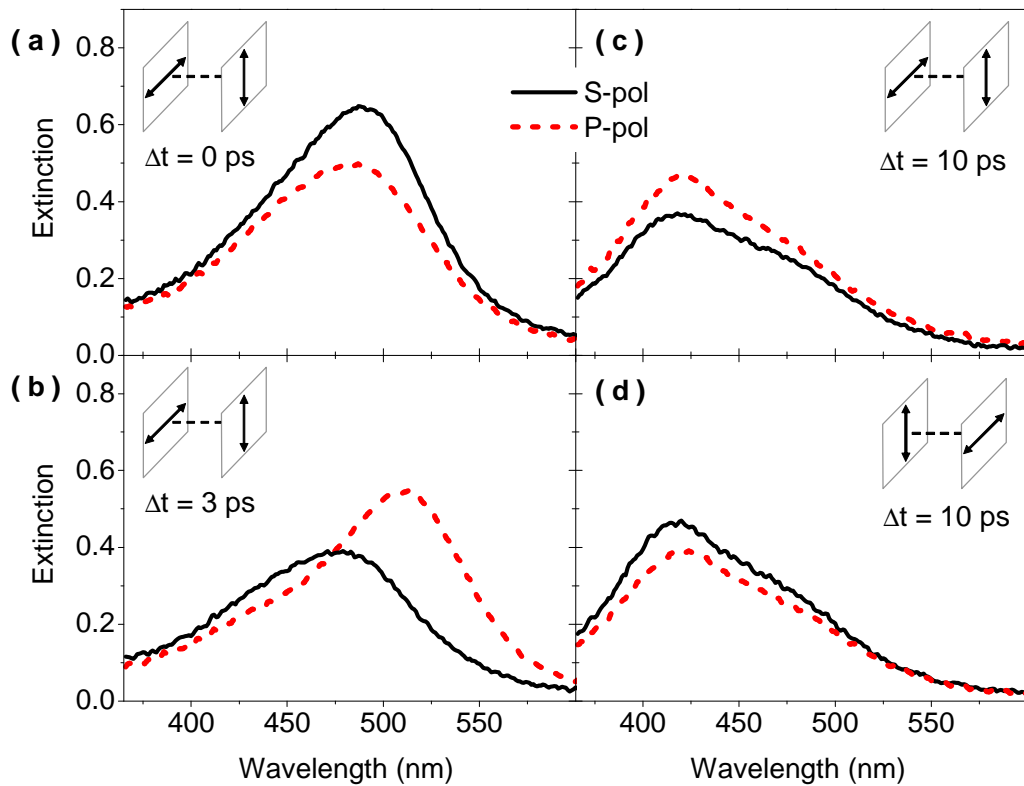


Fig. 5.2. Surface plasmon extinction bands of nanoparticles resulting from orthogonal-polarized pulse pair irradiation experiments for different time delays: $\Delta t = 0$ ps (a), 3 ps (b) and 10 ps (c-d). The order of the pulses is changed from (c) to (d). The energy of each pulse is $3 \mu\text{J}$ (fluence of $\approx 20 \text{ mJ/cm}^2$ at the sample spot). Arrows represent the polarization directions of the pulses.

same behavior as was obtained by irradiation of the nanoparticles with circularly polarized pulses, which created a red-shift of the surface plasmon band, but no dichroism within experimental accuracy [3].

However, as the pulses are separated from each other, for example the time delay of $\Delta t = 3$ ps is shown in Fig. 5.2(b), the dichroism with a considerable spectral gap occurs. Strikingly here, the stronger red-shifted surface plasmon band (the P-pol) is found to be along the direction of the polarization parallel to that of the second-hitting pulse. That means that also the nanoparticles' long axes are being defined by the pulse interacting with the sample later in time. This statement, however, is only true for a limited range of time delay. Figure 5.2(c) shows the situation for $\Delta t = 10$ ps, where the centers of both S- and P-bands experience only a small red-shift (with respect to the original band of spherical nanoparticles) upon irradiation, and the dichroism vanishes again (spectral gap ≈ 0 nm). Interchanging the order of the pulses (i.e. the horizontal-polarized pulse hits the nanoparticle first) shows no difference (see Fig. 5.2(d)). That means no dichroism can be induced to the nanoparticles when the orthogonal-polarized pulses are separated by $\Delta t = 10$ ps from each other in time. The long-term dynamics of this type of irradiation will be presented in the following section together with the results of parallel-polarized experiments.

As the number of plasmon bands to be considered increases with the increasing range of time delay, it becomes very difficult to compare the resulting bands of a time delay with the others. Therefore a compact analysis of a bundle of spectral bands requires a global method of band analysis. To do this we employ the well-known method of moments [4], which is a statistical method allowing an equal treatment and objective comparison of the spectral parameters of bands possible. The method defines the set of spectral moments as

$$M_i = (1/S_0) \int_{band} (v - \bar{v})^i \rho(v) dv \quad (5.1)$$

$$S_i = \int_{band} v^i \rho(v) dv \quad (5.2)$$

where $\rho = I(v)/v$, and $\bar{v} = S_1/S_0$. The first moment of the normalized photon distribution S_1/S_0 strictly defines the mean wavenumber of the photons \bar{v} . The second central moment is associated with the bandwidth of the spectral curve $\sigma = \sqrt{M_2}$. The third and fourth moments define the tapering and pointedness of the band and thereby characterize its shape.

The integrals of the plasmon extinction bands are also important features for the understanding of nanoparticle shape transformations, as they contain information regarding band amplitudes and bandwidths at the same time. For clarity and to avoid too many inter-related graphs, we will present only the band integrals instead of bandwidths and band amplitudes. Physically, the temporal changes in band integrals (band areas) can be considered as absorption changes of the nanoparticle system; a decrease in the surface plasmon band integral represents a decrease in total amount of absorption (i.e. extinction) and vice versa. This is also in close correlation with the

size of the nanoparticles, as known from the volume dependence of the extinction cross section (Eq. 2.17).

Therefore in the following sections, instead of showing a crowded group of plasmon extinction bands, we will display the central positions of the bands, the spectral gap between the bands, and the band integrals, all of which are analyzed by the described method.

5.2. Temporal evolution of surface plasmon bands

In this section, we will present the temporal evolution of surface plasmon bands up to a time delay of $\Delta t = 1$ ns for parallel- and orthogonal-polarized pulse pair experiments. Several examples of these bands have already been shown in the last section for some selected time delays. As mentioned above, here we will not present the bands themselves, rather the outcomes of the moments analyses.

For a better understanding of the very fast happening nanoparticle shape modification mechanisms, it is very useful to compare the band centers of the pulse pair irradiations with the band centers of the longest delay irradiation, which is $\Delta t = 1$ ms in our case. This is a quite long time delay for the nanoparticle shape modification dynamics to be accomplished; therefore, we can consider it as the steady state situation (see for example Fig. 5.1). The P-pol and S-pol band centers of the corresponding 1 ms irradiations are plotted with horizontal red and black dashed lines on the figures, respectively. Together with the band centers, the figures also depict the amount of dichroism, which is the spectral gap between S-polarized bands and P-polarized bands. The spectral gap is a practical parameter considering the aspect ratio (a/c) of the modified nanoparticles. It decreases as the aspect ratio gets smaller (and vice versa), making it possible to comment on the shape transformation of nanoparticles.

5.2.1. Parallel-polarized pulse pairs

Three sets of results will be presented for parallel-polarized pulse pair experiments. Each of the experiments employed different energy pulse pairs: namely a low energy pulse pair (2 μJ per pulse), a medium energy pulse pair (3 μJ per pulse) and a high energy pulse pair (6 μJ per pulse). The spectral bands shown in the previous section belong to the experiments, which employed 3 μJ energy per pulse (≈ 20 mJ/cm^2 energy density on the irradiated sample spot). The lowest energy pulses correspond almost to the shape modification threshold of the nanoparticles; it was not possible to induce any observable changes to the samples with laser pulses below this energy level. On the other hand, the irradiations with high energy pulses caused partial destruction of the nanoparticles due to the huge intensity on the focussed spot. The most effective nanoparticle shape modifications (above the threshold and without any destruction) are therefore achieved with the medium energy pulses.

The results of the low energy pulse pair irradiation (Fig. 5.3) show that the S- and P-polarized surface plasmon bands are well-separated from each other, resulting

in a high spectral gap for the very short time delays (especially when $0 < \Delta t < 20$ ps). The high resolution data for these short delays will be presented together with the discussion part in the the following sections. There is no other time delay, for which the spectral gap becomes higher than that of the short time delays. The P-polarized band experiences a monotonous decrease with the increasing time delay, while the changes in the S-polarized bands are localized around 420 nm. Therefore the spectral gap decreases gradually, reaching its steady state to $\Delta t = 1$ ms irradiation. The spectral gap between polarized plasmon bands of $\Delta t = 1$ ms (i.e. the gap between the dashed lines) is only 10 nm, which proves that the low energy pulse pair irradiation is indeed just above the threshold of permanent shape modifications.

The behavior of the spectral gaps show clearly that the irradiation of a second pulse is almost always better off for the nanoparticle aspect ratios if it is no more than 600 ps delayed. After $\Delta t = 600$ ps, the spectral gap is almost equal to that one of the $\Delta t = 1$ ms delay. This observation suggests that for the low energy pulse pair case, the mechanisms determining the nanoparticle shape changes are more or less finished within 600 ps. It is clearly seen that the band centers and the spectral gap of $\Delta t = 1$ ns irradiation is equal to those values of the $\Delta t = 1$ ms case, which means that for the low energy pulse pairs, the nanoparticle shape changes are almost fully finished within 1 ns. This argument is plausible, because the second pulse hitting the nanoparticle 1 ns after the first pulse does not do anything (that we can observe

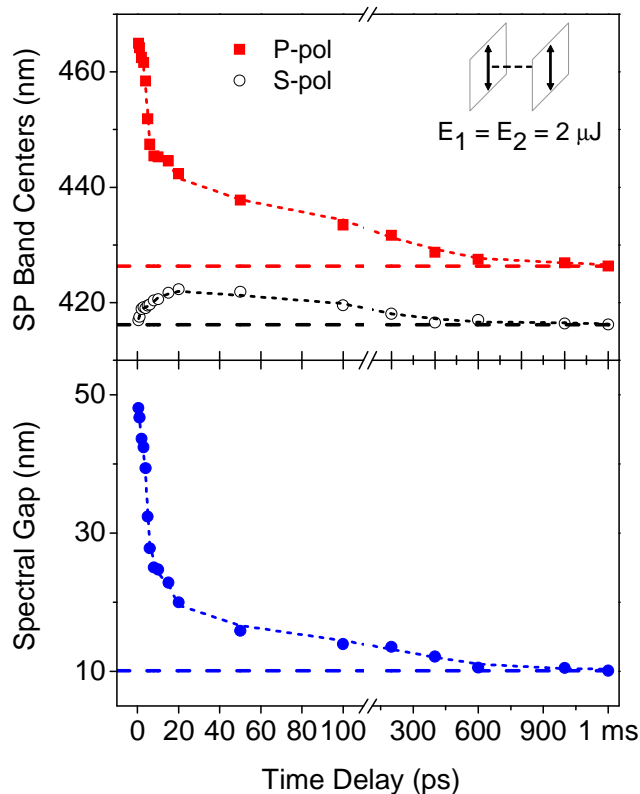


Fig. 5.3. Surface plasmon (SP) band centers (top panel) and the corresponding spectral gaps between SP bands (bottom panel) from irradiations with parallel-polarized pulse pairs of $2 \mu\text{J}$ of energy per pulse. The increments of the x -axes change after the axes break. Horizontal dashed lines on the top panel represent the P-pol (the one at 426 nm) and S-pol (the one at 416 nm) band centers of the $\Delta t = 1$ ms irradiation with the same pulse pair for comparison. The horizontal dashed line of the bottom panel represents the corresponding spectral gap of 10 nm.

spectroscopically) to the mechanisms started by (and remaining from) the first pulse. Therefore, we can verbally reduce the effect of the second pulse hitting the nanoparticle already at $\Delta t = 1$ ns as a pulse hitting a cold nanoparticle. It simply triggers the mechanisms from the beginning. The pulse energy is simply not enough to create longer-living dynamics.

Proceeding with the medium energy pulse pair irradiations (Fig. 5.4), we see again that the maximum spectral gap is produced for very short time delays. However, compared with the monotonous decreases in the spectral gaps of the low energy pulse pair irradiations (Fig. 5.3), the long-term picture is different for this more energetic case. The P-pol band centers go below the $\Delta t = 1$ ms irradiation line after a few picoseconds of time delay (the detailed views of short time delays will be presented in Ch. 5.3). Applying a second pulse to the disturbed nanoparticle is seen to be worse off for the induced spectral gaps compared with the $\Delta t = 1$ ms irradiation. Both S- and P-polarized bands are observed to sit on plateaus around 430 and 450 nm, respectively, right after $\Delta t = 20$ ps. This quasi-equilibrium situation lasts until 100 ps. During this time interval the spectral gaps of the bands are at their minimum values of 20 nm. After 100 ps of delay, the S- and P-polarized bands move away from each other, reaching their long-term steady-state positions (obtained by the $\Delta t = 1$ ms irradiation). It is seen that the spectral gaps increase rapidly (from 100 ps until 600

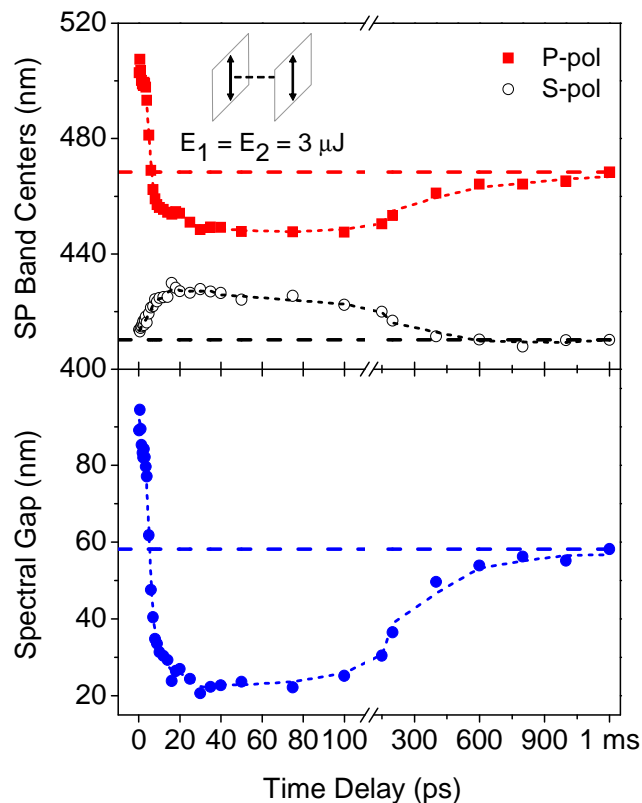


Fig. 5.4. Surface plasmon (SP) band centers (top panel) and the corresponding spectral gaps between SP bands (bottom panel) from irradiations with parallel-polarized pulse pairs of $3 \mu\text{J}$ of energy per pulse. The increments of the x -axes change after the axes break. Horizontal dashed lines on the top panel represent the P-pol (the one at 468 nm) and S-pol (the one at 410 nm) band centers of the $\Delta t = 1$ ms irradiation with the same pulse pair for comparison. The horizontal dashed line of the bottom panel represents the corresponding spectral gap of 58 nm.

ps) from 20 nm to 55 nm, and then they reach their steady-state values at longer delays. The nanoparticle system reaches a long-term equilibrium from several hundred ps until 1 ns with slowed-down dynamics. The spectral positions of the bands at 1 ms delay are observed to be only a few nm away from their 1 ns positions, which suggests the same argument developed above for the low energy pulse pairs. The spectra themselves are almost identical (see Figs. 5.1(a) and 5.1(f)). Compared with the low energy pulse pair irradiation, the spectral gap produced in the medium energy case is almost 6 times larger, which is 58 nm, at $\Delta t = 1$ ms.

Figure 5.5 shows the results of the high energy pulse pair irradiations. The dynamics observed for the delay intervals of $20 \text{ ps} < \Delta t < 100 \text{ ps}$ and $100 \text{ ps} < \Delta t < 600 \text{ ps}$ are similar to those of the medium energy irradiation case (Fig. 5.4), but the situation is much more dramatic here. The first point to notice is the overall ‘inefficiency’ of the second-hitting pulse for the nanoparticle aspect ratios, because the spectral gaps between the surface plasmon band centers are less for all Δt compared with the spectral gap achieved for $\Delta t = 1$ ms (which is 75 nm). It is clear that quickly applying pulse pairs of such high energy to the nanoparticle disturbs the nanoparticle in a worse manner compared to the irradiation with same pulse pairs applied with a delay of 1 ms. The minimum values of spectral gaps are obtained when the pulses are delayed in the $20 \text{ ps} < \Delta t < 100 \text{ ps}$ region, similar to the case

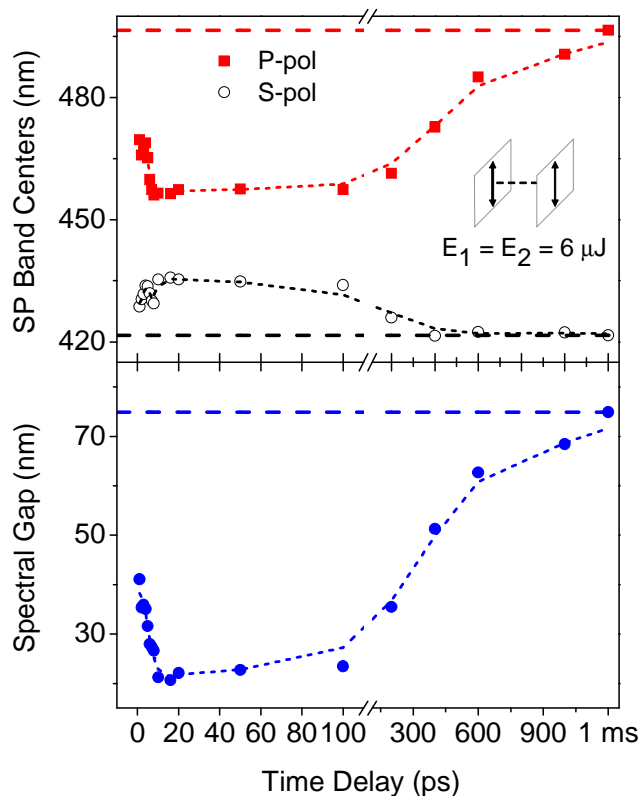


Fig. 5.5. Surface plasmon (SP) band centers (top panel) and the corresponding spectral gaps between SP bands (bottom panel) from irradiations with parallel-polarized pulse pairs of $6 \mu\text{J}$ of energy per pulse. The increments of the x -axes change after the axes break. Horizontal dashed lines on the top panel represent the P-pol (the one at 496 nm) and S-pol (the one at 421 nm) band centers of the $\Delta t = 1$ ms irradiation with the same pulse pair for comparison. The horizontal dashed line of the bottom panel represents the corresponding spectral gap of 75 nm.

shown in Fig. 5.4. We witness the separation of the surface plasmon band centers and thus the rise of the spectral gaps right after $\Delta t = 100$ ps. The rising behaviour of the spectral gaps continues hundreds of picoseconds, like it was observed in the case of medium energy pulse pairs. As the pulses are much more energetic here, it is clear that there are still some remaining processes, which were triggered by the first pulse, that go on even at $\Delta t = 1$ ns.

The discussion regarding the above presented results will be developed in the next sections starting from the shortest time delays (Ch. 5.3-5.5) and going to the longer (Ch. 5.6-5.7). Before proceeding with that, we now want to compare the results of parallel-polarized pulse pair experiments with the results of the orthogonal-polarized experiments.

5.2.2. Orthogonal-polarized pulse pairs

Figure 5.6 shows a comparable series of experiments applying orthogonally polarized pulse pairs. Some of the corresponding spectra for this irradiation were shown in Fig. 5.2. As the spectra at time delay zero suggested, the temporally overlapping pulses shift the band centers to the red side of the spectrum (with respect to the original band) without causing any spectral gap. Therefore the surface plasmon band centers start almost from the same spectral position at time delay 0. The spectral gaps shown in the bottom panel of Fig. 5.6 show that the maximum spectral gaps (up to 24 nm) are produced along the second-hitting pulse polarization for very

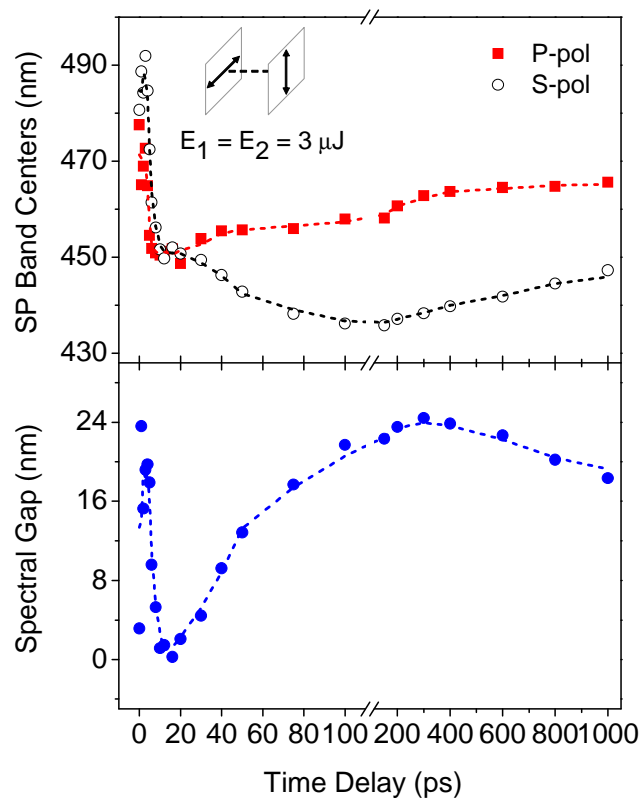


Fig. 5.6. Surface plasmon (SP) band centers (top panel) and the corresponding spectral gaps between SP bands (bottom panel) from irradiations with orthogonal-polarized pulse pairs of $3 \mu\text{J}$ of energy per pulse. The increments of the x -axes change after the axes break.

short delay times. The unresolved dynamics happening until 20 ps will be clearly shown and discussed in detail in the following sections. As we have already seen from the spectra shown in Fig. 5.2, the S- and P-polarized bands meet at $\Delta t = 10$ ps, resulting in 0 spectral gap (no dichroism). This situation is observed to continue until $\Delta t = 20$ ps.

Interestingly after this time, the bands are separated from each other; the P-polarized bands stay more or less constant but the S-polarized bands move towards to short wavelengths. Therefore, the spectral gaps rise rapidly to their maxima around 100 ps. It should be kept in mind that the aspect ratios induced to the nanoparticle are always along the second-hitting pulse polarization. That means, the second pulse hitting after $\Delta t = 20$ ps can benefit from the situation of the nanoparticle prepared by the events that were triggered by the first pulse. The prominent rise of the spectral gaps slow down after $\Delta t = 100$ ps and start to decrease roughly after $\Delta t = 600$ ps. Between 100 and 600 ps, the spectra themselves and the spectral gaps between the bands are more or less equal to each other. The observed behaviors of the bands are totally different compared with the parallel-polarized pulse pair irradiations but the critical Δt values that one can notice (such as 20, 100 and 600 ps) are basically the same. Although the irradiations are totally different from each other, the physical processes that determine nanoparticle shape changes should be the same for both of them.

In general one can identify three time intervals out of the above given results for parallel- and orthogonal-polarized pulse pairs. The first interval contains the fastest dynamics that start with the interaction of the first pulse with the nanoparticle and lasts up to 20 ps of time delay. The second time interval, from 20 ps to 100 ps, is observed to have some intermediate dynamics, which prepare the forthcoming long-term events. The last interval, with the so-called long-term dynamics, starts after 100 ps of time delay and goes up to 1 ns. The nanoparticle shape determining dynamics that continue to happen even at slower levels after 1 ns are hinted by the steady state data of $\Delta t = 1$ ms.

In the following, we will analyze and discuss the results presented above accordingly with their temporal order. We will start with the fastest mechanisms induced to the nanoparticle with the strong laser pulse interaction. This time interval ($0 < \Delta t < 20$ ps) contains the most important physical events that trigger all the forthcoming intermediate ($20 < \Delta t < 100$ ps) and long-term dynamics ($100 \text{ ps} < \Delta t$).

5.3. First 20 ps of nanoparticle shape modifications

To investigate the fastest physical events acting on the nanoparticle, we will first present the detailed views of surface plasmon bands for the first 20 ps of time delay extracted from the above given results. Here the shifts of the plasmon bands will be presented together with the corresponding band integrals for a better understanding of the temporal behavior of the nanoparticle absorption dynamics. Afterwards we will discuss and develop the possible physical mechanisms that may be responsible for the experimental observations of this time interval in Ch. 5.4 and 5.5. As it was done in the previous section, we will again present a total of four sets of results; three for parallel-polarized pulse pair experiments with varying pulse energies (Figs. 5.7-5.9) and one for orthogonal-polarized pulse pair experiment with medium energy pulses (Fig. 5.10).

One of the common points for all three parallel-polarized experiments is that for time delay larger than $\Delta t \approx 3$ ps, the P-band position shifts to smaller, the S-band position slightly towards longer wavelengths. At $\Delta t \approx 10$ ps, this decrease of the induced dichroism stops; for larger Δt (up to 20 ps) the positions of the SP bands (spectral gap) remain almost unchanged. The results of the low energy pulse pair irradiation (Fig. 5.7) show that the P-pol band centers are above the red dashed line (P-pol of $\Delta t = 1$ ms) for all delay times. Although the P-pol band centers shift to

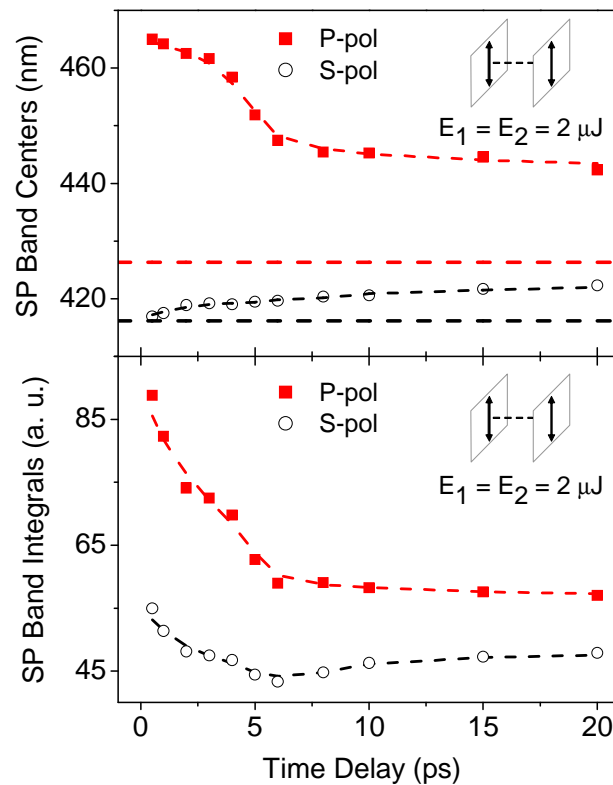


Fig. 5.7. Surface plasmon (SP) band centers (top panel) and the corresponding band integrals (bottom panel) from irradiations with parallel-polarized pulse pairs of $2 \mu\text{J}$ of energy per pulse. Horizontal dashed lines on the top panel represent the P-pol (the one at 426 nm) and S-pol (the one at 416 nm) band centers of the $\Delta t = 1$ ms irradiation with the same pulse pair for comparison.

lower wavelengths for long delay times, the band center at $\Delta t = 20$ ps still lies ~ 15 nm above the 1 ms line. This indicates that for low energy pulses, the second pulse applied to the nanoparticle is always better off for the nanoparticle system (inducing higher spectral gaps). As already stated, the best situation of a high spectral gap occurs when both of the pulses hit the nanoparticle quickly within the first 3 ps.

The case depicted in Fig. 5.8 (the results of the medium energy pulse pair irradiation) is a little different, where the P-pol band centers go below the $\Delta t = 1$ ms irradiation line right after $\Delta t \approx 5$ ps. Applying a second pulse to the disturbed nanoparticle after 5 ps until 20 ps is seem to be worse off for the induced spectral gaps compared with the 1 ms irradiation. The short-term results of the case with high energy pulse pairs (Fig. 5.9) are also interesting in the sense that the P-pol band centers here are always below the band center of 1 ms irradiation. As stated before, quickly applying pulse pairs of such high energy to the nanoparticle disturbs the nanoparticle in a worse manner compared to the irradiation with a delay of 1 ms.

The surface plasmon band centers of each figure are also accompanied by the corresponding band integrals. We know that decreases in band integrals together with the decreases in spectral gaps between the band centers indicate the volume shrinking of the nanoparticle over time. In Fig. 5.7 directly after time delay zero, both band integrals start to decrease until $\Delta t \approx 5$ ps. At larger temporal distance of the pulse pair, the P-pol band integral remains constant, while the S-pol band integral

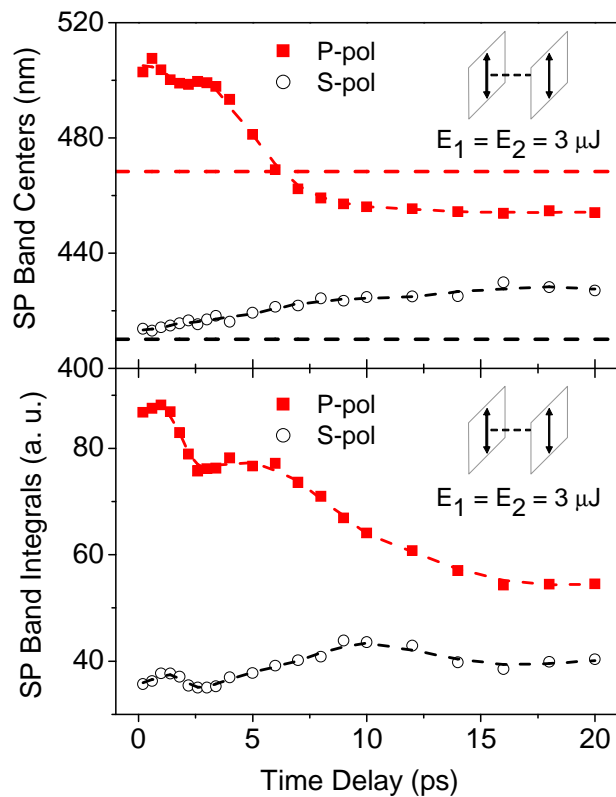


Fig. 5.8. Surface plasmon (SP) band centers (top panel) and the corresponding band integrals (bottom panel) from irradiations with parallel-polarized pulse pairs of $3 \mu\text{J}$ of energy per pulse. Horizontal dashed lines on the top panel represent the P-pol (the one at 468 nm) and S-pol (the one at 410 nm) band centers of the $\Delta t = 1$ ms irradiation with the same pulse pair for comparison.

is slightly recovering. Over all, we can say that the total absorption of the nanoparticle system is significantly reduced when the delay between the two pulses is increased to 5 ps or more.

The P-pol band integrals of Fig. 5.8 decrease gradually as the time delay increases, while the S-pol band integrals remain more or less constant around 40. Even though this behavior of the band integrals does not have much similarity compared with the band integrals of Fig. 5.7, the end comment regarding the reduced amount of total absorption holds also for this case. On the other hand, the band integrals depicted for the high energy pulse pair irradiation (Fig. 5.9) do not agree well with the others. The P-band integrals stay almost constant, while the S-band integrals display a slight increase, which must indicate some increase in the total absorption of the nanoparticle system with increasing delay time. This can make sense considering the added amount of absorption due to the high number of small silver clusters around the disturbed main nanoparticle for such high energy irradiations.

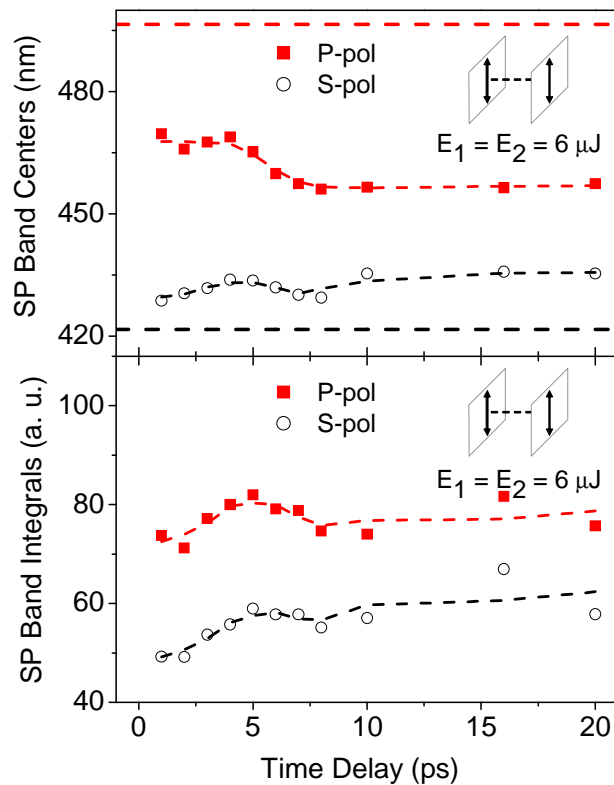


Fig. 5.9. Surface plasmon (SP) band centers (top panel) and the corresponding band integrals (bottom panel) from irradiations with parallel-polarized pulse pairs of $6 \mu\text{J}$ of energy per pulse. Horizontal dashed lines on the top panel represent the P-pol (the one at 496 nm) and S-pol (the one at 421 nm) band centers of the $\Delta t = 1 \text{ ms}$ irradiation with the same pulse pair for comparison.

Figure 5.10 presents the first 20 ps results of experiments with orthogonal-polarized pulse pairs. As it was mentioned before, the first important feature is observed at time delay zero, where no spectral gap between the polarized plasmon bands can be observed. However, already at a time delay of $\Delta t = 1 \text{ ps}$ between the two pulses, dichroism with a considerable spectral gap of $> 20 \text{ nm}$ occurs. The P-pol

band centers are along the polarization direction of the second-hitting pulse (i.e. horizontal-polarized). This state, where a spectral gap is observed is only valid for a limited range of time delay: already for $\Delta t > 3$ ps the centers of both S- and P-bands start to experience smaller red-shift (from the original SP band of Ag nanoparticles) upon irradiation, and a smaller spectral gap is produced. These trends continue until at $\Delta t = 10$ ps, when the dichroism vanishes (spectral gap ≈ 0 nm); after this time delay the situation remains unchanged. Both of the band integrals decrease gradually until 10 ps, indicating a decrease in nanoparticle absorption, and they reach a stable situation at their minimum values around this time.

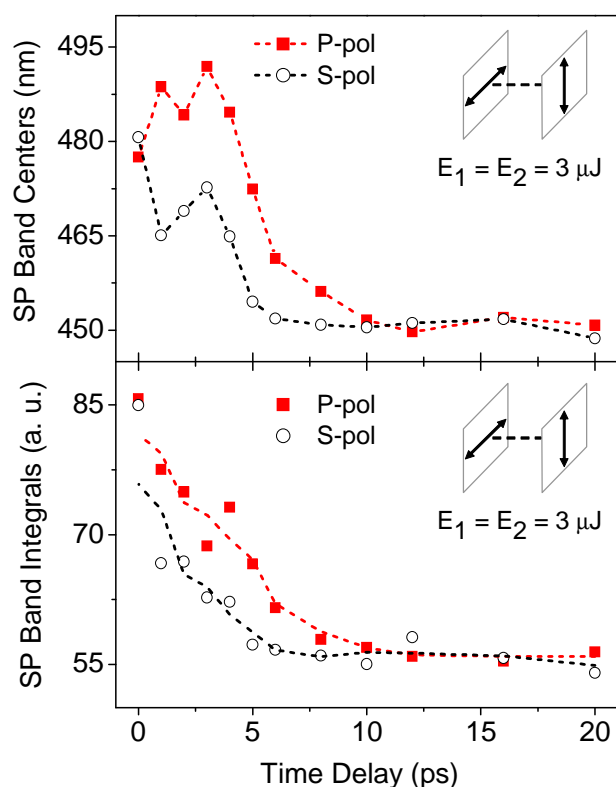


Fig. 5.10. Surface plasmon (SP) band centers (top panel) and the corresponding band integrals (bottom panel) from irradiations with orthogonal-polarized pulse pairs of $3 \mu\text{J}$ of energy per pulse.

Comprising all the above given short-term results (Figs. 5.7-5.10), we can give a first qualitative interpretation. Obviously the first pulse initiates ultrafast processes changing the state of the nanoparticle and its surrounding strongly during the first few picoseconds. With increasing time delay Δt , the second pulse causes a monotonous decrease of the band integrals, which is most plausibly explained by volume shrinking (partial dissolution) of the nanoparticles. This indicates, together with the behavior of the band centers in the case of orthogonal-polarized pulses, an isotropic process – tentatively ion emission – which prevents the second pulse from creating a directional memory for nanoparticle reshaping.

The band centers show the largest spectral gaps for time delay $\Delta t \leq 3$ ps for parallel-polarized pulse pairs; and in the case of orthogonal-polarized pairs the second pulse can redirect the directional memory within this interval of time. Most

probably, these observations can be attributed to the directed electron emissions. Therefore these processes will be in the focus of the following discussion.

5.4. Nanoparticle ionization through electron emissions

If the evidently occurring electron and ion emission processes would be purely thermal, the anisotropy of the nanoparticles after irradiation could not be explained at all. Therefore, we have to investigate the possible electron emission processes in more detail, in particular those happening during the pulse interaction, because the strong field of a linearly polarized laser pulse is the only reasonable source of a directional preference. According to the Mie theory [5], the surface plasmon oscillations of spherical particles are either dipolar or multipolar in character depending on their sizes [6]. For particles having sizes much smaller than the wavelength of the exciting electromagnetic field ($d \ll \lambda$), it is sufficient to consider only the first term of the multipolar expansion, i.e., the dipolar term. In this case of small enough nanoparticles, hot electrons can be injected into the surrounding glass matrix along the direction of the laser polarization during interaction with the applied pulse. The probability of this process is clearly correlated to the availability of electronic states of the surrounding medium. Therefore, the next section is devoted to the description of the electronic states of the glass-nanoparticle system.

5.4.1. Electronic band structure of composite glass containing silver nanoparticles

The glass matrix embedding the metal nanoparticle can influence the energy levels of the nanoparticle. It is known for dielectrics (e.g. glass) that their ionization requires high photon energies due to the large energy gap between the valence and conduction bands. If the photon energy of excitation is less than the energy gap, the ionization due to single photon absorption is excluded, which proves the difficulty of ionizing the glass. However, the glass matrix itself opens up an additional damping mechanism for the surface plasmon modes of the nanoparticle [7], and its free conduction bands supply an inviting reservoir for nanoparticle electrons. When the energy of the occupied nanoparticle states coincide with the electronic states of the glass matrix, the conduction electrons of the nanoparticle are transmitted through the interface, escaping from the nanoparticle potential (Ch 3.2.3). In such a case, the electrons are no longer confined with the nanoparticle, which is a typical mechanism for the nanoparticle plasmons [7].

In the case of silver nanoparticles embedded in glass, the occupied states of the nanoparticle coincide in their energy with the electronic states of the glass as shown in Fig. 5.11. The valence band maximum of the glass lies 10.6 eV below the vacuum level (i.e., -10.6 eV), and therefore it has no influence on the silver nanoparticle surface plasmons. On the other hand, the lowest conduction band has a bandwidth of around 4 eV [7] and the band minimum occurs around -1.7 eV. Comparing this with the Fermi level of Ag, which lies at -4.3 eV, yields a 2.6 eV gap in between the Fermi level of the silver nanoparticles and the conduction band of the glass matrix. It is noteworthy to see that this energy is lower than the energy of the

surface plasmon resonances of Ag nanoparticles in glass ($\hbar\omega_{SP} \approx 3$ eV). This proves that it is possible for a surface plasmon to decay by injection of a hot electron (with $E \geq 2.6$ eV) into the glass conduction band [8]. Therefore, our irradiation at 3.1 eV, which is very close to the surface plasmon resonance, can provide considerable probability for the nanoparticle electrons to penetrate into the glass conduction band(s) within the pulse duration, which enables the probability of anisotropic electron emissions from the nanoparticle.

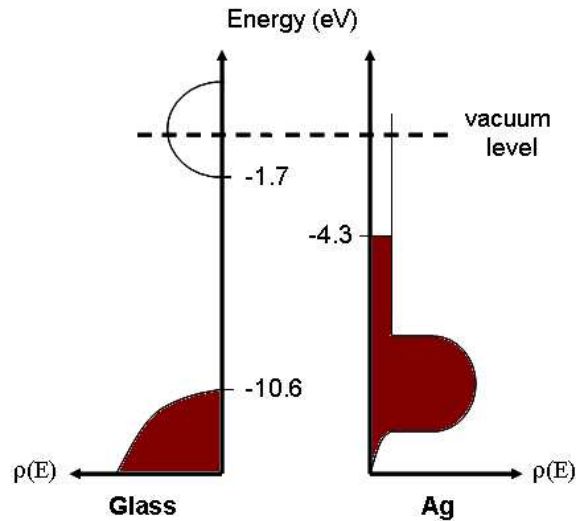


Fig. 5.11. Left: the density of states of glass, where only the lowest conduction band is depicted. Right: the occupied and unoccupied density of states of bulk silver. The figure is adapted from [8].

But what happens after the ultrashort pulse has gone away? Will there be still some probability for the thermalized electrons to penetrate into the glass conduction bands? To answer such questions and to establish a further understanding, the effect of irradiation on the nanoparticle density of states is depicted in Fig. 5.12. The figure shows the Fermi distributions of an electronic system before (with $T_e = 300$ K) and after absorbing the $\hbar\omega_L = 3.1$ eV laser pulse. As it was described in Ch. 3.2.1, the laser pulse excites the electrons right below the Fermi level to high energies in a very short time scale, thereby creating an athermal electronic distribution. This laser excitation process is represented by the arrows in Fig. 5.12. As suggested above, it is seen that the laser pulse energy is enough for electrons to be excited 2.6 eV above the Fermi level of silver. This will greatly enhance the probability of anisotropic electron emissions. In the following times, the electrons thermalize to form a hot Fermi distribution, which is depicted by the red, solid curve in the figure. The high energy tail of the high T_e Fermi distribution gives an answer to the questions above as it exceeds the energy needed for nanoparticle electrons to penetrate into the glass conduction band (2.6 eV). As the directionality of the pulse is no more there, these thermal emissions of electrons are isotropic. Therefore, it is obvious regarding the given Fermi distributions that the nanoparticle injects hot electrons into the glass during and after the laser pulse interaction.

This gives rise to two different types of electron emission processes, which we will classify according to their nature of occurrence as 'pulse-enhanced' or 'purely thermal' in the following; the first being anisotropic and the second being isotropic. The isotropic purely thermal electron emissions start after the pulse has gone away

and continue to happen as long as the electrons possess high temperatures. The pulse-enhanced electron emission processes, on the other hand, comprise a ‘direct’ and a ‘pulse-enhanced thermal’ electron emission component. The direct electron emission processes are the fastest that happen within the first few plasmon oscillation periods, the details of which have been described in Ch. 3.2.3. The second component of the pulse-enhanced electron emissions is thermal in nature, owing to the increased electron temperatures along the plasmon oscillation directions. Such anisotropic thermal electron emissions are indeed possible because the electrons that gain very high temperatures during the pulse are driven out from the nanoparticle by the dipolar plasmon oscillations.

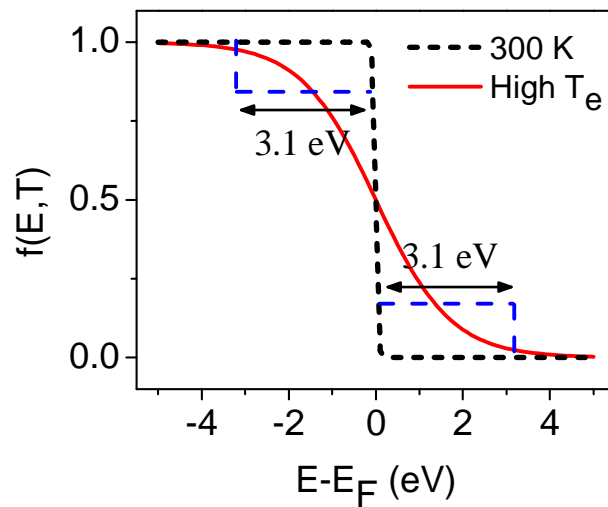


Fig. 5.12. Changes in the Fermi distribution of the electronic system following an ultrashort laser pulse irradiation at an energy of 3.1 eV, which excites electrons below the Fermi level to high energies (represented by the arrows). The resulting hot electronic distribution is shown with the solid curve.

Before proceeding with the discussion of the pulse-enhanced and purely thermal electron emission processes, we will introduce the model calculations based on the extended TTM and the band structures of composite glass.

5.4.2. Modeling of nanoparticle ionization with the extended TTM

As described above, we will in the following call all field-driven electron emissions from nanoparticles (except the fastest direct emissions) occurring during interaction with a laser pulse by the notion ‘pulse-enhanced thermal emission’ (PETE). When the laser pulse is terminated, the electronic system is still very hot (Fig. 5.12), and thus there are still enough electrons at energies allowing them to enter the glass conduction band just by a diffusive process. We will call this comparably long-lived process as isotropic thermal emission (ITE) of electrons. For all the emitted electrons there is a certain probability that they lose their energy rapidly and are eventually trapped at local potential minima forming color centers in

the glass [9, 10]. These trapped electrons play an important role in reducing Ag cations at later times.

To get a better understanding of the time evolution of the thermal emission processes, we calculated the Fermi distribution as a function of T_e (a Fermi distribution for each T_e value of Fig. 5.13(a)), and used the resulting amount of electrons above 2.6 eV as an estimate for the relative electron emission probabilities. Figure 5.13(b) shows this percentage of electrons, referring to the situation of Fig. 5.13(a) as a function of time.

For the presence time of the laser pulse we add probability to the PETE process (blue, solid line), after the end of the pulse the percentage of high-energy electrons is assigned to add probability to the ITE process (red, dashed line). Thus, integration over the pulse duration (start and end of pulse defined by $1/e^2$ intensity) and the whole remaining time interval afterwards yields the total relative probabilities ($\sum P$) of the two processes. These integrals are shown as shaded areas under the curves in the inset of Fig. 5.13(b). The absolute probabilities are unknown, but it is obvious to anticipate higher probability for the PETE process to account for the experimentally observed anisotropy [11].

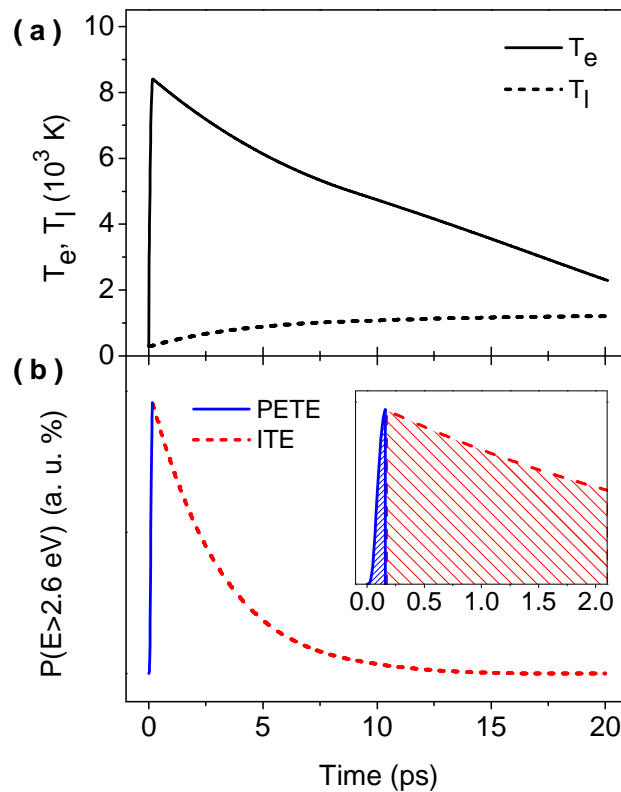


Fig. 5.13. (a) Time evolution of electronic and lattice temperatures of a silver nanoparticle following the absorption of an intense fs laser pulse. (b) Probabilities of electrons that possess energies above 2.6 eV as a function of time. Pulse-enhanced thermal emission (PETE) happens during the pulse (rising curve) and isotropic thermal emission (ITE) after the pulse (decaying curve). Inset of (b): First 2 ps of PETE and ITE with shaded areas showing the total probabilities for both processes.

5.4.3. Pulse-enhanced and isotropic thermal electron emissions for pulse pair irradiations

To account for the temporal behavior seen in the experimental results, we now consider the relative probabilities of pulse-enhanced thermal emission (PETE) and isotropic thermal emission (ITE) of electrons for the cases of parallel and orthogonal-polarized pulse pair irradiations. Starting point is again the extended two-temperature model, which is now applied to estimate the electronic temperatures for the case of pulse pair irradiation of a nanoparticle.

Figure 5.14 shows the resulting time evolution of electronic and lattice temperatures calculated for several cases of irradiation with a pulse pair (energy matching the experimental values) at time delays of $\Delta t = 0, 2, 5$ and 20 ps. In the case of exact temporal overlapping of the pulses (Fig. 5.14(a)), the electronic temperature can rise as high as 11000 K. When the pulses are separated from each other, e.g. by 2 ps (Fig. 5.14(b)), the first pulse is observed to create a maximum T_e value of ~ 8000 K, and the second pulse hitting the already hot nanoparticle increases the electronic temperature again; however, it is not as prominent as the first pulse effect because of the increased electron heat capacity. Therefore the maximum T_e to be achieved is around 10000 K. Increasing the delay further changes the maximum amount of T_e value to be created by the second pulse. Figures 5.14(c) and 5.14(d)

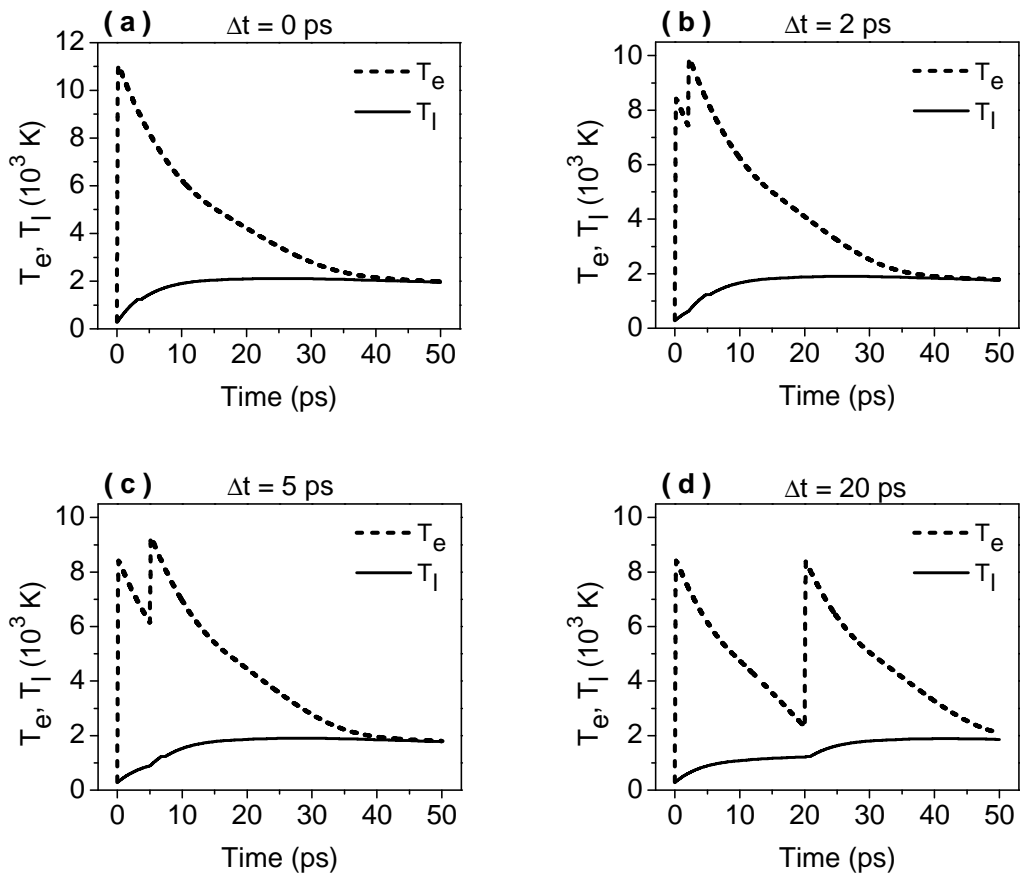


Fig. 5.14. Time evolution of electronic and lattice temperatures for pulse pair irradiation with (a) $\Delta t = 0$ ps, (b) $\Delta t = 2$ ps, (c) $\Delta t = 5$ ps and (d) $\Delta t = 20$ ps.

show that the efficiency of the second pulse decreases as the time delay increases. But a common point to all scenarios is that any temperature increase given to the electronic system causes the lattice temperature to rise more steeply.

To estimate the relative contributions of PETE and ITE processes, we applied the same procedure as described above for Fig. 5.13. That is, we calculated the percentage of electrons having energy above the Fermi level with $E > 2.6$ eV as a function of time by constructing a separate Fermi distribution for each T_e value. As an example, Fig. 5.15 shows the resulting probability distributions for the time delay of $\Delta t = 5$ ps, which are calculated from the electronic temperatures shown in Fig. 5.14(c). The probability distributions are calculated in this manner for each time delay Δt between pulse pairs (from 0 to 20 ps).

From this set of probability distributions, the total relative probabilities (ΣP) can be calculated as shown in the inset of Fig. 5.13(b). Integrating over the time intervals where a laser field is present yields the total relative probability for the PETE processes during first and second pulse (regions indicated by blue, solid lines in Fig. 5.15). Integration over the remaining time (no laser field) gives the total relative probability for ITE processes (regions indicated by red, dashed lines in Fig. 5.15). Finally, performing this procedure for the whole range of time delay between pulse pairs from perfect overlapping at $\Delta t = 0$ ps to a maximum delay of 20 ps, the total relative probabilities of PETE and ITE processes are obtained as a function of the temporal sequence of the two pulses.

Now we have to compare these calculated numbers with the experimental results presented in the previous sections. Experimentally, we have investigated the two cases of parallel and orthogonal polarization of the pulse pairs, which imply a characteristic difference: The integrated probability of ITE processes does only depend on the current electronic temperature and thus the total amount of absorbed energy, but is not at all sensitive to the laser pulse polarization – the reason why it is called isotropic. In contrast, the PETE processes were assumed to be field-driven, i.e.

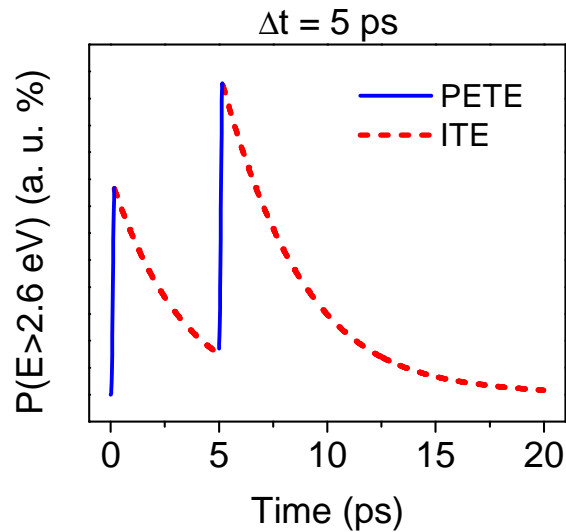


Fig. 5.15. The corresponding probabilities of electrons that possess energies above 2.6 eV for the case of $\Delta t = 5$ ps, which was given in Fig. 5.14(c).

to produce a directional distribution of electron emission which reflects the actual laser polarization. With respect to this definition, the amount of anisotropy initiated by the PETE processes in case of parallel polarization of the pulse pair must be related to the sum of the PETE probabilities. For orthogonal polarization of a pulse pair, one expects a relation to the difference of PETE probabilities, because directed emission of exactly the same amount of electrons in parallel and perpendicular direction can not produce anisotropy of lowest (dipolar) order.

According to these considerations, Fig. 5.16 shows the integrated probability for ITE processes only once (upper panel), while in the lower panel both sum (open triangles) and difference (open circles) of the PETE probabilities, integrated separately over first (PETE1) and second pulse (PETE2), are plotted. It is most instructive to look at the difference (PETE2 - PETE1) first: While at $\Delta t = 0$ the two contributions cancel each other as expected, already a few 100 fs time delay of the pulses leads to a clear prevalence of pulse-enhanced electron emission probability due to the second pulse. This can easily be explained by the fact that the second pulse can interact with an already very hot electronic system. With increasing Δt , the difference decreases down to zero at $\Delta t \approx 15$ ps. Over all, this behavior almost perfectly matches the experimentally observed dichroism as a function of Δt (Fig. 5.10), as well as the finding that the second of two energetically equal pulses defines the direction of anisotropy. It is obvious to conclude that pulse-enhanced thermal emission of electrons into the matrix is the key process initiating the directional memory for the following shape transformation of the Ag nanoparticles.

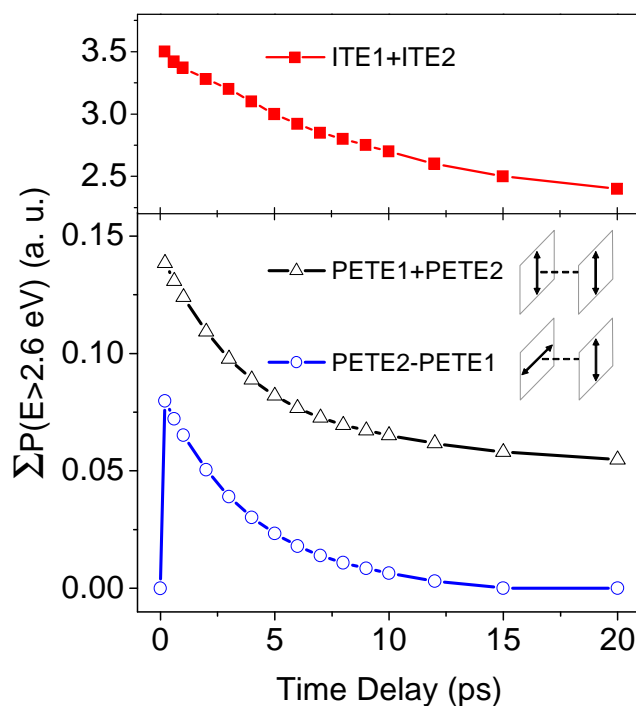


Fig. 5.16. Added probabilities of ITE (isotropic thermal emissions) and PETE (pulse-enhanced thermal emissions) for selected delay times. ITE1 (PETE1) represents the isotropic (pulse-enhanced) thermal emissions due to the first pulse, and so on. ITE of both pulses are added to each other (owing to the isotropy). PETE of pulse pairs are added when the pulses are parallel-polarized and subtracted when the pulses are orthogonal-polarized.

This interpretation is confirmed considering the sum (PETE1 + PETE2): First, the larger values of the total PETE probability corresponds nicely to the larger amount of anisotropy (spectral gap) observed for parallel-polarized pulse pairs (e.g. Figs. 5.7 and 5.8). Second, the sum decreases by more than a factor of 2 when the pulse delay increases from very small Δt to $\Delta t \approx 10$ ps; the experimentally observed reduction of the spectral gap of the SP bands happens also on the same time scale.

Using the above given added probabilities it is possible to test the quantitative relationship between PETE and ITE processes by calculating the ratios of ‘PETE / ITE’ over the delay time. The ratios for parallel- and orthogonal-polarized pulse pairs, which are calculated directly from Fig. 5.16, are shown in Fig. 5.17. The time evolution of these ratios yields the efficiency or the validity timescale of nanoparticle anisotropy. As expected, very high ratios are observed for short time delays. Such high ratios mean that the PETE processes for both experimental situations are much more efficient than those of the ITE processes when the irradiations are carried on with pulse pairs following each other quickly in time (except $\Delta t = 0$ of the orthogonal-polarized pulse pairs, which is simply 0). With the increasing Δt , the ITE processes start to balance the situation, gradually creating plateau regions after 10 ps. Out of these ratios we can say that there will be a high anisotropy of electronic distribution for short delay times owing to the strong PETE processes. However, for irradiations at longer Δt , the isotropic thermal emissions are also as strong as the anisotropic emissions, thereby they can reduce the total anisotropy of the nanoparticle for the parallel-polarized pulses and remove it all for the orthogonal-polarized pulses. The exponential lifetimes of the ratios yield values on the order of 3-4 ps for both processes. Comparing with the experimental results given in the Ch. 5.3, it is seen that they correspond quite well with the temporal regions of the highest spectral gaps.

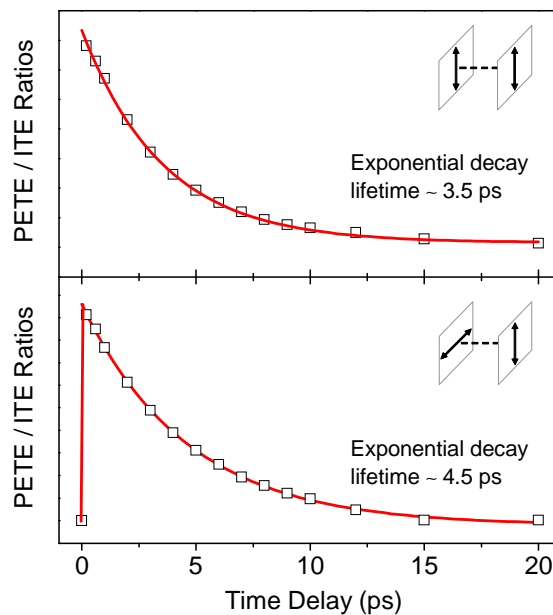


Fig. 5.17. Ratios of the added probabilities of PETE to ITE (from Fig. 5.16) for parallel (top panel) and orthogonal (bottom panel) polarized pulse pairs. The exponential fits show the rates of decrease in anisotropy with the increasing time delay between pulse pairs. The lifetimes correspond nicely with the experimental observations.

We can now consider which physical processes cause the reduction of the anisotropy for parallel-polarized pulse pairs and the full disappearance of it for orthogonal-polarized pulse pairs within 10 ps. Clearly the purely thermal emission of electrons (ITE) is the first candidate: when isotropic injection of electrons into the glass has been going on long enough, all available trapping sites [10] close to the nanoparticle will be occupied. Electrons emitted by a second pulse interacting after this time can, if at all, can only be trapped at sites further away from the nanoparticle. For parallel-polarized pulse pairs, these sites are also already occupied by PETE during the first pulse, so the electrons emitted by the second one will diffuse back to the nanoparticle, and as a result the anisotropy is not increased. In the case of orthogonal-polarized pulse pairs, there are free sites in the emission direction, and the anisotropy can be cancelled. So, already this simplified scenario of saturation of the trapping sites can provide a reasonable explanation for the observed dependence of the dichroism on the pulse delay time Δt [11].

There are, however, further processes which might start within the first picoseconds after the laser pulse interaction. In particular, any process of electron emission (no matter if directed or isotropic) ionizes the nanoparticle. The positively ionized and heated nanoparticle is therefore electrically and thermodynamically in an unstable state. Electrical instability rapidly shows itself as repulsive Coulomb forces among the silver cations. Together with strongly increased temperature this finally leads to emission of ions (known as Coulomb explosion), reducing the total volume of the nanoparticle [9, 12, 13]. This process, which we will investigate in the following section, is isotropic in nature, creating a considerable density of ions around the main nanoparticle.

5.5. Repulsive Coulomb forces on the ionized nanoparticle

For small Na clusters the typical time scale for Coulomb explosion was reported to be around 0.5 – 1 ps [14]. It is reasonable to assume a somewhat slower time scale for the emission of Ag ions from our comparably large nanoparticles embedded in a rigid matrix. This is well compatible with the experimentally observed decrease of the spectral gaps between polarized extinction bands and the decrease of band integrals as a function of time delay (see Figs. 5.7, 5.8, and 5.10 – excluding the too strong irradiation of Fig. 5.9). As the spectral gap between the polarized bands is strongly dependent on the aspect ratio (a/c) of the modified nanoparticles, the decrease in spectral gap can be associated with the dissolution of the nanoparticle due to repulsive Coulomb forces. Both the spectral gaps and the band integrals come to their minimum values around 10 ps and stay constant until 20 ps. The decrease in overall amount of band integrals, corresponding to the same temporal delays with the decrease in spectral gaps, suggests that the nanoparticle system starts to absorb less and less in time, as the total volume of the particle is decreasing over time. From the short term data, only the constant behavior of the band centers and integrals from 10 to 20 ps is seen, but it is also very important to know how long they stay so to comment on the fate of the ion emission processes.

At the moment we can say that ion emissions start at least within the first few picoseconds after the pulse interaction with the nanoparticle, and this will strongly

change the state of the nanoparticle and its surroundings. For instance, the dissipated kinetic energy of the Ag ions will lead to a fast temperature increase in the glass matrix close to the nanoparticle, which might remove the trapping sites for electrons. Also a loss of the silver crystal structure could result in a strongly modified reaction of the nanoparticle to the second laser pulse. All those secondary processes have the potential to prevent the preparation of an anisotropic distribution of trapped electrons, and offer plausible explanations that a second pulse coming in more than 10 ps after the first one can not increase the produced persistent dichroism [11].

Summarizing this part ($\Delta t = 0 - 20$ ps), we can point out that the experimental results combined with the theoretical modeling give evidence that field-driven emission of hot electrons into the glass matrix is the dominating starting process for the fs laser induced reshaping of Ag nanoparticles. As a result of the ionization, the nanoparticle emits ions to the surrounding glass matrix by Coulomb forces, which is observed by the experimental results described above. However, as stated above, 20 ps of time scale is not enough to understand the fate of the emitted ions and the nanoparticle system as a whole.

The whole process of shape transformation requires several further cascaded mechanisms on increasingly slower time scales. To name a few of them, the emitted ions can be reduced by previously emitted, trapped electrons; owing to the directional distribution of these electrons, this reduction happens mainly close to the poles of the nanoparticle along the second-hitting pulse polarization. Due to the increased temperature of the glass matrix in the vicinity of the particle, which is mediated first by emitted electrons and ions and then by normal heat conduction, the reduced Ag atoms may either diffuse back to and reaggregate with the original nanoparticle, or form small silver clusters in its surroundings. Irradiating several hundred pulses, this gradually leads to the nanoparticle shape changes and the usually observed halo of small silver clusters [15, 16]. To investigate the time scales of these long-living mechanisms and to provide additional insight for the nanoparticle shape modifications, we will discuss the requirements and consequences of these processes in the following sections.

5.6. Mobility of emitted silver ions

Starting with the parallel-polarized pulse pair experiments, there are essentially two clear observations from the long-term results ($\Delta t > 20$ ps) given in Ch. 5.2. The first one is the surface plasmon dynamics happening until 100 ps, where the spectral gaps remain constant at their minimum values for the medium and high energy irradiation cases. The second observation comprises the longer delays, especially up to 600 ps, where the spectral gaps increase for the medium and high energy cases. For the low energy pulses (corresponding to the threshold for nanoparticle modification), only the monotonous decrease of the spectral gaps is observed, which is basically due to the insufficient energy of the pulses.

To account for the experimental results, it is necessary to investigate the thermal situation of the glass in the vicinity of the nanoparticle [17]. This task includes the calculation of the nanoparticle cooling together with the glass heating,

which is essentially the heat transfer between two systems. Indeed for the nanoparticle shape changes to take place, one should expect that the glass matrix surrounding the nanoparticle should get softened at least for some period of time. This depends of course on the initial temperature of the nanoparticle lattice, therefore the initial energy given to the nanoparticle by the laser pulse. In this sense, it is quite obvious that in addition to different degrees of electrical situations (i.e. nanoparticle ionization and Coulomb explosion) created by different energy pulses, very different thermal situations affecting the nanoparticle and its surroundings can also be induced by the different energy pulses. Therefore each set of experimental data (employing different pulse energies) reflect different degrees of ionization and thermalization processes. Our aim is to find the possible physical mechanisms to the basic understanding of the experimental observations rather than the modeling of each specific data set.

The cooling of the hot nanoparticle can be calculated by the classical heat transfer equation (Eq. 3.12), where the energy flow from the hot nanoparticle to the glass should be estimated step by step through concentrated spherical shells. The actual values of the nanoparticle lattice temperatures are used directly from the two-temperature model. Due to the huge difference in thermal diffusivities of Ag ($123 \text{ nm}^2/\text{ps}$) and glass ($0.5 \text{ nm}^2/\text{ps}$), the spatial temperature changes within the nanoparticle can be neglected. Therefore, the heat equation yields the temporal and spatial evolution of the heat transfer within the glass. The solutions of the heat equation (modeling the case of $E = 3 \text{ }\mu\text{J}$ pulse irradiation) show that the glass 1 nm and 3 nm away from the nanoparticle surface reaches temperatures around 600 K and 350 K, respectively, within 200 ps following the pulse irradiation. Higher irradiation strengths (i.e. pulse energies) will of course induce higher temperatures to the glass. In the following times the heat is diffused deep away into the glass slowly. As the nanoparticles are several hundred nanometers away from each other, the influence of the heat coming from the neighboring nanoparticles is negligible.

We should also note that the thermal diffusion alone cannot account for the full relaxation and cooling mechanisms of the nanoparticle. As it was mentioned before, the ionization of the nanoparticle and the consequent dissolution (ion emission) mechanisms are effective cooling processes. From the glass side, these mechanisms are additional heating processes of the glass together with the classical heat diffusion. The dissipated kinetic energy of the emitted Ag ions leads to a fast temperature increase in the glass matrix close to the nanoparticle. Taking into consideration these emission processes as coolers of the nanoparticle and heaters of the glass, we can say that the glass matrix in the vicinity of the nanoparticle gets hot and soft even at earlier times (earlier than 200 ps) following the pulse interaction. Indeed the melting of gold nanoparticles suspended in water has been observed to take place within 100 ps following the intense laser pulse excitation (comparable with the fluences employed in our studies) [18, 19].

Therefore, the experimental results for medium and high energies (Figs. 5.4 and 5.5), showing long plateau regions at the minimum spectral gaps until 100 ps, are most probably due to the high ionic mobility in the softening glass. The ions that are emitted from the nanoparticle surface experience a radial force due to the Coulomb explosion. The kinetic energy inputted into the ions will determine the range of their travel. In this sense very high irradiation energies (higher than the case depicted in

Fig. 5.5) will definitely cause enormous ionization conditions, which leads to the destruction of the full nanoparticle into ions.

The emitted ions decrease the volume of the nanoparticle, and they do not contribute to the surface plasmon bands until they are reduced and recombine with the nanoparticle again. The prerequisite for the reduction of these ions is the existence of untrapped electrons. It was mentioned in Ch. 4.4 that the emitted electrons are trapped in the glass potential minima (i.e. color centers), which can only be removed if the glass temperature is high enough. Until the glass temperature is high enough to free the trapped electrons, ions wander around depending on the energy they possess. This is an interesting situation, where the ionic mobility is expected to get enhanced in a soft glass but on the other hand the mobility of the ions contribute to the softening of the glass. Considering them together with the classical thermal heat diffusion from the hot nanoparticle, we can say that a hot sphere of glass surrounding the nanoparticle houses the emitted ions. As discussed above, the volume of the hot glass depends on the irradiation conditions, i.e. the energy input given to the nanoparticle. Extreme irradiation cases can cause a molten state of the glass, which in turn can diffuse the emitted Ag ions away from the main nanoparticle, resulting in its complete dissolution.

The experimental results suggest that the reduction and precipitation of the silver ions are less probable until 100 ps, because the spectral gaps (and the nanoparticle aspect ratios) are at their minimum levels. This minimum level corresponds to the nanoparticle with a reduced volume. To see the plausibility of this remark, we can check the corresponding band integrals as they contain information regarding the total absorption of the nanoparticle. Figure 5.18 shows the band integrals of the medium energy pulse pair irradiation. The two temporal regions described above are also present in the band integrals. Up to $\Delta t = 100$ ps, the band integrals show no changes, which proves that there is no reduction and recombination of the emitted ions with the main nanoparticle at least during this time.

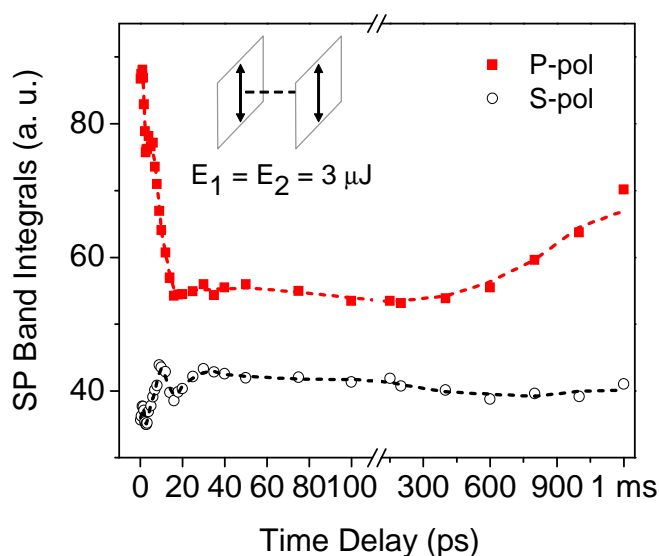


Fig. 5.18. Surface plasmon (SP) band integrals from irradiations with parallel-polarized pulse pairs of $3 \mu\text{J}$ of energy per pulse.

This is compatible with the remarks we have made above for the heating of the glass and the ionic mobility. After 100 ps, the P-polarized band integrals increase gradually while the S-polarized integrals remain constant. This indicates an overall increase of the band integrals of the nanoparticle system for the longer delay times. The details of these processes cover basically the reduction of the ions and their recombination with the main nanoparticle, which will be discussed soon.

In this context, one can ask the question: what happens to the emitted ions and the remaining nanoparticle, if the surrounding glass (not only the immediate vicinity of the nanoparticle rather the glass as a full system) is hot enough so that the ions can move far away from the nanoparticle. The test of this idea is a temperature-dependent experiment (see Ch. 4.5), where the laser irradiation is applied on a pre-heated or pre-cooled glass. The resulting spectral properties of the nanoparticles display distinct changes in the high temperature regime, which we will present in the following.

5.6.1. Effect of glass temperature on nanoparticle shape modifications

Figure 5.19 shows the temperature dependent evolution of surface plasmon bands and the corresponding integrals of the $\Delta t = 1$ ms irradiation of silver nanoparticles in heated/cooled glass at different temperatures in the range from -100 up to 170 °C. The top panel of the figure shows three temperature intervals with

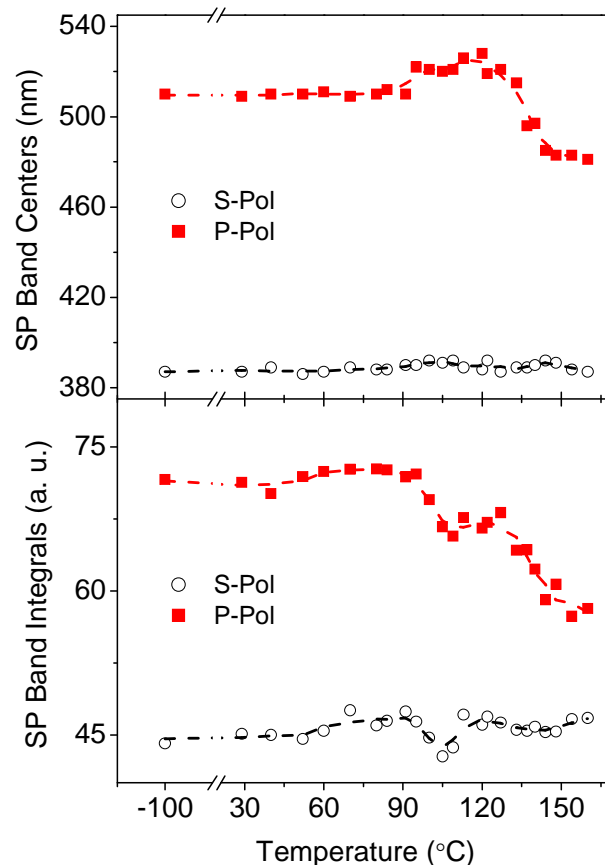


Fig. 5.19. Temperature dependences of surface plasmon (SP) band centers (top panel) and the corresponding band integrals (bottom panel) from irradiations with $\Delta t = 1$ ms pulses.

different behavior of the surface plasmon band centers. The first interval from -100 till 80 °C show that the positions of P- and S-polarized bands stay almost constant, and the spectra are almost identical. There is almost no difference in the results of the cold glass and the glass at room temperature. This may show that cooling the glass down to -100 °C is not enough to eliminate some mechanisms, because in any case the ion emissions are mainly electrical processes. Although the cold glass reduces the the mobility of the emitted ions, it is not observed from this experiment. For the higher temperatures, till 130 °C, P-polarized bands shift to the red, while the S-polarized bands are still constant. Further increase of the sample temperature leads to sharp shifts of the P-polarized band centers to shorter wavelengths [20].

The behavior of the band integrals in the range from -100 till 80 °C is similar to the band centers (bottom panel of Fig. 5.19); the band integrals stay nearly constant for both bands. However, the integrals of the P-polarized bands start to decrease very rapidly above 80 °C, while the S-polarized bands stay relatively constant. These results, comprising the sharp decreases of spectral gaps between P- and S-polarized bands and the decreases of integrals, suggest that the overall absorption of the nanoparticle system is reduced for higher glass temperatures. This indicates that the nanoparticle loses much of its volume due to ion emissions that can not recombine with the nanoparticle again. Most probably, the ions emitted into an already hot glass can move further away from the nanoparticle, and they can not come back again for the recombination. This case can be called as the dissolution (or destruction) of the nanoparticle.

5.6.2. Nanoparticle dissolution

As an illustration, Fig. 5.20 shows the spectra of two irradiation cases on a same sample containing silver nanoparticles. The top panel of the figure shows the spectra from the irradiation on the sample at room temperature, and the bottom panel shows the spectra from the irradiation on the sample, which was pre-heated to 154 °C. It is clearly seen that the irradiation of the nanoparticles in a hot glass matrix results in complete bleaching of the surface plasmon bands. At the same time, due to the huge broadening of the bands, the induced dichroism is disappearing [20].

As one can see, relatively low temperature variations (with respect to the glass transition temperature of 850 K) dramatically change the results of the laser-induced shape modification of nanoparticles. The observed bleaching of the bands and the disappearance of the spectral gap can be nicely associated with the discussion of the ionic mobility. As it was anticipated, the emitted Ag ions can move far away from the nanoparticle (causing the nanoparticle to dissolve) if the glass temperature is hot enough.

Having introduced the nanoparticle ionization, the Coulomb explosion, and the mobility of emitted ions; now we will develop the next events in time, namely the reduction of Ag ions by the trapped electrons, their precipitation and the following recombination with the main nanoparticle. Optical indications of these long-living mechanisms were observed within the temporal range of our experimental setup.

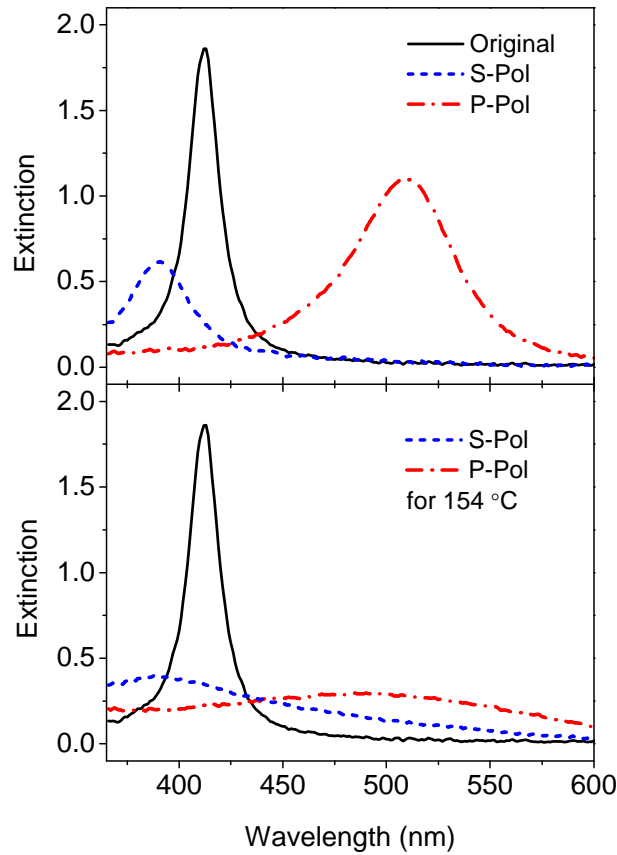


Fig. 5.20. Surface plasmon extinction bands of nanoparticles before laser irradiation (solid lines) and after laser irradiation with $\Delta t = 1$ ms pulses at room temperature (top panel) and at 154 °C (bottom panel).

5.7. Reduction of silver ions and recombination

Considering again the results of the pulse pair irradiation experiments for $\Delta t > 100$ ps (see Ch. 5.2), we can say that with the heating of the glass matrix, the potential barriers of the color centers that trap the emitted electrons are modified. The trapped electrons, therefore, can tunnel through the reduced potential barriers, becoming free. These free electrons can therefore reduce the Ag cations around the nanoparticle. Because most of the electrons in the parallel-polarized pulse pair irradiations are emitted along the poles of the nanoparticle, the reduction of the ions will also be mostly close to the poles of the nanoparticle in the direction of the laser polarization.

As long as the Ag ions are reduced, they form small silver clusters by aggregating and precipitating with the other reduced ions around. Depending on the thermal situation of the surrounding, the reduced Ag atoms may either diffuse back to and reaggregate with the original nanoparticle, or form small silver clusters in its surroundings. The recombination of these clusters with the main nanoparticle is observed as the increase in spectral gaps, which happens clearly after 100 ps [21]. This is a kind of Ostwald ripening process [22], where the big particles gain volume

at the expense of the volume of small ones. Gradually (with the additional cycle of effects from the coming pulses) an anisotropy is maintained along the pulse polarization direction, which is essentially the nanoparticle shape elongation. As it was stated in the description of the experimental results, the differences in the mechanisms and their time scales are indeed expected facts for different irradiation conditions. The results showed that although the recombination processes come to an end around 600 ps to 1 ns for the medium energy irradiations [21], they are observed to continue further for the high energy irradiations (see the increasing spectral gaps of Figs. 5.4 and 5.5). As the high energy pulses have two times the energy of the medium energy pulses, the induced non-equilibrium many-body interactions are surely much more drastic. Therefore, it takes longer time for the nanoparticle to relax after the irradiation with such high energy pulses. The results prove this in the sense that there are still some remaining processes, triggered by the first pulse that go on even after 1 ns.

This situation of increase in spectral gaps also urges an increase in the band integrals, because the nanoparticle system absorbs more and more as the total volume of the particle increases over time. The band integrals seen in Fig. 5.18 shows the overall increase of the the nanoparticle absorption with the increasing time delay ($\Delta t > 100$ ps), which proves the processes comprising the reduction of ions and their recombination with the main nanoparticle during this time interval.

In the case of low energy pulses, the glass in the vicinity of the nanoparticle can not be heated enough and therefore a hot nanoscopic surrounding of the nanoparticle is not achieved at all. This thermal situation is not enough to free the electrons trapped in the trapping centers of the glass [10]. Therefore, the low energy irradiation regime does not allow the formation of a considerable amount of neutralization to the emitted ions, and the subsequent clustering is prohibited. For this reason, the experimental results showing monotonous decreases in the spectral gaps (Fig. 5.3) suggest that a high amount of recombination of the emitted ions with the main nanoparticle does not take place for such low energy irradiations.

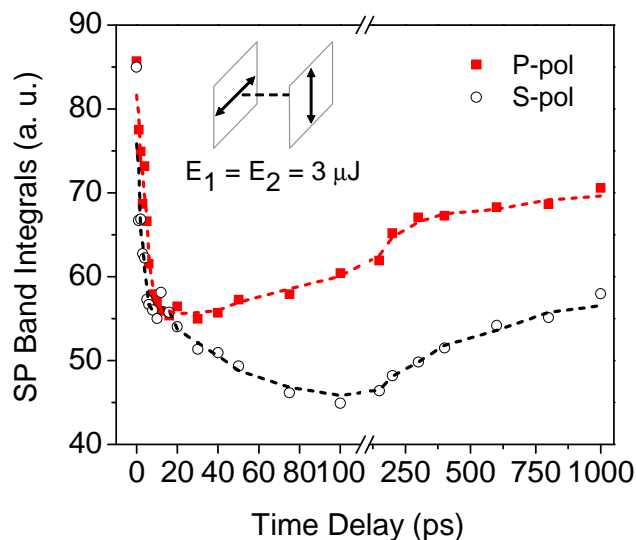


Fig. 5.21. Surface plasmon (SP) band integrals from irradiations with orthogonal-polarized pulse pairs of $3 \mu\text{J}$ of energy per pulse.

The time scales we have discussed above, regarding the reduction and clustering of the ions and the recombination of the small Ag clusters with the main nanoparticle are expected to hold for both parallel and orthogonal-polarized pulse pair irradiations. This statement is of course true only if the irradiation conditions (for example the applied pulse intensity) are the same for both cases. Therefore, now we want to compare our knowledge with the results of the orthogonal-polarized pulse pair irradiations. First of all we want to consider the band integrals (corresponding to the SP band centers given in Fig. 5.6) of the orthogonal-polarized irradiation to comment on the long-term absorption dynamics observed in the nanoparticle system for this irradiation mode. Figure 5.21 shows that the integrals of the P- and S-polarized bands move in opposite directions until 100 ps: the increases in P-polarized band integrals are accompanied by the decreases in S-polarized band integrals. The overall absorption of the nanoparticle system, therefore, stays more or less constant until 100 ps. This is well in agreement with the above arguments for the mobility time scale of silver ions. The increases in the spectral gaps during this time (Fig. 5.6) must be due to the reduction of the ions along the poles of the second-hitting pulse polarization direction. During the time when the isotropic ion emissions take place due to the first pulse, the second pulse can directly reduce those ions along its polarization direction with the pulse-enhanced electron emissions. With the increasing number of pulse pairs hitting the nanoparticle, a population of small silver clusters near to nanoparticle in the second-hitting pulse polarization direction is created. However, they can not add up (join) to the nanoparticle volume yet, therefore, the overall added behaviour of P- and S-polarized band integrals stay almost constant until 100 ps, indicating a nanoparticle with a smaller volume.

In the following times, the small clusters can join to the main nanoparticle through the mentioned Ostwald ripening processes [22]. This will add up to the size of the nanoparticle and therefore to its absorption (as indicated by Eq. 2.17). This is also well compatible with the associated increases of P- and S-polarized band integrals for the long time delays.

5.8. One pulse model

As a short summary to the results presented in this chapter, we would like to consider a simple schematical view (see Fig. 5.22) of a silver nanoparticle in glass that is irradiated by an intense femtosecond laser pulse. The laser pulse has a central wavelength of 400 nm, which is very close to the surface plasmon absorption of the nanoparticle. The peak pulse intensity on the nanoparticle is not less than 0.2 TW/cm^2 (i.e. $2 \mu\text{J}$ of energy pulse focussed on $100 \mu\text{m}$ of spot size), which corresponds to the threshold intensity for permanent nanoparticle shape modifications. Some of the basic mechanisms and the corresponding time scales are depicted on the schematic from left to right on the time axis.

As soon as the intense laser pulse interacts with the nanoparticle, the localized plasmon oscillations of the nanoparticle are enhanced due to the very high electric field of the applied laser pulse (see Ch. 3.2). Such high field strengths can drive the electrons away from the nanoparticle, which we called as pulse-enhanced (direct and pulse-enhanced thermal) electron emissions. This is the first of the two electron

emission processes that ionizes the nanoparticle. The long living but less efficient second process of electron emissions was called as the isotropic thermal electron emissions. Absorbing the strong energy input of the laser pulse, the electrons that are not emitted by the pulse field reach very high temperatures, which make the thermal emission of electrons possible. The electron emission processes can be regarded as a relaxation mechanism of the hot electronic system. Although the pulse-enhanced electron emissions are anisotropic, i.e. having the direction of the laser polarization, the thermal electron emissions are isotropic in nature. The number of electrons emitted during the pulse is much higher than the number of electrons emitted thermally as depicted in Fig. 5.22. The emitted electrons lose their energy rapidly and they are trapped in the potential minima of the glass matrix. In addition to the electron emission processes, the other relaxation channel for the hot electronic system is the coupling of electrons with nanoparticle phonons. The nanoparticle lattice is heated by the hot electrons concomitant to the cooling of the electronic system [11].

The instability of the positively-ionized, hot nanoparticle shows itself as repulsive electrical forces on silver cations. This results in the Coulomb explosion process, which reduces the volume of the nanoparticle via silver ion emissions to the glass matrix. The experimental results showed that this process starts within a few ps and it is completed within 20 ps [11]. Subsequently, the emitted ions are reduced by the trapped electrons as soon as the electrons survive from the traps. The experimental results showed that the silver ions are not reduced until 100 ps [21], most probably due to the time it takes for the glass to heat up and heal the electron trapping centers [20]. After 100 ps, the ions around the nanoparticle (Fig. 5.22) are reduced – mostly around the poles of the nanoparticle owing to the large number of electrons in these regions. As the ions become neutralized, they precipitate and form small silver clusters. These small clusters can join to the main nanoparticle through the mentioned ripening processes.

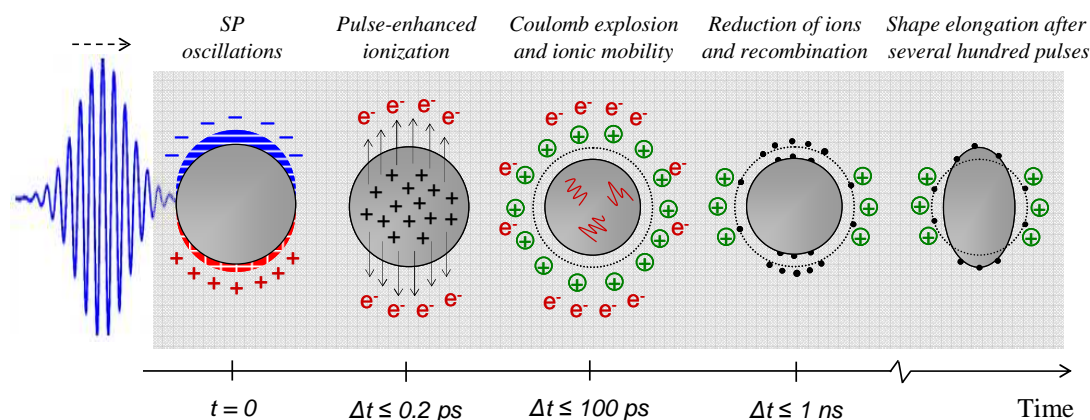


Fig. 5.22. A schematic view of the ultrafast dynamics on a silver nanoparticle in glass following the absorption of a femtosecond laser pulse. The emitted electrons are denoted by e^- , Ag cations are denoted by $+$ signs and small clusters of Ag atoms are denoted by black points.

The results indicated that the recombination of the small silver clusters with the main nanoparticle happens also within 1 ns for low and medium energy pulses [21]. As the strength of the laser irradiation increases (e.g. irradiation with high energy pulses), the non-equilibrium mechanisms will be more involved and the glass

temperature in the vicinity of the nanoparticle will be much higher, which can postpone the recombination processes. The forthcoming pulses will repeat the cycle of events summarized above on a 'step by step' slightly modified nanoparticle. As the period of the pulses is 1 ms, the events started by a pulse are finished before the second one hits the nanoparticle. This means that the material transport would accumulate with the increasing number of pulses. Therefore the increasing number of pulses will ripen the anisotropy of the nanoparticle [16, 20, 21], creating an elongation at the end as depicted by the schematic. One can identify a halo of small silver clusters on the equator sides of the nanoparticle at the end (see the TEM images in Ch. 4.2).

Chapter

6. Summary and conclusions

The research presented in this thesis is the result of a brand new experimental approach on laser-induced shape modification dynamics of silver nanoparticles embedded in glass. The approach is an easy-to-implement femtosecond laser irradiation technique that employs pairs of time-delayed laser pulses with equal energies for the modification of original, spherical silver nanoparticles (see Ch. 4.4). For each time delay between the pulse pairs, a separate part of the original sample (with spherical nanoparticles) was irradiated, thereby creating delay-dependent nanoparticle shape modifications. The corresponding persistent changes of the surface plasmon extinction bands were analyzed as a function of time delay and relative polarization of the pulse pairs. Comparing the resulting plasmon bands of the short time delays ($\Delta t \leq 1$ ns) with that of the $\Delta t = 1$ ms gave valuable information about the efficiency of nanoparticle shape modifications (see Ch. 5.1). It has been shown that the pulse pair irradiation with some time delays created higher nanoparticle shape elongations than the irradiation with pulses of $\Delta t = 1$ ms delay could do, and for some time delays the situation was reversed.

It was found that the strongest nanoparticle shape changes, i.e. the highest aspect ratios, were achieved when the time delay between pulse pairs is less than 3 ps (see Ch. 5.2 and 5.3). Using a two-temperature model, which have been extended to be valid for very high temperatures, the time dependence of directed and isotropic thermal electron emissions was estimated to decay also on a time scale of a few picoseconds (see Ch. 5.4). It was shown that directed, electric field-driven emission of hot electrons, which are then trapped in the glass matrix, is the key process initiating the transformation of Ag nanoparticles to non-spherical shapes. This directional memory, which is prepared only during the time of laser pulse interaction, defines the anisotropy of the whole, much longer-lasting process leading to ellipsoidal nanoparticles and persistent dichroism, respectively. The anisotropic, pulse-enhanced electron emission is counteracted by thermal, isotropic electron emission because of the very hot electronic system after the laser pulse has gone away (Ch. 5.4). As a result of the electron emissions, the nanoparticle gets highly ionized and dissolves partially by the Coulomb forces (see Ch. 5.5). The nanoparticle emits Ag ions into the glass matrix most probably on a timescale of a few picoseconds. This explains perfectly why the largest nanoparticle aspect ratios are being produced when the delay between pulse pairs is less than ≈ 3 ps.

After 10 ps the nanoparticle aspect ratios were strongly reduced in the case of pulse pairs having identical polarization and vanished using pulse pairs with orthogonal polarization. Therefore the results strongly suggested that the electron and following ion emissions from the nanoparticles are finished within less than 20 ps, and the directional memory is favorably defined by directed emission of hot electrons interacting with the laser field. In the case of orthogonal polarized pulse pairs, the preferential direction of the resulting nanoparticle aspect ratio (whenever there is any) is along the polarization direction of the second-hitting pulse.

Out of the above summarized results for the first 20 ps and thinking of the technological applications of laser-induced dichroism, it can be concluded that ultrashort laser pulses up to a duration of several picoseconds are well suited to prepare large spectral gaps between the polarized surface plasmon bands. However, the use of significantly longer pulses will favorably create the isotropic changes – up to complete particle destruction. This conclusion is in very good agreement with previous works, where considerable amount of nanoparticle aspect ratios were observed when nanoparticles were irradiated by pulses of 4 ps duration [1] while only isotropic changes and particle destruction were observed when nanoparticles were irradiated by ns pulses [2].

For the time delays after 20 ps, the heating of the glass matrix in the vicinity of the nanoparticle was taken into account (see Ch. 5.6). Considering only the classical heat diffusion from the nanoparticle, the glass was expected to get hot only within 200 ps. There are, however, other channels of heat transfer from the nanoparticle to the glass in addition to the classical heat diffusion: namely the electron and ion emissions. Owing to these very fast nanoparticle relaxation processes, the glass temperature was expected to reach as high as its melting temperatures in the immediate vicinity of the nanoparticle even at earlier times than 200 ps. The experimental observations suggested that the high temperature state of the glass lasts at least until 100 ps and the soft glass enables high mobility to the emitted Ag ions. The first evidence of the reduction and clustering of ions were observed after 100 ps. That is, until this time, the reduction of the ions was not observed in our results. During the high temperature state of the glass, the electron trapping sites of the glass are healed and the trapped electrons can become free in the glass conduction bands. These free electrons play very important roles in reducing the emitted, mobile Ag ions. Subsequently with the neutralization of the ions, silver atoms form small silver aggregates and clusters around the nanoparticle. Because the reduction of the ions takes place in the regions, where high number of electrons exists, bigger Ag clusters are formed in these regions. Generally speaking, these regions are along the direction of the second hitting pulse polarization. Finally the anisotropic recombination of these small Ag clusters with the main nanoparticle results in the gradual elongation of the nanoparticle.

The experimental results showed that the processes comprising the reduction of Ag ions, the clustering of the atoms and the recombination of these clusters with the main nanoparticle start after 100 ps. However, the laser irradiation parameters such as the energy of the pulses and their intensity decided on the end time of these processes. For the irradiation with pulse pairs having low and medium pulse energies these processes were observed to finish around 600 ps, while for high energy pulses there were some remaining processes even at 1 ns (see Ch. 5.7).

The results summarized above give insight into the nanoparticle shape modification dynamics in a pretty long time scale with very well experimental accuracy. In this sense, playing with the laser irradiation scenarios and nanoparticle properties can shift the time scales of the mentioned mechanisms. Finally, the introduced technique proves to be a valuable tool to investigate the nanoparticle shape modification dynamics or, more generally any ultrafast laser-induced processes, which lead to irreversible optical changes. In this sense, the time-delayed pulse pair irradiation is a reliable method and can provide additional information compared to usual pump-probe spectroscopy in these cases of permanent changes in metal nanoparticles.

References

Chapter 1.

- ¹ I. Freestone, N. Meeks, M. Sax, and C. Higgitt, *Gold Bulletin* **40**, 270 (2007).
- ² D. J. Barber and I. C. Freestone, *Archaeometry* **32**, 33 (1990).
- ³ C. Bohren and D. Huffmann, “*Absorption and Scattering of Light by Small Particles*” (Wiley, New York, 1983).
- ⁴ U. Kreibig and M. Vollmer, “*Optical Properties of Metal Clusters*” (Springer, Berlin, 1995).
- ⁵ S. Link and M. A. El-Sayed, *J. Phys. Chem. B* **103**, 8410 (1999).
- ⁶ E. Ozbay, *Science* **311**, 189 (2006).
- ⁷ S. A. Maier, “*Plasmonics*” (Springer, 2007).
- ⁸ R. W. Wood, *Phil. Mag.* **4**, 396 (1902).
- ⁹ J. C. Maxwell Garnett, *Philos. Trans. R. Soc. London* **203**, 385 (1904).
- ¹⁰ G. Mie, *Ann. Phys.* **330**, 377 (1908).
- ¹¹ K. L. Kelly, E. Coronado, L. L. Zhao, and G. C. Schatz, *J. Phys. Chem. B* **107**, 668 (2003);
E. Hao and G. C. Schatz, *J. Chem. Phys.* **120**, 357 (2004);
E. Hao, G. C. Schatz, and J. T. Hupp, *J. Fluoresc.* **14**, 331 (2004).
- ¹² K. Baba *et al.*, *Opt. Lett.* **16**, 964 (1991).
- ¹³ H. Ditlbacher, J. R. Krenn, B. Lamprecht, A. Leitner, and F. R. Aussenegg, *Opt. Lett.* **25**, 563 (2000).
- ¹⁴ V. M. Shalaev, “*Nonlinear Optics of Random Media: Fractal Composites and Metal-Dielectric Films*” (Springer, 2000).
- ¹⁵ A. Podlipensky, J. Lange, G. Seifert, H. Graener, and I. Cravetchi, *Opt. Lett.* **28**, 716 (2003).
- ¹⁶ M. Quinten, A. Leitner, J. R. Krenn, and F. R. Aussenegg, *Opt. Lett.* **23**, 1331 (1998).
- ¹⁷ S. A. Maier *et al.*, *Nat. Mater.* **2**, 229 (2003);
S. A. Maier *et al.*, *Adv. Mater.* **13**, 1501 (2001).
- ¹⁸ J. L. West and N. J. Halas, *Ann. Rev. Biomed. Eng.* **5**, 285 (2003).
- ¹⁹ J. R. Lakovicz *et al.*, *Anal. Biochem.* **301**, 261 (2002).
- ²⁰ M. L. Brongersma and P. G. Kik *eds.*, “*Surface Plasmon Nanophotonics*” (Springer, 2007).
- ²¹ J. Y. Bigot, V. Halte, J. C. Merle, and A. Daunois, *Chem. Phys.* **251**, 181 (2000);
N. Del Fatti, F. Vallee, C. Flytzanis, Y. Hamanaka, and A. Nakamura, *Chem. Phys.* **251**, 215 (2000);
S. Link, C. Burda, Z. L. Wang, and M. A. El-Sayed, *J. Chem. Phys.* **111**, 1255 (1999).
- ²² M. Kaempfe, T. Rainer, K. J. Berg, G. Seifert, and H. Graener, *Appl. Phys. Lett.* **74**, 1200 (1999); **77**, E459 (2000);
M. Kaempfe, H. Hofmeister, S. Hopfe, G. Seifert, and H. Graener, *J. Phys. Chem. B* **104**, 11847 (2000);
M. Kaempfe, H. Graener, A. Kiesow, and A. Heilmann, *Appl. Phys. Lett.* **79**, 1876 (2001).
- ²³ A. V. Podlipensky, “*Laser assisted modification of optical and structural properties of composite glass with silver nanoparticles*” Ph.D. Thesis, Martin-Luther-Universität Halle-Wittenberg (2005). <http://sundoc.bibliothek.uni-halle.de/diss-online/05/05H084/index.htm>

-
- ²⁴ A. Stalmashonak, G. Seifert, and H. Graener, *Opt. Lett.* **32**, 3215 (2007).
- ²⁵ see for example J. Y. Bigot, V. Halte, J. C. Merle, and A. Daunois, *Chem. Phys.* **251**, 181 (2000).
- ²⁶ C. Voisin, *et al.*, *Phys. Rev. B* **69**, 195416 (2004);
A. Arbouet, *et al.*, *Phys. Rev. Lett.* **90**, 177401 (2003).
- ²⁷ P. V. Kamat, M. Flumiani, and G. V. Hartland, *J. Phys. Chem. B* **102**, 3123 (1998).
- ²⁸ G. Seifert, M. Kaempfe, K. J. Berg, and H. Graener, *Appl. Phys. B* **71**, 795 (2000).
- ²⁹ T. Doppner, T. Fennel, T. Diederich, J. Tiggesbaumker, and K. H. Meiwes-Broer, *Phys. Rev. Lett.* **94**, 013401 (2005).
- ³⁰ A. V. Podlipensky, V. Grebenev, G. Seifert, and H. Graener, *J. Lumin.* **109**, 135 (2004).

Chapter 2.

- ¹ A. Sommerfeld, *Ann. Phys.* **28**, 665 (1909).
- ² R. W. Wood, *Phil. Mag.* **4**, 396 (1902).
- ³ J. C. Maxwell Garnett, *Philos. Trans. R. Soc. London* **203**, 385 (1904).
- ⁴ C. Kittel, *“Introduction to Solid State Physics”* 7th ed. (Wiley, 1996).
- ⁵ G. Mie, *Ann. Phys.* **330**, 377 (1908).
- ⁶ D. Pines, *Rev. Mod. Phys.* **28**, 184 (1956).
- ⁷ U. Fano, *Phys. Rev.* **103**, 1202 (1956).
- ⁸ E. Kretschmann, *Z. Physik* **241**, 313 (1971).
- ⁹ U. Kreibig and P. Zacharias, *Z. Physik* **231**, 128 (1970).
- ¹⁰ M. Fleischmann, P. J. Hendra, and A. J. McQuillan, *Chem. Phys. Lett.* **26**, 163 (1974).
- ¹¹ S. A. Maier, *“Plasmonics”* (Springer, 2007).
- ¹² E. Ozbay, *Science* **311**, 189 (2006).
- ¹³ N. W. Ashcroft and N. D. Mermin, *“Solid State Physics”* (Saunders College, 1976).
- ¹⁴ U. Kreibig and M. Vollmer, *“Optical Properties of Metal Clusters”* (Springer, Berlin, 1995).
- ¹⁵ P. B. Johnson and R. W. Christy, *Phys. Rev. B* **6**, 4370 (1972).
- ¹⁶ V. M. Shalaev and S. Kawata, *eds.*, *“Nanophotonics with Surface Plasmons”* (Elsevier, 2007).
- ¹⁷ P. N. Prasad, *“Nanophotonics”* John Wiley & Sons (2004).
- ¹⁸ C. Bohren and D. Huffmann, *“Absorption and Scattering of Light by Small Particles”* (Wiley, New York, 1983).
- ¹⁹ see for example L. Genzel, T. P. Martin, and U. Kreibig, *Z. Phys. B* **21**, 339 (1975).
- ²⁰ A. V. Podlipensky, *“Laser assisted modification of optical and structural properties of composite glass with silver nanoparticles”* Ph.D. Thesis, Martin-Luther-Universität Halle-Wittenberg (2005). <http://sundoc.bibliothek.uni-halle.de/diss-online/05/05H084/index.htm>
- ²¹ M. P. Seah and W. A. Dench, *Surface and Interface Analysis* **1**, 1 (1979).
- ²² S. Link and M. A. El-Sayed, *Ann. Rev. Phys. Chem.* **54**, 331 (2003).
- ²³ J. Porstendorfer, *“Numerische Berechnung von Extinktions- und Streuspektren sphäroidaler Metallpartikel beliebiger Größe in dielektrischer Matrix”* Ph.D. Thesis, Martin-Luther-Universität Halle-Wittenberg (1999).
- ²⁴ U. Kreibig and L. Genzel, *Surface Science* **156**, 678 (1985).
- ²⁵ K. L. Kelly, E. Coronado, L. L. Zhao, and G. C. Schatz, *J. of Phys. Chem. B* **107**, 668 (2003).

Chapter 3.

- ¹ J. Y. Bigot, V. Halte, J. C. Merle, and A. Daunois, *Chem. Phys.* **251**, 181 (2000).
- ² S. Link and M. A. El-Sayed, *Int. Rev. Phys. Chem.* **19**, 409 (2000).
- ³ see for example A. Arbouet, *et al.*, *Phys. Rev. Lett.* **90**, 177401 (2003).
- ⁴ C. Voisin, *et al.*, *Phys. Rev. B* **69**, 195416 (2004).
- ⁵ R. Loudon, “*The Quantum Theory of Light*” 3rd ed. (Oxford Science Publications, 2003).
- ⁶ H. A. H. Boot, and R. B. R. S. Harvie, *Nature* **180**, 1187 (1957).
- ⁷ L. V. Keldysh, *Sov. Phys. JETP* **20**, 1018 (1965).
- ⁸ Z. Lin, L. V. Zhigilei, and V. Celli, *Phys. Rev. B* **77**, 075133 (2008).
- ⁹ S. Link and M. A. El-Sayed, *J. Phys. Chem. B* **103**, 8410 (1999).
- ¹⁰ D. Pines and P. Nozieres, “*The Theory of Quantum Liquids*” (Benjamin, New York, 1966).
- ¹¹ C. Voisin *et al.*, *Phys. Rev. Lett.* **85**, 2200 (2000).
- ¹² C. Voisin, N. Del Fatti, D. Christofilos, and F. Vallee, *J. Phys. Chem. B* **105**, 2264 (2001).
- ¹³ M. Perner *et al.*, *Phys. Rev. Lett.* **78**, 2192 (1997).
- ¹⁴ R. H. M. Groeneveld, R. Sprik, and A. Lagendijk, *Phys. Rev. B* **51**, 11433 (1995);
C. K. Sun, F. Vallee, L. H. Acioli, E. P. Ippen, and J. G. Fujimoto, *Phys. Rev. B* **50**, 15337 (1994);
W. S. Fann, R. Storz, H. W. K. Tom, and J. Boker, *Phys. Rev. B* **46**, 13592 (1992).
- ¹⁵ see for example N. Del Fatti, C. Flyzanis, and F. Vallee, *Appl. Phys. B* **68**, 433 (1999).
- ¹⁶ N. Del Fatti, C. Voisin, M. Achermann, S. Tzortzakis, D. Christofilos, and F. Vallee, *Phys. Rev. B* **61**, 16956 (2000).
- ¹⁷ J. Y. Bigot, J. C. Merle, O. Cregut, and A. Daunois, *Phys. Rev. Lett.* **75**, 4702 (1995).
- ¹⁸ S. I. Anisimov, B. L. Kapeliovich, and T. L. Perelman, *Zh. Eksp. Teor. Fiz.* **66**, 776 (1974) [*Sov. Phys. JETP* **39**, 375 (1974)].
- ¹⁹ O. L. Muskens, N. Del Fatti, and F. Vallee, *Nano Lett.* **6**, 552 (2006).
- ²⁰ R. Hultgren, P. D. Desai, D. T. Hawkins, M. Gleiser, K. K. Kelley, and D. D. Wagman, “*Selected Values of the Thermodynamic Properties of the Elements*” (American Society for Metals, Ohio, 1973).
- ²¹ N. W. Ashcroft and N. D. Mermin, “*Solid State Physics*” (Saunders College, 1976).
- ²² *American Institute of Physics Handbook*, 3rd ed. (McGraw-Hill, New York, 1972).
- ²³ M. I. Kaganov, I. M. Lifshitz, and L. V. Tanatorov, *Zh. Eksp. Teor. Fiz.* **31**, 232 (1956) [*Sov. Phys. JETP* **4**, 173 (1957)].
- ²⁴ Y. Hamanaka, N. Hayashi, A. Nakamura, and S. Omi, *J. Lumin.* **76**, 221 (1998).
- ²⁵ S. Lysenko, J. Jimenez, G. Zhang, and H. Liu, *J. Elect. Mat.* **35**, 1715 (2006).
- ²⁶ T. S. Ahmadi, S. L. Logunov, and M. A. El-Sayed, *J. Phys. Chem.* **100**, 8053 (1996).
- ²⁷ J. K. Hodak, I. Martini, and G. V. Hartland, *J. Phys. Chem. B* **102**, 6958 (1998).
- ²⁸ T. Tokizaki, A. Nakamura, S. Kaneko, K. Uchida, S. Omi, H. Tanji, and Y. Asahara, *Appl. Phys. Lett.* **65**, 941 (1994).
- ²⁹ C. Kittel, “*Introduction to Solid State Physics*” 7th ed. (Wiley, 1996).
- ³⁰ A. Stalmashonak, A. Podlipensky, G. Seifert, and H. Graener, *Appl. Phys. B* **94**, 459 (2009).
- ³¹ A. Plech, V. Kotaidis, S. Gresillon, C. Dahmen, and G. von Plessen, *Phys. Rev. B* **70**, 195423 (2004).

-
- ³² A. Plech, V. Kotaidis, M. Lorenc, J. Boneberg, Nat. Phys. **2**, 44 (2006).
- ³³ H. Inouye, K. Tanaka, I. Tanahashi, and K. Hirao, Phys. Rev. B **57**, 11334 (1998).
- ³⁴ A. Plech *et. al.*, Europhys. Lett. **61** (6), 762 (2003).
- ³⁵ see for example M. Hu and G. V. Hartland, J. Phys. Chem. B **106**, 7029 (2002).
- ³⁶ K. L. Kelly, E. Coronado, L. L. Zhao, and G. C. Schatz, J. Phys. Chem. B **107**, 668 (2003);
E. Hao and G. C. Schatz, J. Chem. Phys. **120**, 357 (2004);
E. Hao, G. C. Schatz, and J. T. Hupp, J. Fluoresc. **14**, 331 (2004).
- ³⁷ F. Calvayrac, P. G. Reinhard, E. Suraud, and C. A. Ullrich, Phys. Rep. **337**, 493 (2000).
- ³⁸ U. Kreibig and M. Vollmer, “*Optical Properties of Metal Clusters*” (Springer, Berlin, 1995).
- ³⁹ G. Mie, Ann. Phys. **330**, 377 (1908).
- ⁴⁰ C. Bohren and D. Huffmann, “*Absorption and Scattering of Light by Small Particles*” (Wiley, New York, 1983).
- ⁴¹ A. V. Podlipensky, V. Grebenev, G. Seifert, and H. Graener, J. Lumin. **109**, 135 (2004).
- ⁴² M. Kaempfe, G. Seifert, K. J. Berg, H. Hofmeister, and H. Graener, Eur. Phys. J. D **16**, 237 (2001).
- ⁴³ A. Stalmashonak, G. Seifert, and H. Graener, Opt. Lett. **32**, 3215 (2007).
- ⁴⁴ T. Doppner, T. Fennel, T. Diederich, J. Tiggesbaumker, and K. H. Meiwes-Broer, Phys. Rev. Lett. **94**, 013401 (2005).
- ⁴⁵ P. V. Kamat, M. Flumiani, and G. V. Hartland, J. Phys. Chem. B **102**, 3123 (1998).

Chapter 4.

- ¹ Website of CODIXX AG: <http://www.codixx.de>
- ² K. J. Berg, A. Berger, and H. Hofmeister, Z. Phys. D **20**, 309 (1991).
- ³ A. V. Podlipensky, A. Abdolvand, G. Seifert, and H. Graener, Appl. Phys. A **80**, 1647 (2005).
- ⁴ A. Abdolvand, “*Modification of Optical and Structural Properties of Glass Containing Silver Nanoparticles via DC Electric Field and Moderately Elevated Temperatures*” Ph.D. Thesis, Martin-Luther-Universität Halle-Wittenberg (2006).
<http://sundoc.bibliothek.uni-halle.de/diss-online/06/06H011/index.htm>
- ⁵ M. Kaempfe, “*Laserinduzierte Deformation metallischer Nanopartikel in Gläsern*” Ph.D. Thesis, Martin-Luther-Universität Halle-Wittenberg (2000).
<http://sundoc.bibliothek.uni-halle.de/diss-online/00/00H165/index.htm>
- ⁶ M. Kaempfe, T. Rainer, K. J. Berg, G. Seifert, and H. Graener, Appl. Phys. Lett. **74**, 1200 (1999); **77**, E459 (2000);
M. Kaempfe, G. Seifert, K. J. Berg, H. Hofmeister, and H. Graener, Eur. Phys. J. D **16**, 237 (2001).
- ⁷ M. Kaempfe, H. Graener, A. Kiesow, and A. Heilmann, Appl. Phys. Lett. **79**, 1876 (2001);
M. Kaempfe, H. Hofmeister, S. Hopfe, G. Seifert, and H. Graener, J. Phys. Chem. B **104**, 11847 (2000).
- ⁸ A. Stalmashonak, G. Seifert, and H. Graener, Opt. Lett. **32**, 3215 (2007).
- ⁹ J. Porstendorfer, K. J. Berg, and G. Berg, J. Quant. Spectrosc. Radiat. Transf. **63**, 479 (1999).
- ¹⁰ K. L. Kelly, E. Coronado, L. L. Zhao, and G. C. Schatz, J. Phys. Chem. B **107**, 668 (2003).

-
- ¹¹ A. V. Podlipensky, “*Laser assisted modification of optical and structural properties of composite glass with silver nanoparticles*” Ph.D. Thesis, Martin-Luther-Universität Halle-Wittenberg (2005). <http://sundoc.bibliothek.uni-halle.de/diss-online/05/05H084/index.htm>
- ¹² A. Stalmashonak, A. Podlipensky, G. Seifert, and H. Graener, *Appl. Phys. B* **94**, 459 (2009).
- ¹³ P. F. Moulton, *J. Opt. Soc. Am. B* **3**, 125 (1986).
- ¹⁴ E. Hecht, “*Optics*” 4th ed. (Addison Wesley, 2002).
- ¹⁵ FROG tutorial of Rick Trebino's group at the Georgia Institute of Technology, <http://www.physics.gatech.edu/gcuo/Tutorial/tutorial.html>
- ¹⁶ J. A. Armstrong, *Appl. Phys. Lett.* **10** (1), 16 (1967).
- ¹⁷ D. J. Kane and R. Trebino, *IEEE J. Quantum Electron.* **29** (2), 571 (1993).
- ¹⁸ R. Trebino and D. J. Kane, *J. Opt. Soc. Am. A* **11**, 2429-2437 (1993);
K. W. DeLong et al., *Opt. Lett.* **19**, 2152-2154 (1994).
- ¹⁹ K. W. DeLong et al., *J. Opt. Soc. Am. B* **11** (11), 2206 (1994).
- ²⁰ R. Trebino, “*Frequency-Resolved Optical Gating: the Measurement of Ultrashort Laser Pulses*” (Kluwer, Boston, 2002).
- ²¹ J. R. Shulman and W.D. Compton, “*Color Centers in Solids*” (Pergamon, New York, 1962).
- ²² A. V. Podlipensky, V. Grebenev, G. Seifert, and H. Graener, *J. Lumin.* **109**, 135 (2004).
- ²³ G. G. Dyadyusha and A. A. Ishchenko, *Zh. Prikl. Spektrosk.* **30**, 1037 (1979) [*J. Appl. Spectrosc.* **30**, 746 (1979)].

Chapter 5.

- ¹ G. Seifert, M. Kaempfe, K. J. Berg, and H. Graener, *Appl. Phys. B* **73**, 355 (2001).
- ² F. Gonella, G. Mattei, P. Mazzoldi, E. Cattaruzza, G. W. Arnold, G. Battaglin, P. Calvelli, R. Polloni, R. Bertozello, R. F. Jr. Haglund, *Appl. Phys. Lett.* **69**, 3101 (1996).
- ³ M. Kaempfe, G. Seifert, K. J. Berg, H. Hofmeister, and H. Graener, *Eur. Phys. J. D* **16**, 237 (2001).
- ⁴ G. G. Dyadyusha and A. A. Ishchenko, *Zh. Prikl. Spektrosk.* **30**, 1037 (1979) [*J. Appl. Spectrosc.* **30**, 746 (1979)].
- ⁵ G. Mie, *Ann. Phys.* **330**, 377 (1908).
- ⁶ C. Bohren and D. Huffmann, “*Absorption and Scattering of Light by Small Particles*” (Wiley, New York, 1983).
- ⁷ U. Kreibig and M. Vollmer, “*Optical Properties of Metal Clusters*” (Springer, Berlin, 1995).
- ⁸ B. N. J. Persson, *Surf. Sci.* **281**, 153 (1993).
- ⁹ A. V. Podlipensky, V. Grebenev, G. Seifert, and H. Graener, *J. Lumin.* **109**, 135 (2004).
- ¹⁰ J. R. Shulman and W.D. Compton, “*Color Centers in Solids*” (Pergamon, New York, 1962).
- ¹¹ A. A. Unal, A. Stalmashonak, G. Seifert, and H. Graener, *Phys. Rev. B* **79**, 115411 (2009).
- ¹² T. Doppner, T. Fennel, T. Diederich, J. Tiggesbaumker, and K. H. Meiwes-Broer, *Phys. Rev. Lett.* **94**, 013401 (2005);
T. Doppner, T. Fennel, P. Radcliffe, J. Tiggesbaumker, and K. H. Meiwes-Broer, *Phys. Rev. A* **73**, 031202(R) (2006);

-
- T. Doppner, S. Teuber, M. Schumacher, J. Tiggesbaumker, and K. H. Meiwes-Broer, *Appl. Phys. B* **71**, 357 (2000).
- ¹³ P. V. Kamat, M. Flumiani, and G. V. Hartland, *J. Phys. Chem. B* **102**, 3123 (1998).
- ¹⁴ F. Calvayrac, P. G. Reinhard, E. Suraud, and C. A. Ullrich, *Phys. Rep.* **337**, 493 (2000).
- ¹⁵ A. V. Podlipensky, “*Laser assisted modification of optical and structural properties of composite glass with silver nanoparticles*” Ph.D. Thesis, Martin-Luther-Universität Halle-Wittenberg (2005). <http://sundoc.bibliothek.uni-halle.de/diss-online/05/05H084/index.htm>
- ¹⁶ A. Stalmashonak, A. Podlipensky, G. Seifert, and H. Graener, *Appl. Phys. B* **94**, 459 (2009).
- ¹⁷ A. A. Unal, A. Stalmashonak, G. Seifert, and H. Graener, *Proceedings of SPIE* **7032**, 703225 (2008).
- ¹⁸ A. Plech, V. Kotaidis, S. Gresillon, C. Dahmen, and G. von Plessen, *Phys. Rev. B* **70**, 195423 (2004).
- ¹⁹ A. Plech, V. Kotaidis, M. Lorenc, J. Boneberg, *Nat. Phys.* **2**, 44 (2006).
- ²⁰ A. Stalmashonak, A. A. Unal, H. Graener, and G. Seifert, *J. Phys. Chem. C* **113**, 12028 (2009).
- ²¹ A. A. Unal, A. Stalmashonak, G. Seifert, and H. Graener, *Phys. Rev. B*, submitted (2009).
- ²² L. Ratke and P. W. Voorhees, “*Growth and Coarsening: Ostwald Ripening in Material Processing*” (Springer, Berlin, 2002).

Chapter 6.

- ¹ G. Seifert, M. Kaempfe, K. J. Berg, and H. Graener, *Appl. Phys. B* **73**, 355 (2001).
- ² F. Gonella, G. Mattei, P. Mazzoldi, E. Cattaruzza, G. W. Arnold, G. Battaglin, P. Calvelli, R. Polloni, R. Bertinello, R. F. Jr. Haglund, *Appl. Phys. Lett.* **69**, 3101 (1996).

Acknowledgments

First of all, I would like to express my gratitude to my supervisor Professor Dr. Heinrich Graener, for giving me the opportunity to do this work and for his continuous guidance throughout my studies. It was a great pleasure for me to conduct my Ph.D. under his supervision.

I am also very grateful to Priv.-Doz. Dr. Gerhard Seifert for his generous supports and for fruitful discussions.

I would like to thank all the coworkers and staff of the Optics Group for providing me with a nice and friendly working environment. Especially I want to thank my colleague Andrei Stalmashonak for his friendship and continuous enthusiasm in discussing the results. I must also thank Dr. Jens Lange for his technical assistance in the lab.

Additionally, I want to acknowledge the former coordinator of the International Max Planck Research School for Science and Technology of Nanostructures, Dr. Monika Kaempfe, for her kind supports from my first days in Halle until now.

Finally, I am grateful to my wife and my parents for their endless encouragements during my studies.

Publications

- 1. Ultrafast dynamics of silver nanoparticle shape transformation studied by femtosecond pulse-pair irradiation**
A. A. Unal, A. Stalmashonak, G. Seifert, and H. Graener
Phys. Rev. B **79**, 115411 (2009).
- 2. Time-resolved investigation of laser-induced shape transformation of silver nanoparticles**
A. A. Unal, A. Stalmashonak, H. Graener, and G. Seifert
Phys. Rev. B, submitted (2009).
- 3. Effects of temperature on laser-induced shape modification of silver nanoparticles embedded in glass**
A. Stalmashonak, A. A. Unal, G. Seifert, and H. Graener
J. Phys. Chem. C **113**, 12028 (2009).
- 4. Towards the production of micro-polarizers by irradiation of composite glasses with silver nanoparticles**
A. Stalmashonak, G. Seifert, A. A. Unal, U. Skrzypczak, A. Podlipensky, A. Abdolvand, and H. Graener
Appl. Opt. **48**, F38 (2009).
- 5. Effects of electron emission strengths on the formation of prolate and oblate spheroids from Ag nanospheres**
A. A. Unal, A. Stalmashonak, H. Graener, and G. Seifert
In preparation (2009).
- 6. Femtosecond shape transformation dynamics of silver nanoparticles in glass**
A. A. Unal, A. Stalmashonak, G. Seifert, and H. Graener
Plasmonics: Metallic Nanostructures and Their Optical Properties VI, Proceedings of SPIE Vol. **7032**, 703225 (2008).
- 7. Optimization of dichroism in laser-induced transformation of silver nanoparticles in glass**
A. Stalmashonak, A. A. Unal, G. Seifert, and H. Graener
Plasmonics: Nanoimaging, Nanofabrication, and Their Applications IV, Proceedings of SPIE Vol. **7033**, 70331Z (2008).



Curriculum Vitae

Personal Details

Name: Ahmet Akın Ünal
Date of Birth: 7. October 1979
Place of Birth: Çorum, Turkey
Current Address: Lessing Straße 11, 06114 Halle

Education

1998-2003 B.Sc. in Physics
Koç University, Istanbul, Turkey.
B.Sc. Independent study: “Optical properties of porous silicon”
Supervisor: Prof. Dr. Ali Serpengüzel

2003-2005 M.Sc. in Electronics Engineering and Computer Science
Sabanci University, Istanbul, Turkey.
M.Sc. Thesis: “Inhibited spontaneous emission of perylene dye molecules embedded in nano-cavities” Supervisor: Prof. Dr. Naci Inci

Since WS 2005/06 Ph.D. in Physics
Martin-Luther-Universität Halle-Wittenberg.
Ph.D. Thesis: “Time-resolved investigations on ultrafast shape modification dynamics of silver nanoparticles embedded in glass” Supervisor: Prof. Dr. Heinrich Graener

Work Experience

2003-2005 Teaching (Optoelectronics / Semiconductor Physics and Devices / Calculus / Nature of Science) and research assistant at Sabanci University, Istanbul, Turkey.

Since WS 2005/06 Scientific coworker in Optics Group, Physics Department at Martin-Luther-Universität Halle-Wittenberg.

SS 2008, 2009 Teaching assistant in “Physikalisches Grundpraktikum” at Martin-Luther-Universität Halle-Wittenberg.



Erklärung

Hiermit erkläre ich, daß ich diese Arbeit selbständig und ohne fremde Hilfe verfaßt, andere als die von mir angegebenen Quellen und Hilfsmittel nicht benutzt und die den benutzten Werken wörtlich oder inhaltlich entnommenen Stellen als solche kenntlich gemacht habe.

Eine Anmeldung der Promotionsabsicht habe ich an keiner anderen Fakultät einer Universität oder Hochschule beantragt.

Ahmet Akın Ünal